SAPIENZA
UNIVERSITÀ DI ROMA

Adaptive Control of Launch Vehicles in Atmospheric Flight

Department of Mechanical and Aerospace Engineering

Ph.D. in Aeronautics and Space Engineering - XXXIII Ph.D. program

Candidate

Domenico Trotta

ID number 1254945

Thesis Advisor   Co-Advisor

Prof. Guido De Matteis   Prof. Alessandro Zavoli

2021

Thesis defended on 26 May 2021
in front of a Board of Examiners composed by:

Prof. Roberto Camussi (chairman)
Prof. Fabrizio Giulietti
Prof. Pierangelo Masarati

Adaptive Control of Launch Vehicles in Atmospheric Flight

Ph.D. thesis. Sapienza – University of Rome

This thesis has been typeset by LATEX and the Sapthesis class.

Author's email: domenico.trotta@uniroma1.it

Abstract

The research focuses on the development of innovative control techniques for attitude control of a launch vehicle (LV) during the atmospheric flight, and to investigate their possible benefits in terms - for instance - of improved disturbance rejection capability, as well as, a means for reducing the burden of recurrent activities of mission integration and flight program software finalization.

In this respect, a complete nonlinear mathematical model of the launch vehicle dynamics, comprehensive of all relevant aspects for the attitude control problem is first developed. Next, linearized equations of motion are derived under the assumption of small deviations of the vehicle motion from a reference trajectory. The time-invariant linear model is used to synthesize a baseline controller (BC) that features two proportional-derivative (PD) components for attitude and translational motion control, plus filters to phase-stabilize and notch the bending modes by using classical, frequency-based, analysis, and control design techniques.

Among several advanced algorithms referenced in the literature, the Adaptive Augmenting Control (AAC) has been selected and implemented in the LV flight control system in order to retain the functionality and proven record of success of classically designed linear control systems, while consistently and predictably improving their performance and robustness in expanded flight and/or uncertainty parameter envelopes. AAC adjusts the action of a baseline PID-type controller by means of a forward loop gain multiplicative adaptive law that, basically, on-line modulates BC output either to minimize the error with respect to a reference model or to limit undesirable high-frequency response in the control path.

In order to fully exploit the AAC potentiality, an effective and reliable tuning procedure for AAC gains is developed, where a robust design optimization (RDO) problem is formulated, and the goal is to maximize a statistical metric that describes FCS performance measured over a set of LV simulations. Finally, an analysis of the effects of uncertainties on bending mode characteristics is carried out. Variations of bending mode parameters have a significant and negative impact on AAC performance and, consequently, on LV stability. In this respect, the use of adaptive filters is investigated in order to further improve flight control system robustness. An adaptive notch filter is designed, the parameters of which are updated continuously by an adaptation algorithm that uses the pitch rate sensor output so as to estimate the unknown parameters of the filter and precisely match the actual bending mode frequency.

Contents

List of Figures

List of Tables

Chapter 1

Introduction

1.1 Thesis objectives

This study is focused on the development of innovative control techniques for the attitude control of a launch vehicle (LV) during the atmospheric phase of flight.

Industries are still very reliant on classical control theories for high-risk aerospace applications, even though a detailed review of the available historical LV data from 1990 to 2002 reveales that 41% of failures might have been mitigated by advanced GN&C technologies [1]. This lack of attitude towards innovation is mainly due to the fact that proven experience on classic methods allows to manage well known controller limitations, such as time-consuming synthesis process and lack of robustness with respect to uncertainties, and thus to adopt reliable procedures for control system design, analysis, and verification.

Classical control systems, such as PID controllers with gain scheduling, are typically able to meet requirements for flight and meet stability and performance criteria, as required among other specifications for flight certification. However, the demand for increased FCS robustness and, in general, more effective technologies for risk reduction with respect to possible loss of performance due to model uncertainties, off-nominal flight conditions and unexpected environmental disturbances, and reduced time needed to design FCS for a specific mission, calls for the investigation of the impact of modern design methodologies on the FCSs developed using classical techniques.

Therefore, the objectives of this research work is to investigate the opportunity to improve the performance of currently used attitude control systems by an adaptive control architecture. In particular, the major goals of the study are as follows

- To investigate the possible benefits of modern control methodologies in terms

– for instance – of improved performance, increased robustness, scalability and expendability, as well as higher capability of accommodating flight anomalies and/or some class of failures

- To analyze limitations of the classical approach, with particular attentions to the aspects related to recurrent activities of mission integration and flight program software finalization, including gain tuning with the related extensive validation and verification, as payload mass, target injection orbit, or launch conditions are varied for each flight

- To assess whether (or not) the aforementioned issues could be limited by the adoption of a novel approach to LV FCS design.

1.2   Research topics

FCS design for LVs in atmospheric flight is a challenging task from a control point of view, where the fundamental aim is to ensure stability and adequate response to guidance commands while satisfying very demanding and conflicting requirements in the presence of external disturbances, such as wind gusts.

LVs are complex systems, the dynamics of which must be appropriately modeled when the design, stability, and performance analyses of FCS are dealt with. In particular, the present study is focused on the attitude control of LVs in the atmospheric flight phase, which begins at lift-off, lasts up to first stage separation and takes approximately 100-140 s of flight time. During the ascent trajectory the vehicle experiences rapid variations of mass and inertia properties, and aero-propulsive characteristics. The high value of dynamic pressure that LV encounters during the aforementioned phase generates aerodynamic loads that could damage the structural integrity of LV. Moreover, stability problems need to be addressed because the LV is inherent unstable, due to the forward position of the aerodynamic center with respect to the center of gravity, and highly flexible due to the slender shape. In particular, since the first bending mode frequency is usually close to the crossover frequency of the rigid body dynamics, the control system has the potential to excite the bending mode and destabilize the vehicle dynamics. Also, translation and rotational dynamics are controlled through thrust vectoring, realizing the thrust vector control (TVC) and, in this respect, control authority is limited to the nozzle rotation of non-throttleable engines, whose angular range is constrained to a few degrees.

In this framework, an accurate nonlinear simulation model and an associated linear model are mandatory, and represent powerful tools for performance and

stability analysis. The most remarkable LV simulation model in literature is the Stability Aerospace Vehicle ANalysis Tool (SAVANT) presented in [2]. SAVANT uses fully coupled nonlinear equations of motion, including both six-degrees-of-freedom (6-DoF) rigid body and flexible body effects, to run time-domain simulations throughout the entire launch profile. This model features a realistic description of aerodynamics, propulsive and inertial forces and moments. Engine inertia ("tail-wags-dog") effects, liquid-propellant slosh, and TVC actuator models are also included. The set of equations developed for the SAVANT model is recalled in [3], where inertial, aerodynamic, propulsive, and bending modes dynamic data for ARES-I relative to the ascent trajectory are also provided.

In the framework of VEGA program, a high-fidelity, nonlinear 6-DoF simulator for V&V (verify and validate) purposes, called Vegacontrol [4], was developed by European Launch Vehicle (ELV). It is implemented in Matlab/Simulink and it is tailored to simulate the VEGA launcher during the atmospheric phase. Vegacontrol is representative of the real launch system, accounting for rotational and translational dynamics of the vehicle, elastic and sloshing modes, tail-wags-dog (TWD) effect, and nonlinear aerodynamics, including aero-elastic effects. Moreover, Vegacontrol presents a detailed model of INS (Inertial Navigation system) measurements, a nonlinear TVC actuator model, and also the Roll and Attitude Control System (RACS) for roll axis control. Finally, Vegacontrol allows to perform simulations where a number of parameters are scattered, and different wind profiles are specified.

Several linearized models have been proposed in the open literature, even though the underlying assumptions for the derivation of the governing equation lack clarity to some extent, and/or are excessively restrictive [5, 6]. A model of LV pitch motion, incorporating flexible and sloshing dynamics, and TVC inertial effects, is presented in [7], with particular focus on analyzing aeroelastic effects on a slender-body conventional LV. Although presented without derivation, the linearized planar model of a large, flexible boost rocket and a comprehensive presentation of the relevant dynamics, that is, rigid and flexible body dynamics, propellant slosh and nozzle inertial effect, are reported in [8] together with a straightforward mechanization of the equations of motion in state-space form.

Moreover, an exhaustive and comprehensive derivation of the 6-DoF linear equations of motion for a LV in the body reference frame is presented in [9], including the effects of elasticity, fuel sloshing and engine inertia. Finally, in [10] a linear model of both LV rigid and flexible dynamics is derived in a trajectory reference frame that translates axially with the vehicle but remains tangent to the ascent trajectory.

During the atmospheric flight, attitude control is required to stabilize the system, reject wind disturbances, and limit the aerodynamic loads while minimizing the offset from reference trajectory. The robustness of the control system to uncertainty on vehicle aero-mechanical parameters, such as bending modes characteristics (that is, natural frequencies and modal participation factors), aerodynamic coefficients, engine exhaust velocity, and TVC dynamics, is also mandatory.

Traditional approaches for LV attitude control are based on gain-scheduled proportional-integral-derivative (PID) controllers to stabilize the rigid body dynamics. This kind of controller typically features different feedbacks on available sensor measurements (i.e. drift, drift-rate, acceleration, angle-of-attack) to minimize the structural loads suffered by LV and error with respect to the reference trajectory. Moreover, the FCS incorporates appropriate structural bending filters for gain- or phase-stabilization of the elastic modes sensed by rate gyros [11].

This control architecture was widely used proving its effectiveness in satisfying performance and stability requirements for a number of vehicles, such as Saturn V [12, 13] and Space Shuttle [14], where control laws based on attitude and attitude-rate plus acceleration signals for load alleviation and bending filters were implemented. A similar controller architecture is used for the Japanese H-IIA LV [15] which employs a PD on attitude angle, bending mode filters, and a load relief control that uses a lateral accelerometer to detect the effects of wind and reduce the aerodynamic load. Other examples are the FCS of the ARES-I [16, 17] LV that adopts an attitude PID controller with an anti-drift/load-relief algorithm plus a set of attitude and rate bending filters, and the Brazilian VLS [18] and Korea Space Launch Vehicle-I [19] that feature a PID attitude controllers plus notch filters for the stabilization of the bending modes. Proportional-derivative (PD) controllers for attitude and lateral drift, combined with bending filters, are also used in the FCS of the European VEGA launcher [20]. The classical FCS's of LVs recalled so far allow for performance evaluation using classical frequency-domain criteria based on stability margins and time-domain simulations that represent well-proven practices for flight certification.

In order to deal with rapidly changing dynamics, a gain-scheduling approach is commonly adopted, that is obtained by interpolating between a set of linear controllers designed for a different set of LV linear model associated to several operating points along the ascent trajectory. The resulting controller is a linear system whose parameters are scheduled as a function of time or other useful variables (such as the so called non-gravitational velocity) [20]. In spite of the simplicity of implementation, the design of gain-scheduling controllers presents two main drawbacks: it is time-consuming since the parameters are determined for many

operating conditions, and, the stability of the system is not guaranteed even if the system is stable at each operating point [21, 22].

Classical control techniques are designed for nominal conditions and do not implicitly consider uncertainties during the design process. The robustness characteristics are enforced through stability margin requirements, i.e. 6 dB gain margin and 30 deg phase margin, that is a standard practice in industry to accommodate the stability degradation due to uncertain parameters. Finally, stability, performance and robustness of the controller are verified and validated through extensive campaigns of Monte Carlo (MC) and worst-case simulations [23, 24], where model parameters are suitably scattered.

In the above framework, it appears that effective design methodologies are demanded to increase FCS robustness to model uncertainties, off-nominal flight conditions, and unexpected wind disturbances. Moreover, FCS robustness could be further exploited as a means for reducing the burden of recurrent activities of mission integration and flight program software finalization, including gain tuning with the related extensive validation and verification, as payload mass, target injection orbit or launch conditions are varied for each launch.

These aspects led to research efforts dedicated to the development and application of design methodologies based on optimal control theory; examples are the Brazilian VLS LV, where the Linear Quadratic Regulator (LQR) method is used for the tuning of the controller [25] in atmospheric flight, and the FCS of the Ariane 5 LV that was initially designed using the Linear Quadratic Gaussian (LQG) approach [26].

These two optimal methods represent automated ways to devise multivariable controllers, that allow to reduce the complexity of gain tuning and improve design performance [27]. Nevertheless, the LQR and LQG approaches do not provide any guaranteed stability robustness against parametric uncertainties and unmodelled dynamics [28].

The limitations of LQR and LQG encouraged the investigation of robust control methodologies for LV attitude control that address the robustness issue in the design, such as $\mathcal{H}_\infty$ control [29], Linear-Parameter-Varying (LPV) [30] and μ-synthesis [31].

$\mathcal{H}_\infty$ control design aims at finding a controller that minimizes the $\mathcal{H}_\infty$ norm of the transfer function from the external inputs and the outputs signals to be minimized/penalized, that includes both performance and robustness measures. The $\mathcal{H}_\infty$ -norm corresponds to the maximum gain between input and output signals over all frequencies. A crucial step in $\mathcal{H}_\infty$ control robust design is to find appropriate weighting functions for the optimization process. It usually involves trial and error procedure relying on design experience and knowledge of the plants [32].

LPV techniques have been proposed in order to overcome the issues related to gain scheduling for the synthesis of a multivariable controller for a flexible LV [33], where the design is optimized taking into account a linear time-varying LV model. The main principle of μ control is to find a controller K that reduces the maximum singular value by solving a sequence of scaled $\mathcal{H}_\infty$ problems, which defines an iterative design procedure, called D-K iteration involving dynamic frequency-dependent scaling called D scaling. This technique has been presented in a limited number of studies on launcher control design [34, 31], as, for istance, one major issue is that there are no guarantees that the D-K iteration will converge.

It is also worth to remark that $\mathcal{H}_\infty$, LPV and μ-synthesis techniques have some limitations because the designed controller is usually of high order and without a defined structure, that makes it difficult to analyze and adjust its parameters. Moreover, the $\mathcal{H}_\infty$ requirements are expressed in terms of weighting functions in the frequency domain, and this requires a significant effort to define a relation between performance requirements and $\mathcal{H}_\infty$ constraints.

In the last decade, significant contributions to the implementation of $\mathcal{H}_\infty$ controllers for LVs has come from the structured $\mathcal{H}_\infty$ synthesis [35], which allows to perform a robust control tuning (i.e. $\mathcal{H}_\infty$) for a controller with specified order and structure. With respect to classical techniques, structured $\mathcal{H}_\infty$ is promising in order to achieve a direct trade-off between robustness and performance, to reduce tuning effort and cost prior to each mission flight, and has the capability to directly include system uncertainties in the design [36]. The feasibility of structured $\mathcal{H}_\infty$ synthesis technique for the control of a flexible LV during non-stationary ascent phase has been investigated in recent papers [37, 38]. Nevertheless, in practical scenarios, (structured) $\mathcal{H}_\infty$ control still requires a significant effort as well as a thoughtful iterative design process, that heavily relies on the designer experience, to properly shape the weighting functions so that stability, robustness, and performance requirements are satisfied

Another class of control methods that manages systems with uncertain parameters and unmodelled dynamics is in the framework of adaptive control. This methodology provides controllers able to adapt their parameters to accommodate unpredictable changes in the system response. Among the best know adaptive control architectures, we recall the Model Reference Adaptive Control (MRAC) [39, 40, 41], where the adaptation of the control law is realized by minimizing the difference between the output of the controlled system and the response of a reference model.

In recent years, the interest in using adaptive control techniques for attitude control of LVs in atmospheric flight has increased.

In Ref. [42] the main focus is to develop a Lyapunov based adaptive PD and PID controller based on the MRAC technique for a highly unstable rigid LV model. In [43], an adaptive control system based on MRAC is proposed, that uses several basis functions to approximate the uncertainties in the system dynamics, and a reference model is developed using feedback linearization. Since vehicle dynamics and baseline controller are time varying, several linearization points and reference models are required. Moreover, in [44], a control allocation algorithm is combined with MRAC to guarantee the stability and tracking performance of a LV in the presence of actuator failure. An improved weighting algorithm and an anti-saturation controller are developed in the same study to compensate for saturation errors.

Besides MRAC, other innovative adaptive control techniques have been developed. In Ref. [45] a methodology based on a direct adaptive fuzzy controller is presented to control the pitch attitude dynamics of LVs, incorporating Lyapunov principle in the adaptation in order to guarantee that the system is asymptotically stable. Reference [46] uses an output feedback neural network adaptive element, that augments a baseline gain scheduled controller for attitude control and vibration suppression of a crewed LV.

Finally, a number of papers are focused on the application of adaptive control techniques to the design of notch filters [47, 48, 49] used to limit the effects of vibrations due to LV flexibility. In this respect, $\mathcal{L}_1$ adaptive output feedback architecture for a flexible crew LV is proposed in [50] to control the flexible DoFs, the frequencies of which are close to those of the rigid body dynamics.

The adaptive control laws are inherently nonlinear, their behavior is not always predictable and, although many researches have been carried out on this topic, the certification for safety-critical applications for this class of controllers remains a serious concern from an industrial point of view.

The Adaptive Augmenting Control (AAC) has been proposed [51, 52] in the framework of the Space Launch System (SLS) program [53], the upcoming LV under development by NASA. AAC is intended to retain the functionality and proven record of success of classically designed linear control systems while consistently and predictably improving their performance and robustness in expanded flight and/or uncertainty parameter envelopes. AAC adjusts the action of a baseline PID-type controller (BC) by means of a forward loop gain multiplicative adaptive law which, basically, on-line modulates BC output either to minimize the error with respect to a reference model or to limit undesirable high frequency response in the control path. Specific adaption limits are enforced to preserve BC stability margins.

A number of papers report on the advantages of the AAC architecture in the

FCS of SLS with respect to the three design objectives of (i) minimal adaptation, (ii) improved performance, and (iii) loss of vehicle (LoV) prevention [51, 52, 54]. AAC stability has been extensively and exhaustively investigated by a number of techniques [51, 55, 56]. In particular, a time-varying model of a typical first stage pitch axis dynamics has been considered in [51] showing that the augmenting controller is shown to retain stability and prevent the LoV experienced by the system without adaptation, when significant corner cases are dealt with, such as the situations of large aerodynamic instability in presence of strong wind disturbances, or a significant reduction of the first bending mode frequency paired with an increment of modal gain at the attitude angle sensor.

Performance of AAC architecture in a realistic model of SLS featuring a digital three-axis autopilot with bending filters, a pseudo-optimal control allocation scheme, and nonlinear observers for active in-flight disturbance compensation (DAC) has been investigated in [52]. Results of frequency domain stability analyzes and dispersed simulations of vehicle ascent flight show the advantages of gain modulation provided by AAC in terms of envelope expansion and robustness enhancement. A number of Monte Carlo analyses have been conducted in [54] using a rigorous and extensive sampling process where dispersions are applied on mass properties, aerodynamic and structural parameters, actuator dynamics, thrust misalignment, winds, and sensor errors to demonstrate that the AAC algorithm meets the aforementioned design goals. Also, AAC integration in the full SLS digital 3-axis autopilot, including integration with the production flight software prototype, discussed in the same paper, appears fully satisfying.

Stability assessment for this (adaptive) nonlinear control system has been addressed by using a combination of frequency-domain methods and high-fidelity Monte Carlo simulations. Stability margins of SLS have been analyzed in the time domain in [55] to verify the fidelity of the classical approach. An extensive and more exhaustive analysis has been reported in [56]. There, the stability of AAC implemented in the SLS control architecture featuring BC and DCA is investigated by several techniques, including Lyapunov-based stability analysis, classical stability analysis with gain modulation, generalized gain margins analysis, and time-domain stability margin assessment and Monte Carlo simulations with expanded dispersion. Even in this broader assessment perspective, which also led to some recommendations on AAC parameter tuning, is it apparent that AAC performance objectives are met for operations in off-nominal conditions. It is worth to mention that AAC algorithm capability, robustness, and reproducibility, have been successfully demonstrated by an in-flight test campaign on a piloted F/A-18 [57].

In recent times, the application of the AAC architecture to the European VEGA LV in the atmospheric flight phase has been investigated, with the main purpose of improving FCS stability and performance robustness characteristics as well as reducing the effort dedicated to the processes of pre-flight (re)tuning and validation. In [38] the adaptive augmentation has been applied to a BC for pitch and yaw axes, designed using the structured $\mathcal{H}_\infty$ control technique. Again the AAC prevents LoVs and improves BC performance, but the complexity of adaptive law tuning process in the absence of a specific design methodology and analysis tools is remarked as a drawback of the approach.

One may conclude that, although extended capabilities of AAC architecture over flight-certified LV BCs have been demonstrated, a sound method for quantifying the benefits of the nonlinear adaptive augmentation is still to be devised. It is also apparent that selection of appropriate values of AAC parameters, where different elements act concurrently and independently to modulate the multiplicative forward gain [54], is far from trivial. In this respect, suitability of heuristic, trial-and-error tuning procedures is debatable, as an assessment of expected improvement of baseline FCS calls for extensive and time-consuming V&V activities, where stability and performance targets and criteria are not clearly established.

As mentioned above, in addition to stability and performance, FCS must also ensure that the bending modes related to the flexible structure of the LV are not excited. The conventional approach for compensating bending mode instability consists of placing notch filters in the feedback control loop so as to suppress sensor signals in a selected range bending mode frequencies. This is a difficult task because the characteristics of the bending modes, i.e. natural frequency and modal participation terms, vary during the flight and their value is uncertain to some extent. Moreover, the introduction of the bending filters generally results in degradation of the rigid-body stability margins and performance.

Different synthesis approaches have been investigated in the last decade to address the aforementioned notch filter implementation difficulties. The bending filters of the NASA's Ares-I launch vehicle are designed using a constrained numerical optimization [58] providing minimal degradation to the rigid-body stability margins. An integrated design optimization framework for gain scheduling and bending filters is applied to the design of FCS of Korea Sounding Rocket III (KSR-III) [59]. The objective of the optimization is to minimize the worst case peak of the open-loop transfer function at the first bending mode frequency with constraints on the stability margins during the ascent flight.

LV sensors contain signals at the bending mode frequencies in addition to those

due to rigid body motion. In this respect, many studies deal with the use of adaptive control to stabilize LV flexible dynamics, where different techniques are used to identify the frequency of the bending modes from sensor output, and using this information to set the notch filter center frequency. An in-depth analysis on the tracking notch filter concept and its application to LV FCS is conducted in [60]. Gain and phase stabilization by means of an adaptive filter in order to stabilize the first and second bending modes of a SI-B launch vehicle [61] are investigated, where the frequency tracking system is based on the relative phase between the input and the reference output of a tunable second order filter. This technique is also discussed in [62], where different types of demodulators are applied to detect the phase shift.

Moreover, a practical adaptive notch filter using an $\mathcal{H}_\infty$ bending frequency estimator is proposed in [63] to remove the signal component due to the time-varying structural mode of a missile from the rate sensor measurements. A model reference adaptive method is proposed in [64], that relies on MIT rule, an adaptive law developed in 1960 by the researchers of Massachusetts Institute of Technology (MIT) [65, 66], to adjust on-line the center frequency of a discrete notch filter in order to meet the actual frequency of the bending mode. Moreover, the study in [67] presents an adaptive notch filter the design parameters of which are updated continuously by an adaptation algorithm that uses the pitch rate sensor output to estimate the unknown parameters of the filter, and precisely match the actual bending mode frequency. To this end, the recursive least-squares (RLS) method [68] is adopted as adaptation algorithm, which minimizes the weighted root-mean-square of the notch filter output. The feasibility of the controller for the stabilization of a flexible LV is demonstrated in [48] using a ground-based testbed, developed to model the varying frequency of a flexible LV.

1.3   Research outline

The rationale for the present work stems from recognizing that adding an adaptive controller on top of a BC can provide additional robustness to FCS of LVs in the presence of significant parameter uncertainty, and a recovery capability from unanticipated, severe off-nominal conditions.

Therefore, the main aim is to study adaptive control laws that can extend FCS capabilities in order to: 1) improve performance and safety in terms of reference trajectory error and aerodynamic load minimization despite wind disturbances; 2) improve stability robustness against parameter uncertainties; 3) reduce the workload in the activities of controller tuning and V&V before each flight.

The specific research activities are listed as follows:

To study Adaptive Augmenting Control (AAC) in order to enhance the system performance while keeping the classical LV control architecture. The aim is to provide a critical and detailed assessment of the potential of the AAC techniques for the implementation in the FCS of a LV of the same class of the European VEGA launcher. Effectiveness of the AAC in increasing performance and robustness of FCS in off-nominal conditions, that involve variations of rigid-body parameters and bending-mode frequencies, is then investigated by means of numerical simulations and using tools from linear system analysis.

To develop an optimal AAC parameter tuning methodology to fully exploit the AAC potentiality. The objective is to reduce the issues and burden of manual, trial-and-error procedures currently adopted for the design of AAC adaption law. To this end, two methodologies for AAC parameter tuning are presented where a robust design optimization (RDO) problem [69] is formulated, and the goal is to maximize a statistical metric that describes FCS performance measured over a set of representative simulations of LV flight. In more detail, the tuning procedures rely on a genetic algorithm (GA) [70] and the Nelder-Mead simplex method [71] in order to find the optimal adaptive law parameters that minimize attitude error and traversal aerodynamic loads. In so doing, the occurrence of LoV events may be reduced [51].

To investigate Adaptive Notch Filter (ANF) techniques to improve the FCS robustness to uncertainties on the flexible dynamics characteristics of LV. In this respect, the use of adaptive bending mode filters to provide also phase-margin adaptation appears promising in order to further improve FCS robustness. In more detail, a pitch rate driven adaptive algorithm is used to adjust on-line the design parametrs of an adaptive notch filter [67, 48] so that the centering frequency of notch filter precisely matches the actual bending mode frequency. To this end, the recursive least-squares (RLS) method [68] is adopted that minimizes the weighted root mean square of the notch filter output in order to estimate the bending mode frequency.

To develop an Extended AAC (EAAC) capable to exploiting the gain-adaptation capabilities of the AAC combined with the phase-margin adaptation provided by ANF so as to further improve FCS robustness. In particular, EAAC is devised adding the AAC on the top of the typical PD controller featuring adaptive bending mode filters.

A combination of classical analyses in the frequency domain, simulations of selected stressing cases, and Monte Carlo simulations for scenarios with scattering of several model parameters are carried out for a detailed investigation of EAAC performance.

1.4   Thesis summary

This section briefly describes the organization of this thesis.

Chapter 2 presents a mathematical model of the LV. First, a 6-DoF nonlinear model is developed taking into account all physical aspects relevant for the attitude control of LV during the atmospheric phase of flight (from lift-off to first stage separation), such as the rigid-body dynamics, aerodynamic and propulsion forces, the effects of elasticity, and the inertial coupling terms due to the nozzle rotation in the TVC. Next, the linearized equations of motion are derived under the assumptions of small-disturbances with respect to a trajectory reference frame. Moreover, the TVC actuator dynamics and wind models are discussed.

In Chapter 3, the main elements of a classical BC featuring two proportional-derivative (PD) components for attitude and translational motion control, plus notch and low-pass filters to gain and phase stabilize the bending mode, are recalled. The FCS robustness to the uncertainty on LV parameters is also investigated.

In Chapter 4, the main features of the AAC architecture are critically reviewed, and a detailed investigation of opportunities and limitations when an AAC system is adopted for LV attitude control in atmospheric flight is carried out. Moreover, two effective tuning procedures, that involve the solution of the RDO problem, are devised for the AAC parameters, while appropriate guidelines are provided for the setup of spectral damper filters. Performances of FCS tuned according to the optimal approaches are assessed.

Chapter 5 recalls the main features of the adaptive notch filter design and RLS adaptive algorithm. The main difficulties related to this adaptive control problem are investigated by applying them to simple problems. Development of the EAAC is presented, that features the AAC and an RLS algorithm to adapt the notch filter of BC to variations of the first bending mode frequency.

In Chapter 6, the results of the performance analysis of the BC augmented by AAC and EAAC are presented and discussed with the objective of investigating and comparing the effectiveness of the different control architectures. The performance and robustness assessment is carried out using time-domain simulations of selected stressing cases and Monte Carlo simulations for scenarios with scattering of several

model parameters and/or wind disturbances.

Finally, the conclusions and major contributions of this study are presented in Chapter 7.

Chapter 2

Launch vehicle model

The launch vehicle model for the design of attitude controller must be comprehensive of all relevant features that are necessary to describe the LV behavior during the atmospheric phase of flight, that goes from lift-off to first stage separation. The main features of the model are

- Rigid-body translation and rotation

- Structural elastic dynamics modelled using rocket bending modes

- Inertial coupling effects due to nozzle rotation

- Aerodynamic and thrust force and moments

- TVC actuators dynamics

In what follows a complete derivation of the equations of motion is proposed, based on the formulations presented in Greensite [9] and Garner [10]. First, the 6-DoF EOMs for rigid-body LV nonlinear model are presented and then, a linear model with respect to the trajectory reference frame is derived to be used for FCS development.

Usually, for the purpose of attitude control system design, the coupling between pitch and yaw dynamics may be ignored because LV roll rate is typically small and, moreover, the LV considered in this thesis is a rocket symmetric about the roll axis. Therefore, single-axis, 3-degree of freedom (3-DoF) linear model can be used to describe the motion of the LV. Consequently, the attitude control systems for the yaw and pitch dynamics are frequently based on the same architecture. The derived linear model allows using of traditional stability criteria borrowed from classical control theory, such as phase-margin and gain-margin. Since the system is inherently time-varying, the transfer functions are computed at successive time-points along the

trajectory, and an assumption is made that stability can be assessed by considering points on the trajectory where the parameters are varying "slowly enough" that they may be assumed constant.

2.1 Reference frames

The different reference frames necessary for describing the mathematical model of the LV, are recalled in this section.
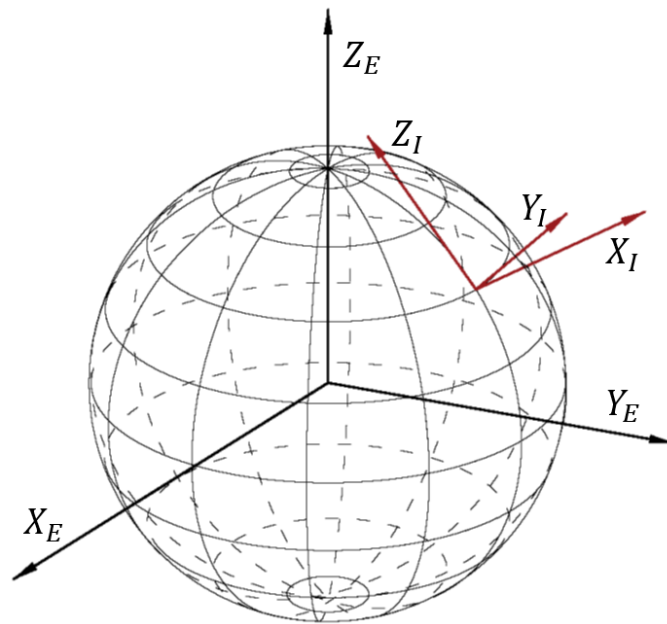
Figure 2.1. Representation of earth-centered inertial reference frame (X_E, Y_E, Z_E), and Launch base reference frame (X_I, Y_I, Z_I).

Earth-centered inertial reference frame

The not-rotating Earth-centered inertial frame S_E with set of basis vectors X_E, Y_E, Z_E has its origin at the Earth center as illustrated in Fig. 2.1. The z-axis is normal to the equatorial plane, coincides with the Earth rotation axis and points to the North Pole. The x-axis lies in the equatorial plane pointing towards the vernal equinox. The remaining axis y is in the equatorial plane and completes the right-handed Cartesian system. Because the Earth's orbital motion around the Sun is negligible in the trajectory analysis of the LV, this frame is often considered as an inertial reference frame.

Launch base reference frame

The launch base reference frame S_I, with coordinates X_I, Y_I, Z_I shown in Fig. 2.1, is taken with origin at the launch site, and with X_I-axis directed along the local vertical directed upward, Z_I-axis pointed to north, and Y_I-axis pointed to east. In this study, because of the Earth is regarded as flat and stationary in inertial space, and any coordinate reference frame attached to the Earth is therefore an inertial system, the launch base reference frame is considered as inertial frame. This assumption is sufficiently accurate because the duration of the atmospheric phase of rocket ascent trajectory is of the order of a few minutes, so that the effects of the Earth rotation are negligible [9, 72]. In particular, it is remarkable to evaluate the contribution of the Coriolis acceleration $2\omega^E V$ that is at most $5\%g$ at first stage separation, considering that the Earth rate of rotation is $\omega^E = 7.27 \times 10^{-5}$ and that the typical maximum speed reached by a LV of the same size class as VEGA at the end of the first stage is $V = 2000 - 3000\,\text{m/s}$. This term must therefore be negligible.

Body-fixed reference frame

The body-fixed frame S_B with basis vectors $\hat{\mathbf{i}}$, $\hat{\mathbf{j}}$, $\hat{\mathbf{k}}$ is a right-hand coordinate system, X_B, Y_B, Z_B fixed to the vehicle's body as illustrated in Fig.2.2. Its origin is the center of gravity, the $\hat{\mathbf{i}}$-axis is along the vehicle's longitudinal axis, the $\hat{\mathbf{j}}$-axis, perpendicular to the $\hat{\mathbf{k}}$-axis points downward and the $\hat{\mathbf{j}}$-axis points rightward.
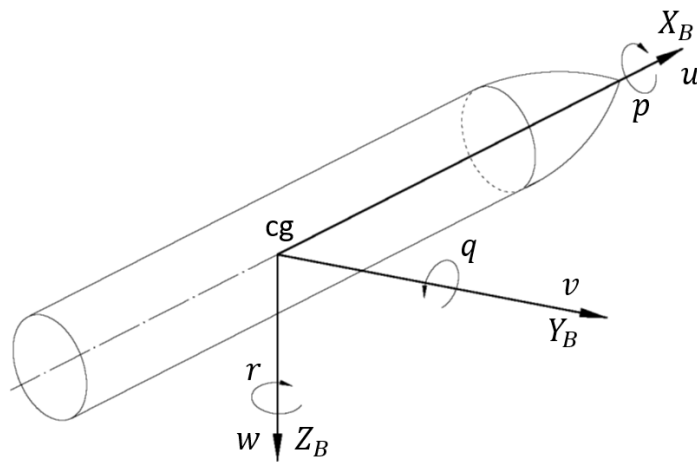
Figure 2.2. Illustration of body-fixed reference frame (X_B, Y_B, Z_B).

Trajectory reference frame

The trajectory reference frame S_t with basis vectors $\hat{\mathbf{i_t}}$, $\hat{\mathbf{j_t}}$, $\hat{\mathbf{k_t}}$, X_t, Y_t, Z_t is a right hand non-stationary frame that translates axially with the vehicle but remains tangent to the ascent trajectory. The $\hat{\mathbf{i_t}}$ and the $\hat{\mathbf{j_t}}$ axes are, respectively, tangent and normal to the nominal trajectory. $\hat{\mathbf{k_t}}$ completes the right-hand frame.

2.2 Nonlinear rigid-body model

The equations of motion (EOMs) are derived by applying the Newton's laws to the rigid body and the motion will be described with reference to an inertial coordinate system S_I, that is taken equal to the launch base reference frame, whereas, the inertial coupling terms due to the engine nozzle motion are introduced in the model according to the Euler-Lagrange equation [73]. Considering a mass element of the launch vehicle, its velocity may be expressed in S_I by

$$\boldsymbol{\mu} + \frac{d\boldsymbol{\rho}}{dt} = \boldsymbol{\mu} + \boldsymbol{\omega} \times \boldsymbol{\rho} \tag{2.1}$$

where $\boldsymbol{\mu}$ is the velocity of the origin of S_B expressed as

$$\boldsymbol{\mu} = u\hat{\mathbf{i}} + v\hat{\mathbf{j}} + w\hat{\mathbf{k}} \tag{2.2}$$

The position vector $\boldsymbol{\rho}$ of the element of mass respect to the origin of S_B is

$$\boldsymbol{\rho} = x\hat{\mathbf{i}} + y\hat{\mathbf{j}} + z\hat{\mathbf{k}} \tag{2.3}$$

The angular velocity $\boldsymbol{\omega}$ of S_B is also expressed as

$$\boldsymbol{\omega} = p\hat{\mathbf{i}} + q\hat{\mathbf{j}} + r\hat{\mathbf{k}} \tag{2.4}$$

According to Ref. [9], the equations of motion are given in S_B as

$$m\left[\frac{\delta\boldsymbol{\mu}}{\delta t} + \boldsymbol{\omega} \times \boldsymbol{\mu}\right] = \mathbf{F}_{g_b} + \mathbf{F}_{T_b} + \mathbf{F}_{A_b} + \mathbf{F}_{N_b} \tag{2.5}$$

$$\mathbf{I}\dot{\boldsymbol{\omega}} + \boldsymbol{\omega} \times \mathbf{I}\boldsymbol{\omega} = \mathbf{M}_{T_b} + \mathbf{M}_{A_b} + \mathbf{M}_{N_b} \tag{2.6}$$

where $\frac{\delta}{\delta t}()$ denotes time derivative with respect to the body frame S_B, the subscripts in the right-hand side terms stay for gravity (g), thrust (T), aerodynamics (A), and nozzle inertial coupling effects (N), and m and $\mathbf{I}$ are mass and inertia tensor of the LV, respectively. Moreover, the subscript (b) indicates that the force and moment

components are in S_B frame

Writing the EOMs in scalar form for the LV 6-DoF dynamics gives

$$m\left(\dot{u} + qw - rv\right) = F_{x_b} \tag{2.7}$$

$$m\left(\dot{v} + ru - pw\right) = F_{y_b} \tag{2.8}$$

$$m\left(\dot{w} + pv - qu\right) = F_{z_b} \tag{2.9}$$

where

$$F_{x_b} = F_{g_{x_b}} + F_{T_{x_b}} + F_{A_{x_b}} + F_{N_{x_b}} \tag{2.10}$$

$$F_{y_b} = F_{g_{y_b}} + F_{T_{y_b}} + F_{A_{y_b}} + F_{N_{y_b}} \tag{2.11}$$

$$F_{z_b} = F_{g_{z_b}} + F_{T_{z_b}} + F_{A_{z_b}} + F_{N_{z_b}} \tag{2.12}$$

and

$$I_{xx}\dot{p} - I_{xy}(\dot{q} - pr) - I_{xz}(\dot{r} + pq) + I_{yz}(r^2 - q^2) + (I_{zz} - I_{yy})qr = M_{x_b} \tag{2.13}$$

$$I_{yy}\dot{q} - I_{xy}(\dot{p} + qr) - I_{yz}(\dot{r} + pq) + I_{xz}(p^2 - r^2) + (I_{xx} - I_{zz})pr = M_{y_b} \tag{2.14}$$

$$I_{zz}\dot{r} - I_{xz}(\dot{p} - qr) - I_{yz}(\dot{q} + pr) + I_{xz}(q^2 - p^2) + (I_{yy} - I_{xx})pq = M_{z_b} \tag{2.15}$$

where

$$M_{x_b} = M_{g_{x_b}} + M_{T_{x_b}} + M_{A_{x_b}} + M_{N_{x_b}} \tag{2.16}$$

$$M_{y_b} = M_{g_{y_b}} + M_{T_{y_b}} + M_{A_{y_b}} + M_{N_{y_b}} \tag{2.17}$$

$$M_{z_b} = M_{g_{z_b}} + M_{T_{z_b}} + M_{A_{z_b}} + M_{N_{z_b}} \tag{2.18}$$

2.2.1 Euler angles

The orientation of the LV is given relative to the launch base reference frame S_I by three Euler angles ψ, θ and ϕ. In this manner the yaw, pitch and roll angles describes LV attitude with respect to the initial position at the launch pad, because LV is first taken to be oriented so that the body frame axis are parallel to those of S_I frame (see Fig. 2.3). Therefore, the Euler angles are defined as follow

- rotate S_B about the Z_I axis by angle ψ (yaw angle) in the positive direction[1]

- then rotate about the new direction of Y' axis by an angle θ (pitch angle) in the positive direction

- finally, rotate about the X'' (i.e. X_B) axis by an angle ϕ (roll angle) in the positive direction.

---

[1]Positive direction is determined by the right-hand rule.
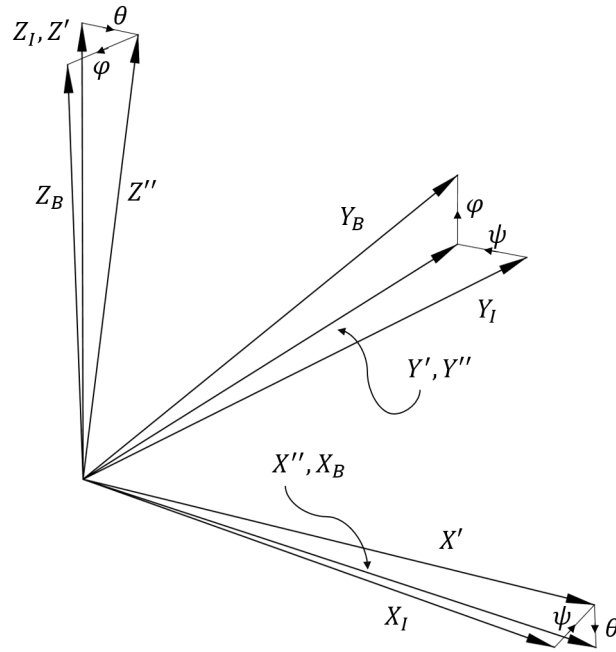
Figure 2.3. LV orientation respect to the S_I frame.

According to Ref. [74], the Euler angles are determined using the following set of differential equations

$$
\begin{bmatrix} \dot{\phi} \\ \dot{\theta} \\ \dot{\psi} \end{bmatrix} = \mathbf{R}^{-1} \begin{bmatrix} p \\ q \\ r \end{bmatrix} \tag{2.19}
$$

where

$$
\mathbf{R} = \begin{bmatrix} 1 & 0 & -\sin\theta \\ 0 & \cos\phi & \sin\phi\cos\theta \\ 0 & -\sin\phi & \cos\phi\cos\theta \end{bmatrix} \tag{2.20}
$$

2.2.2 Force and moments

(a) Pitch plane
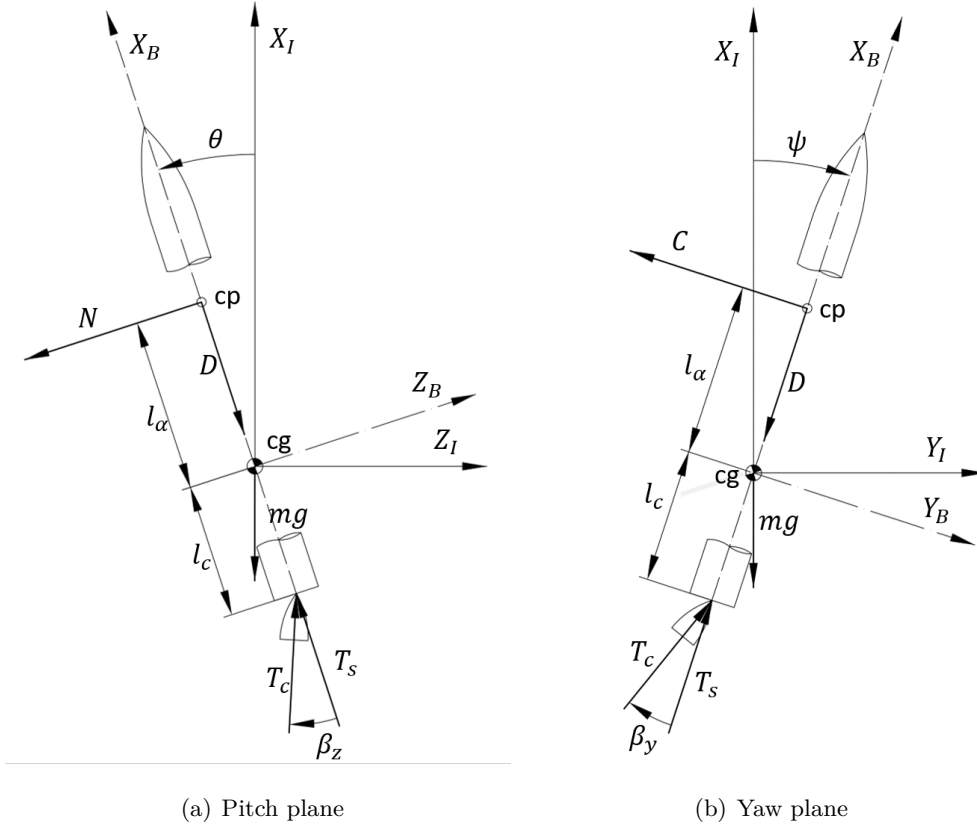
(b) Yaw plane

Figure 2.4. Sketch of forces acting on LV: (a) pitch plane, (b) yaw plane.

In this section we derive the force and moment terms in equations (2.7) - (2.15). The forces acting on the launch vehicle are shown in Fig. 2.4 for, pitch (Fig. 2.4(a)) and yaw (Fig. 2.4(b)) planes.

Weight

The weight force is applied in the center of gravity (c.g.) with components in S_B

$$F_{g_{x_b}} = -mg(\cos\theta\cos\psi) \tag{2.21}$$

$$F_{g_{y_b}} = -mg(\sin\phi\sin\theta\cos\psi - \cos\psi\sin\psi) \tag{2.22}$$

$$F_{g_{z_b}} = -mg(\cos\phi\sin\theta\cos\psi + \sin\phi\sin\psi) \tag{2.23}$$

Thrust

The thrust due to the rocket engines is one of the major forces acting on the LV during the flight, and it can be considered applied to the nozzle hinge, as shown in Fig. 2.4. Thrust is composed of the sustained thrust T_s, directed along the vehicle longitudinal axis, and the control (swivelled) thrust T_c, that realizes the thrust vector control (TVC) by means of which the LV is controlled. In particular, a reference frame S_N (with basis vectors X_N, Y_N, Z_N) can be defined rigidly attached to nozzle, with origin in the nozzle hinge and X_N directed along the nozzle symmetry axis. Y_N and Z_N are chosen to be parallel with Y_B and Z_B, respectively, when the control angles β_y and β_z are zero. Being T_c aligned with X_N, the thrust control force in the body frame S_B is

$$\boldsymbol{F}_{T_B} = \boldsymbol{L}_{BN}\boldsymbol{F}_{T_N} = \boldsymbol{L}_{BN}\begin{bmatrix} T_c \\ 0 \\ 0 \end{bmatrix} \tag{2.24}$$

where $\boldsymbol{L}_{BN}$ is the transformation matrix from S_N to S_B, that is

$$\boldsymbol{L}_{BN} = \begin{bmatrix} \cos\left(\beta_y\right)\cos\left(\beta_z\right) & -\sin\left(\beta_y\right) & -\sin\left(\beta_z\right)\cos\left(\beta_y\right) \\ \sin\left(\beta_y\right)\cos\left(\beta_z\right) & \cos\left(\beta_y\right) & -\sin\left(\beta_y\right)\sin\left(\beta_z\right) \\ \sin\left(\beta_z\right) & 0 & \cos\left(\beta_z\right) \end{bmatrix} \tag{2.25}$$

Thus, the force components of thrust force in S_B are

$$F_{T_{x_b}} = T_s + T_c\cos\beta_y\cos\beta_z \tag{2.26}$$

$$F_{T_{y_b}} = T_c\cos\beta_z\sin\beta_y \tag{2.27}$$

$$F_{T_{z_b}} = T_c\sin\beta_z \tag{2.28}$$

Moreover, the moments due to the thrust are

$$\boldsymbol{M}_{T_B} = \boldsymbol{r}_C \times \boldsymbol{F}_{T_B} \tag{2.29}$$

where $\boldsymbol{r}_C = \begin{bmatrix} -l_c & 0 & 0 \end{bmatrix}$ is the control arm, that is, the distance between the nozzle hinge and c.g. and depends on time. The moment components are

$$M_{T_{x_b}} = 0 \tag{2.30}$$

$$M_{T_{y_b}} = l_c\,T_c\sin\beta_z \tag{2.31}$$

$$M_{T_{z_b}} = -l_c\,T_c\cos\beta_z\sin\beta_y \tag{2.32}$$

For a LV in the boost phase of flight, T_s and T_c are function of time.

Aerodynamics

The aerodynamic force and moment components for missiles and space launch vehicles are obtained both experimentally and analytically via body axes [9] and, using quasi-steady-state aerodynamic theory, they are expressed in usual manner as follows

$$F_{A_{x_b}} = -D = -\frac{1}{2}\rho V^2 S C_D \tag{2.33}$$

$$F_{A_{y_b}} = -C = -\frac{1}{2}\rho V^2 S C_C \tag{2.34}$$

$$F_{A_{z_b}} = -N = -\frac{1}{2}\rho V^2 S C_N \tag{2.35}$$

$$M_{A_{x_b}} = 0 \tag{2.36}$$

$$M_{A_{y_b}} = -\frac{1}{2}\rho V^2 S l_\alpha C_N \tag{2.37}$$

$$M_{A_{z_b}} = -\frac{1}{2}\rho V^2 S l_\beta C_C \tag{2.38}$$

where S is the reference area, l_α and l_β are the aerodynamic moment arms that is, the distance between c.g. and center of pressure (c.p.) and V is the flight speed expressed as

$$V = [u^2 + v^2 + w^2]^{1/2} \tag{2.39}$$

It is further assumed that, due to the symmetry of the LV, no aerodynamic roll moment is presents and pitch M_{A_y} and yaw M_{A_z} moments are expressed in terms of normal C_N and side C_C coefficients.

The C coefficients in Eqs. (2.33) through (2.38) are, generally, function of variables α, β, $\dot{\alpha}$, $\dot{\beta}$, p, q, r. Furthermore, for LV having little or no lifting surfaces, the damping effects of the velocity variable are negligible, and only the dependence from α and β is taken into account. Therefore, it is assumed that the C function are expanded in a Taylor series about some steady-state condition, the C coefficients are

$$C_D = C_{D_0} + C_{D_\alpha}\alpha + C_{D_\beta}\beta \tag{2.40}$$

$$C_C = C_{C_0} + C_{C_\beta}\beta \tag{2.41}$$

$$C_N = C_{N_0} + C_{N_\alpha}\alpha \tag{2.42}$$

$$\tag{2.43}$$

where the subscript (0) represents the value in the steady state while C_{C_β} and C_{N_α}

correspond to the usual stability derivatives. According to Ref. [9], because of a symmetric LV is considered, C_{C_0} and C_{N_0} are zero, and, moreover, the aerodynamic drag C_D it is not dependent of α and β. However, C_{D_0}, C_{C_β} and C_{N_α} are function of the Mach number.

Fanally, the aerodynamic forces and moments are

$$F_{A_{x_b}} = -D = -\frac{1}{2}\rho V^2 S C_{D_0} \tag{2.44}$$

$$F_{A_{y_b}} = -C = -C_\beta \beta = -\frac{1}{2}\rho V^2 S C_{C_\beta}\beta \tag{2.45}$$

$$F_{A_{z_b}} = -N = -N_\alpha \alpha = -\frac{1}{2}\rho V^2 S C_{N_\alpha}\alpha \tag{2.46}$$

$$M_{A_{x_b}} = 0 \tag{2.47}$$

$$M_{A_{y_b}} = -Nl_\alpha = -N_\alpha l_\alpha \alpha = -\frac{1}{2}\rho V^2 S l_\alpha C_{N_\alpha}\alpha \tag{2.48}$$

$$M_{A_{z_b}} = -Cl_\beta = -C_\beta l_\beta \beta = -\frac{1}{2}\rho V^2 S l_\beta C_{C_\beta}\beta \tag{2.49}$$

Moreover, the aerodynamic angles are defined as α and β, that are, respectively, the angle of attack and sideslip angle expressed as

$$\alpha = \tan^{-1}\frac{w}{u} \tag{2.50}$$

$$\beta = \sin^{-1}\frac{v}{V} \tag{2.51}$$

Nozzle inertia

The effect of the nozzle mass rotation on LV dynamics is developed from first principles by using the derivation presented in [73]. Figure 2.5 shows the relevant elements of the LV configuration, where the total LV, rotating and translating with respect to S_I, is modeled as two interacting subsystems, that is, the base body B, to which S_B frame is rigidly attached and a nozzle that is considered a rigid body. The base body itself is assumed to be a rigid body of mass m_V with an inertial tensor $\boldsymbol{I}_V$ about S_B, located with position $\boldsymbol{r}_V$ with respect to S_B. In the nozzle is embedded the gimbal frame S_N, the motion of which with respect to S_B is described by the angular rate $\boldsymbol{\omega}_N$. The nozzle has mass m_N and inertial tensor $\boldsymbol{I}_N$ about S_N origin, and it is located at displacement $\boldsymbol{r}_N$ with respect to S_N. The origin of S_N is displaced from the origin of S_B by the vector $\boldsymbol{r}_C$.

As discussed in sec. 2.2 the total LV motion is described by its translational position, $\boldsymbol{\rho}$, its translational velocity, $\boldsymbol{\mu}$, and its angular rate $\boldsymbol{\omega}$, and it is assumed
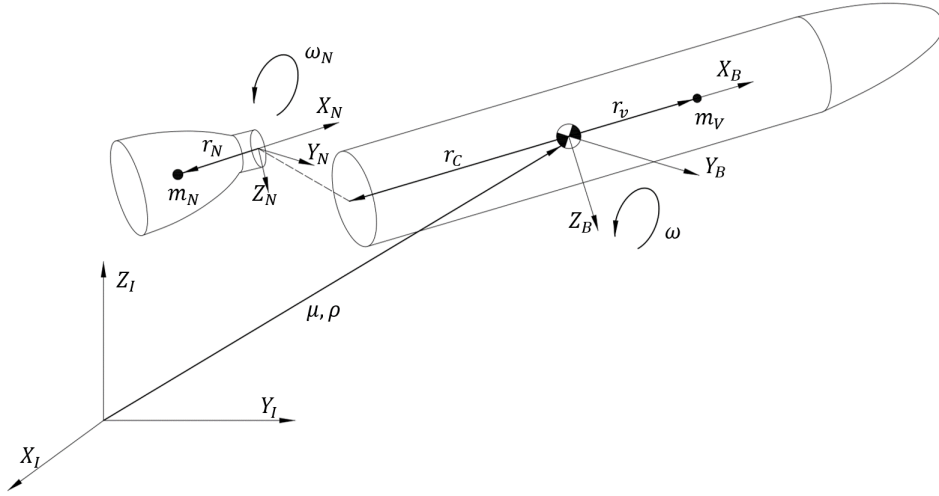
Figure 2.5. Total LV configuration geometry.

that the origin of the body frame corresponds to the location of the total LV c.g.. Remember that, an arbitrary vector u^I in S_I can be expressed in S_B by means of the following relation

$$\boldsymbol{u}^B = \boldsymbol{L}_{BI}\boldsymbol{u}^I \tag{2.52}$$

where $\boldsymbol{L}_{BI}$ is the matrix of direction cosines that transforms a vector from S_I to S_B. Hereafter, the superscript B is omitted for clarity. It is assumed that the variation of the intertial tensor $\boldsymbol{I}_N$ with respect to angular displacement is negligible for small rotations. Therefore, if S_B and S_N are normally aligned,

$$\boldsymbol{I}_N = \boldsymbol{L}_{BN}\boldsymbol{I}_N^N\boldsymbol{L}_{NB} \approx \boldsymbol{I}_N^N \tag{2.53}$$

Boltzmann-Hamel Equations Because we are interested in describing the coupling between the nozzle and LV dynamics, the motion of the total LV must be taken into account. The effects due to the nozzle rotation can be determined from generalized momenta of the total LV by using a modified form of Lagrange's equations. Consider the Lagrange's equations in the classical form for an unconstrained system, that are

$$\frac{d}{dt}\left(\frac{\partial \mathcal{L}}{\partial \dot{\kappa}_i}\right) - \frac{\partial \mathcal{L}}{\partial \kappa_i} = \mathcal{Q}_i \tag{2.54}$$

where $\mathcal{L} = \mathcal{T} - \mathcal{V}$, $\mathcal{T}$ and $\mathcal{V}$ are kinetic and potential energy, respectively, κ_i is each holonomic generalized coordinate and $\mathcal{Q}_i$ is the generalized force associated with that coordinate. According to [73, 9], for this special class of system, we have that

$\frac{\partial \mathcal{T}}{\partial \kappa_i} = 0$ and that there are no position depend-terms. Therefore, Eq. (2.54) can be rewritten in vector form as

$$\frac{d}{dt}\left(\nabla_{\dot{\kappa}}\mathcal{T}\right) = \mathcal{Q} \tag{2.55}$$

Note that, if LV and nozzle coordinates of motion are described with respect to the body frame S_B having a nonzero translation and angular velocity with respect to S_I, the Lagrange's equations can not be applied directly, since a subset of the motion coordinates are non-holonomic coordinates. However, without loss of generality, a state vector of true velocity can be defined as

$$\dot{\boldsymbol{\kappa}} = \boldsymbol{C}\boldsymbol{u} = \boldsymbol{C}\begin{bmatrix}\boldsymbol{\mu} \\ \boldsymbol{\omega}\end{bmatrix} \tag{2.56}$$

where, the holonomic velocities are given by the kinematic integral of the non-holonomic or quasi-velocities $\boldsymbol{u}$, and $\boldsymbol{C}$ is a kinetic transformation $\boldsymbol{L}_{BI}$ that expresses the velocity $\boldsymbol{u}$ in S_I. Introducing the transformed coordinates into Eq. (2.55), one can find

$$\boldsymbol{C}\frac{d}{dt}\left(\nabla_u\mathcal{T}\right) + \dot{\boldsymbol{C}}\nabla_u\mathcal{T} = \mathcal{Q}_{\boldsymbol{u}} \tag{2.57}$$

Recall that $\boldsymbol{C}$ relates an inertial to a rotating frame and is always orthonormal, so $\boldsymbol{C}^T\boldsymbol{C} = \boldsymbol{I}$ and its time derivative $\dot{\boldsymbol{C}} = \boldsymbol{C}\boldsymbol{\omega}\times$, so Eq. (2.57) can be written as

$$\frac{d}{dt}\left(\nabla_u\mathcal{T}\right) + \boldsymbol{\omega} \times \nabla_u\mathcal{T} = \boldsymbol{C}^T\mathcal{Q}_{\boldsymbol{u}} \tag{2.58}$$

The expression (2.58) is a simplified vector form of the Boltzmann-Hamel equations, or Lagrange's equations in quasi-coordinates [75].

Therefore, in order to apply the Eq. (2.58), define first the total LV kinetic energy $\mathcal{T}$, expressed in terms of the translational and angular velocities of the S_B frame, augmented by the energy of the nozzle resulting from its local velocity with respect to S_B. Thus, $\mathcal{T}$ is given by the sum of the contributions of the base vehicle and nozzle, such that

$$\mathcal{T} = \mathcal{T}_V + \mathcal{T}_N \tag{2.59}$$

The velocity of the LV base body in the inertial frame is

$$\boldsymbol{V}_v = \boldsymbol{\mu} + \boldsymbol{\omega} \times \boldsymbol{r}_V \tag{2.60}$$

composed by the velocity of the reference frame and velocity due to the rotation of

S_B. Likewise, the nozzle velocity is

$$\boldsymbol{V}_N = \boldsymbol{\mu} + \boldsymbol{\omega} \times (\boldsymbol{r}_C + \boldsymbol{r}_N) + \boldsymbol{\omega}_N \times \boldsymbol{r}_N \tag{2.61}$$

where the additional angular velocity due to nozzle rotation with respect to S_B is taken into account. The elements of Eq. (2.59) can be expressed as

$$\boldsymbol{\mathcal{T}}_V = \frac{1}{2} m_V (\boldsymbol{\mu} + \boldsymbol{\omega} \times \boldsymbol{r}_V)^2 \tag{2.62}$$

$$\boldsymbol{\mathcal{T}}_N = \frac{1}{2} m_V (\boldsymbol{\mu} + \boldsymbol{\omega} \times (\boldsymbol{r}_C + \boldsymbol{r}_N) + \boldsymbol{\omega}_N \times \boldsymbol{r}_N)^2 \tag{2.63}$$

where the operator $(.)^2$ is the appropriate transpose-inner-product operator. Using the kinetic energies, the generalized momenta with respect to rigid body translation can be calculated to be

$$\nabla_{\boldsymbol{\mu}} \boldsymbol{\mathcal{T}}_V = m_V (\boldsymbol{\mu} + \boldsymbol{\omega} \times \boldsymbol{r}_V) \tag{2.64}$$

$$\nabla_{\boldsymbol{\mu}} \boldsymbol{\mathcal{T}}_N = m_N (\boldsymbol{\mu} + \boldsymbol{\omega} \times (\boldsymbol{r}_C + \boldsymbol{r}_N) + \boldsymbol{\omega}_N \times \boldsymbol{r}_N) \tag{2.65}$$

Therefore, the total generalized momentum is

$$\nabla_{\boldsymbol{\mu}} \boldsymbol{\mathcal{T}} = (m_V + m_N)\boldsymbol{\mu} - (m_V \boldsymbol{r}_V + m_N(\boldsymbol{r}_C + \boldsymbol{r}_N)) \times \boldsymbol{\omega} - m_N \boldsymbol{r}_N \times \boldsymbol{\omega}_N \tag{2.66}$$

Note that if $m_v + m_N = m$ and, because we have assumed that the origin of S_B is at c.g. of the total vehicle,

$$m_V \boldsymbol{r}_V + m_N(\boldsymbol{r}_C + \boldsymbol{r}_N) = 0 \tag{2.67}$$

and therefore, the total linear momentum of the total LV is

$$\nabla_{\boldsymbol{\mu}} \boldsymbol{\mathcal{T}} = m\boldsymbol{\mu} - m_N \boldsymbol{r}_N \times \boldsymbol{\omega}_N \tag{2.68}$$

The last term in Eq. (2.68) is the components in momentum due to angular velocity of nozzle and it is the lateral effect of TWD inertial coupling.

Moreover, the generalized momentum with respect to the angular velocity $\boldsymbol{\omega}$ is found to have the components

$$\nabla_{\boldsymbol{\omega}}\boldsymbol{\mathcal{T}}_V = m_V \boldsymbol{r}_V \times \boldsymbol{\mu} + m_V \boldsymbol{r}_V \times \boldsymbol{\omega} \times \boldsymbol{r}_V \tag{2.69}$$

$$\nabla_{\boldsymbol{\omega}}\boldsymbol{\mathcal{T}}_N = m_N (\boldsymbol{r}_C + \boldsymbol{r}_N) \times \boldsymbol{\mu} + m_N (\boldsymbol{r}_C + \boldsymbol{r}_N) \times \boldsymbol{\omega} \times (\boldsymbol{r}_C + \boldsymbol{r}_N)$$
$$+ m_N (\boldsymbol{r}_C + \boldsymbol{r}_N) \times \boldsymbol{\omega}_N \times \boldsymbol{r}_N \tag{2.70}$$

Employing also the identity

$$m_i \boldsymbol{r}_i \times \boldsymbol{\omega} \times \boldsymbol{r}_i = \boldsymbol{I}_i \boldsymbol{\omega} \qquad i = V, N \tag{2.71}$$

and again assuming that the origin of S_B is the c.g., the resultant simplifications yield

$$\nabla_{\boldsymbol{\omega}}\boldsymbol{T}_V = \boldsymbol{I}_V \times \boldsymbol{\omega} \tag{2.72}$$

$$\nabla_{\boldsymbol{\omega}}\boldsymbol{T}_N = \boldsymbol{I}_N \times \boldsymbol{\omega} + m_N (\boldsymbol{r}_C + \boldsymbol{r}_N) \times \boldsymbol{\omega}_N \times \boldsymbol{r}_N \tag{2.73}$$

Finally, the nozzle momentum can be expanded such that

$$\nabla_{\boldsymbol{\omega}}\boldsymbol{T}_N = \boldsymbol{I}_N \boldsymbol{\omega} - \boldsymbol{r}_C \times m_N \boldsymbol{r}_N \times \boldsymbol{\omega}_N + m_N \boldsymbol{r}_N \times \boldsymbol{\omega}_N \times \boldsymbol{r}_N \tag{2.74}$$

Note that the last term is the nozzle inertia about the gimbal pivot point, thus Eq. (2.74) can be rewritten as

$$\nabla_{\boldsymbol{\omega}}\boldsymbol{T}_N = \boldsymbol{I}_N \boldsymbol{\omega} + (\boldsymbol{I}_N - \boldsymbol{r}_C \times m_N \boldsymbol{r}_N \times) \boldsymbol{\omega}_N \tag{2.75}$$

Then, being $\boldsymbol{I}_V + \boldsymbol{I}_N = \boldsymbol{I}$ the total LV inertia, the total angular momentum with respect to S_B is

$$\nabla_{\boldsymbol{\omega}}\boldsymbol{T} = \boldsymbol{I}\boldsymbol{\omega} + (\boldsymbol{I}_N - \boldsymbol{r}_C \times m_N \boldsymbol{r}_N \times) \boldsymbol{\omega}_N \tag{2.76}$$

Similarly to translational case, the last term in Eq. (2.76) is the angular effect of TWD.

Finally, the effect of the nozzle rotation in terms of generalized forces and moments can be computed directly from the generalized momenta terms due to TWD in Eqs. (2.68) (2.76) and the application of the Boltzmann-Hamel equations (see Eq. (2.58)), resulting to be

$$\boldsymbol{F}_N = -m_N \boldsymbol{r}_N \times \dot{\boldsymbol{\omega}}_N + \boldsymbol{\omega} \times (-m_N \boldsymbol{r}_N \times \boldsymbol{\omega}_N) \tag{2.77}$$

$$\boldsymbol{M}_N = (\boldsymbol{I}_N - \boldsymbol{r}_C \times m_N \boldsymbol{r}_N \times) \dot{\boldsymbol{\omega}}_N + \boldsymbol{\omega} \times (\boldsymbol{I}_N - \boldsymbol{r}_C \times m_N \boldsymbol{r}_N \times) \boldsymbol{\omega}_N \tag{2.78}$$

The force and moment components in scalar form are obtained using the expres-

sions relative to the S_B for the arms $\boldsymbol{r}_C$ and $\boldsymbol{r}_N$,

$$
\boldsymbol{r}_C = \begin{bmatrix} -l_c \\ 0 \\ 0 \end{bmatrix} \qquad \boldsymbol{r}_N = \begin{bmatrix} -l_N \cos(\beta_y)\cos(\beta_z) \\ -l_N \sin(\beta_y)\cos(\beta_z) \\ -l_N \sin(\beta_z) \end{bmatrix} \tag{2.79}
$$

for the nozzle angular rate $\boldsymbol{\omega}_N$ and its derivative $\dot{\boldsymbol{\omega}}_N$,

$$
\boldsymbol{\omega}_N = \begin{bmatrix} -\sin(\beta_y)\dot{\beta}_z \\ \cos(\beta_y)\dot{\beta}_z \\ -\dot{\beta}_y \end{bmatrix} \tag{2.80}
$$

$$
\dot{\boldsymbol{\omega}}_N = \begin{bmatrix} -\sin(\beta_y)\ddot{\beta}_z - \cos(\beta_y)\dot{\beta}_y\dot{\beta}_z \\ -\sin(\beta_y)\dot{\beta}_y\dot{\beta}_z + \cos(\beta_y)\ddot{\beta}_z \\ -\ddot{\beta}_y \end{bmatrix} \tag{2.81}
$$

and assuming that the inertia of the nozzle $\boldsymbol{I}_N$ is diagonal matrix as follows

$$
\boldsymbol{I}_N = \begin{bmatrix} I_{N_x} & 0 & 0 \\ 0 & I_{N_y} & 0 \\ 0 & 0 & I_{N_z} \end{bmatrix} \tag{2.82}
$$

Therefore, the components of force and moment in body frame S_B due to the nozzle displacement are

$$
\begin{aligned}
F_{N_{x_b}} =\, & m_N l_N (q \cos(\beta_z)\dot{\beta}_z + r \sin(\beta_y)\sin(\beta_z)\dot{\beta}_z \\
& - r \cos(\beta_y)\cos(\beta_z)\dot{\beta}_y) + m_N(-l_N(-\sin(\beta_y)\dot{\beta}_y\dot{\beta}_z \\
& + \cos(\beta_y)\ddot{\beta}_z)\sin(\beta_z) - l_N \sin(\beta_y)\cos(\beta_z)\ddot{\beta}_y)
\end{aligned} \tag{2.83}
$$

$$
\begin{aligned}
F_{N_{y_b}} =\, & -m_N l_N (p \cos(\beta_z)\dot{\beta}_z + r \sin(\beta_y)\cos(\beta_z)\dot{\beta}_y \\
& + r \sin(\beta_z)\cos(\beta_y)\dot{\beta}_z) + m_N(-l_N(\sin(\beta_y)\ddot{\beta}_z \\
& + \cos(\beta_y)\dot{\beta}_y\dot{\beta}_z)\sin(\beta_z) + l_N \cos(\beta_y)\cos(\beta_z)\ddot{\beta}_y)
\end{aligned} \tag{2.84}
$$

$$
\begin{aligned}
F_{N_{z_b}} =\, & m_N l_N (-\sin(\beta_y)\sin(\beta_z)\dot{\beta}_z + \cos(\beta_y)\cos(\beta_z)\dot{\beta}_y)p \\
& + m_N l_N (\sin(\beta_y)\cos(\beta_z)\dot{\beta}_y \\
& + \sin(\beta_z)\cos(\beta_y)\dot{\beta}_z)q + m_N l_N \cos(\beta_z)\ddot{\beta}_z
\end{aligned} \tag{2.85}
$$

$$
\begin{aligned}
M_{N_{x_b}} =& I_{N_x}(-\sin(\beta_y)\ddot{\beta}_z - \cos(\beta_y)\dot{\beta}_y\dot{\beta}_z) \\
&+ (-I_{N_z}\dot{\beta}_y - m_N l_N l_c(-\sin(\beta_y)\sin(\beta_z)\dot{\beta}_z \\
&+ \cos(\beta_y)\cos(\beta_z)\dot{\beta}_y))q \\
&- (I_{N_y}\cos(\beta_y)\dot{\beta}_z + m_N l_N l_c \cos(\beta_z)\dot{\beta}_z)r
\end{aligned}
\tag{2.86}
$$

$$
\begin{aligned}
M_{N_{y_b}} =& -I_{N_x} r \sin(\beta_y)\dot{\beta}_z + I_{N_y}(-\sin(\beta_y)\dot{\beta}_y\dot{\beta}_z + \cos(\beta_y)\ddot{\beta}_z) \\
&+ m_N l_N l_c \cos(\beta_z)\ddot{\beta}_z \\
&- (-I_{N_z}\dot{\beta}_y - m_N l_N l_c(-\sin(\beta_y)\sin(\beta_z)\dot{\beta}_z \\
&+ \cos(\beta_y)\cos(\beta_z)\dot{\beta}_y))p
\end{aligned}
\tag{2.87}
$$

$$
\begin{aligned}
M_{N_{z_b}} =& I_{N_x} q \sin(\beta_y)\dot{\beta}_z - I_{N_z}\ddot{\beta}_y \\
&- m_N l_c(-l_N(\sin(\beta_y)\ddot{\beta}_z + \cos(\beta_y)\dot{\beta}_y\dot{\beta}_z)\sin(\beta_z) \\
&+ l_N \cos(\beta_y)\cos(\beta_z)\ddot{\beta}_y) \\
&+ (I_{N_y}\cos(\beta_y)\dot{\beta}_z + m_N l_N l_c \cos(\beta_z)\dot{\beta}_z)p
\end{aligned}
\tag{2.88}
$$

2.2.3 Complete nonlinear equations

In collecting and summarizing the results obtained thus far, the nonlinear equation of motion describing the LV dynamics during the ascent flight can be readily written in scalar form as follows

$$
\begin{aligned}
m\big(\dot{u} + qw - rv\big) =& T_s + T_c \cos\beta_y \cos\beta_z - \frac{1}{2}\rho V^2 S C_{D_0} \\
&+ m_N l_N[(q\cos(\beta_z) + r\sin(\beta_y)\sin(\beta_z))\dot{\beta}_z \\
&- r\cos(\beta_y)\cos(\beta_z)\dot{\beta}_y + \sin(\beta_y)\sin(\beta_z)\dot{\beta}_y\dot{\beta}_z \\
&- \cos(\beta_y)\sin(\beta_z)\ddot{\beta}_z - \sin(\beta_y)\cos(\beta_z)\ddot{\beta}_y]
\end{aligned}
\tag{2.89}
$$

$$
\begin{aligned}
m\big(\dot{v} + ru - pw\big) =& T_c \cos\beta_z \sin\beta_y - \frac{1}{2}\rho V^2 S C_{C_\beta}\beta \\
&- m_N l_N[(p\cos(\beta_z) + r\sin(\beta_z)\cos(\beta_y))\dot{\beta}_z \\
&+ r\sin(\beta_y)\cos(\beta_z)\dot{\beta}_y - \cos(\beta_y)\sin(\beta_z)\dot{\beta}_y\dot{\beta}_z \\
&- \sin(\beta_y)\sin(\beta_z)\ddot{\beta}_z + \cos(\beta_y)\cos(\beta_z)\ddot{\beta}_y]
\end{aligned}
\tag{2.90}
$$

$$
\begin{aligned}
m\big(\dot{w} + pv - qu\big) =& T_c \sin\beta_z - \frac{1}{2}\rho V^2 S C_{N_\alpha}\alpha \\
&+ m_N l_N[(-\sin(\beta_y)\sin(\beta_z)\dot{\beta}_z + \cos(\beta_y)\cos(\beta_z)\dot{\beta}_y)p \\
&+ (\sin(\beta_y)\cos(\beta_z)\dot{\beta}_y + \sin(\beta_z)\cos(\beta_y)\dot{\beta}_z)q \\
&+ \cos(\beta_z)\ddot{\beta}_z]
\end{aligned}
\tag{2.91}
$$

$$
\begin{aligned}
I_{xx}\dot{p} - I_{xy}(\dot{q} - pr) &- I_{xz}(\dot{r} + pq) + I_{yz}(r^2 - q^2) + (I_{zz} - I_{yy})qr = \\
& I_{N_x}(-\sin(\beta_y)\ddot{\beta}_z - \cos(\beta_y)\dot{\beta}_y\dot{\beta}_z) \\
& + (-I_{N_z}\dot{\beta}_y - m_N l_N l_c(-\sin(\beta_y)\sin(\beta_z)\dot{\beta}_z \\
& + \cos(\beta_y)\cos(\beta_z)\dot{\beta}_y))q \\
& - (I_{N_y}\cos(\beta_y)\dot{\beta}_z + m_N l_N l_c\cos(\beta_z)\dot{\beta}_z)r
\end{aligned}
\tag{2.92}
$$

$$
\begin{aligned}
I_{yy}\dot{q} - I_{xy}(\dot{p} + qr) &- I_{yz}(\dot{r} + pq) + I_{xz}(p^2 - r^2) + (I_{xx} - I_{zz})pr = \\
& l_c T_c \sin\beta_z - \frac{1}{2}\rho V^2 S l_\alpha C_{N_\alpha}\alpha \\
& - I_{N_x}r\sin(\beta_y)\dot{\beta}_z + I_{N_y}(-\sin(\beta_y)\dot{\beta}_y\dot{\beta}_z + \cos(\beta_y)\ddot{\beta}_z) \\
& + m_N l_N l_c\cos(\beta_z)\ddot{\beta}_z \\
& - (-I_{N_z}\dot{\beta}_y - m_N l_N l_c(-\sin(\beta_y)\sin(\beta_z)\dot{\beta}_z \\
& + \cos(\beta_y)\cos(\beta_z)\dot{\beta}_y))p
\end{aligned}
\tag{2.93}
$$

$$
\begin{aligned}
I_{zz}\dot{r} - I_{xz}(\dot{p} - qr) &- I_{yz}(\dot{q} + pr) + I_{xz}(q^2 - p^2) + (I_{yy} - I_{xx})pq = \\
& - l_c T_c \cos\beta_z \sin\beta_y - \frac{1}{2}\rho V^2 S l_\beta C_{C_\beta}\beta \\
& I_{N_x}q\sin(\beta_y)\dot{\beta}_z - I_{N_z}\ddot{\beta}_y \\
& - m_N l_c(-l_N(\sin(\beta_y)\ddot{\beta}_z + \cos(\beta_y)\dot{\beta}_y\dot{\beta}_z)\sin(\beta_z) \\
& + l_N\cos(\beta_y)\cos(\beta_z)\ddot{\beta}_y) \\
& + (I_{N_y}\cos(\beta_y)\dot{\beta}_z + m_N l_N l_c\cos(\beta_z)\dot{\beta}_z)p
\end{aligned}
\tag{2.94}
$$

2.3   Linear rigid-body model
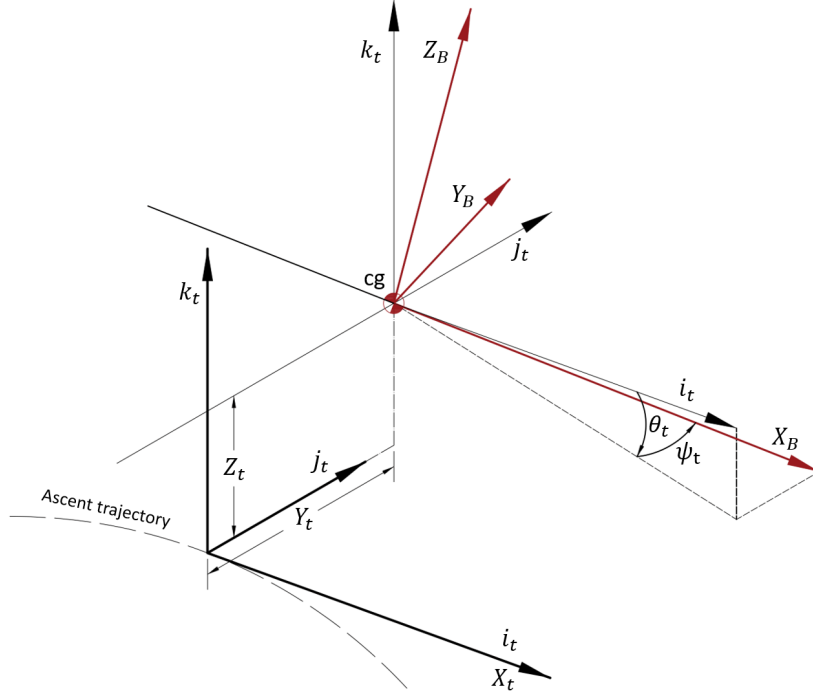
Figure 2.6. Sketch of trajectory S_t and S_B body frame.

In this section, the LV linearized model is devised in S_t, following the approach of Garner [10] with the purpose of deriving model suitable for the study of LV attitude control system, where perturbations of motion and attitude variables with respect to the reference trajectory are dealt with.

In this respect, the EOMs are written for a not-rotating Earth with respect to a not-stationary trajectory frame S_t that translates axially with the vehicle and rotates so as to remain tangent to the ascent reference trajectory (Fig. 2.6). The pitch θ_t and yaw ψ_t define the direction of LV longitudinal axis in the trajectory frame and Y_t, Z_t are the lateral deviations of the LV c.g. with respect to the reference trajectory.

Moreover, because the LV model considered in this thesis represents a symmetric LV configuration about the roll axis, the off-diagonal values in the moment of inertia tensor and the vehicle roll rate are assumed small, the couplings between pitch and yaw dynamics are ruled out, and a single rotational degree of freedom may be associated to either pitch or yaw motion. Therefore, in what follows, the model is developed for the simplified 3-DoF motion in the pitch plane, and the yaw plane equations are obtained by proceeding in the same way.
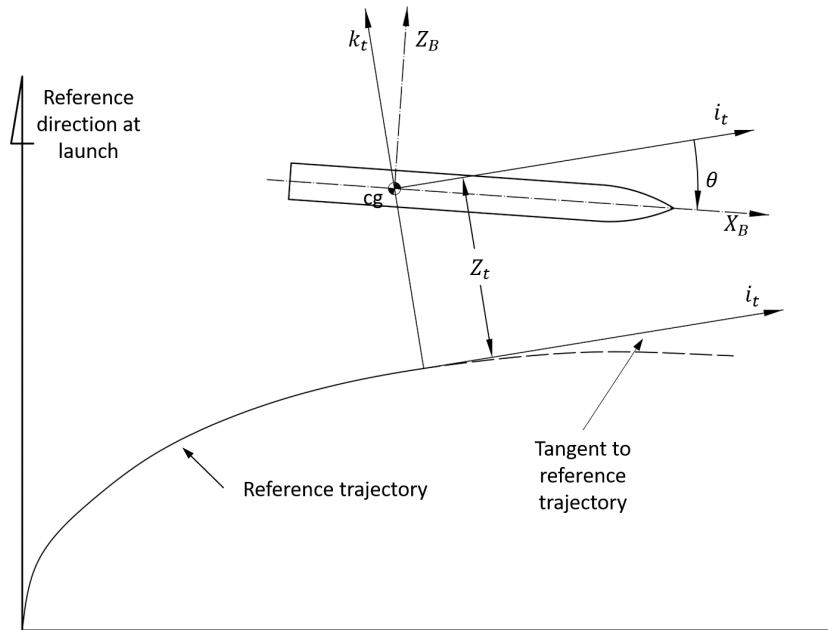
Figure 2.7. Pitch plane LV geometry.

Figure 2.7 shows a sketch of the LV in the pitch plane, whereas, Figure 2.8 shows the schematic representation of the LV with pertinent reference frames, the external forces and motion variables. In particular, we see the body frame S_B, the trajectory frame S_t and the launch base frame S_I. The angles θ and θ_c are also shown in Fig. 2.8, where θ_c is the attitude commanded by the pitch program of the guidance system and θ is the attitude of the vehicle respect to the local vertical at launch pad. The angle θ_c is obtained from the reference trajectory and represents the reference input to the FCS, while $\theta_t = \theta - \theta_c$ is the deviation from the desired direction X_t, and $\mathbf{V}$ is the instantaneous velocity of the vehicle relative to Earth. Moreover, γ is the angle between the velocity vector and X_t direction, and ψ_{ver} is the angle between the local vertical at a instant of flight time and the local vertical at a launch pad.

For a gravity turn trajectory the commanded pitch rate $\dot{\theta}_c$ is adjusted to cancel the component of gravitational acceleration normal to $\mathbf{V}$. In this case, for a reference condition, $\mathbf{V}$ is in the X_t direction and the angle γ is zero.

Given the velocity $\mathbf{V}$

$$\mathbf{V} = V \cos{(\gamma)}\hat{\mathbf{i}}_{\mathbf{t}} + V \sin{(\gamma)}\hat{\mathbf{k}}_{\mathbf{t}} \qquad (2.95)$$
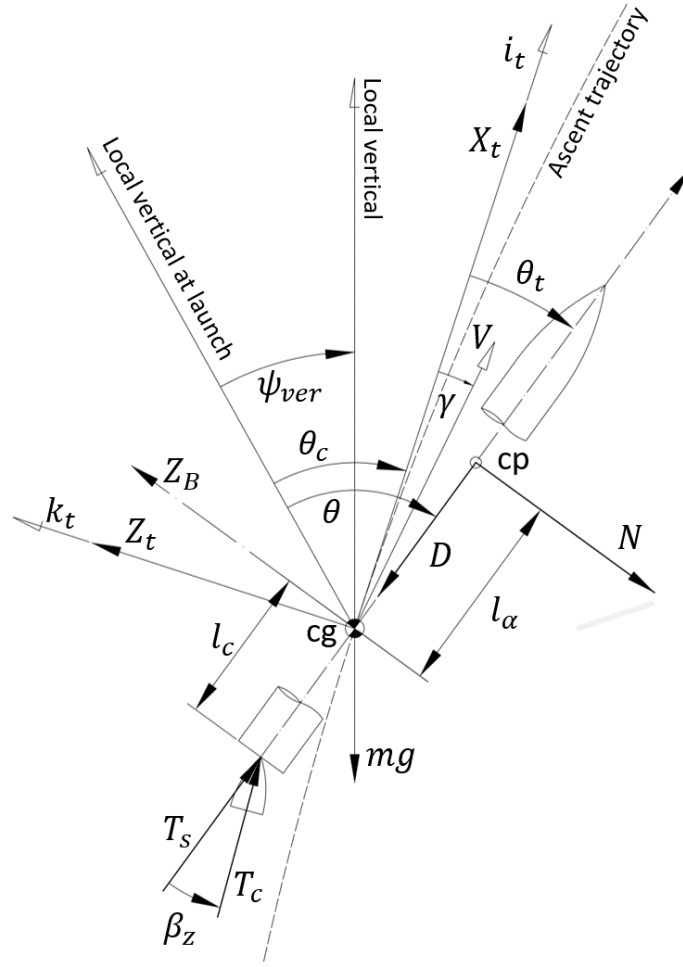
Figure 2.8. Sketch of LV model in the pitch plane.

the acceleration is expressed as

$$
\mathbf{A} = \frac{D\mathbf{V}}{dt} = \dot{V}\cos{(\gamma)}\hat{\mathbf{i}}_{\mathbf{t}} - V\sin{(\gamma)}\dot{\gamma}\hat{\mathbf{i}}_{\mathbf{t}} + V\cos{(\gamma)}\frac{d\hat{\mathbf{i}}_{\mathbf{t}}}{dt} \\
+ \dot{V}\sin{(\gamma)}\hat{\mathbf{k}}_{\mathbf{t}} + V\cos{(\gamma)}\dot{\gamma}\hat{\mathbf{k}}_{\mathbf{t}} + V\sin{(\gamma)}\frac{d\hat{\mathbf{k}}_{\mathbf{t}}}{dt} \tag{2.96}
$$

The frame S_t has angular velocity

$$
\boldsymbol{\omega} = \dot{\theta}_c\hat{\mathbf{j}}_{\mathbf{t}} \tag{2.97}
$$

so that

$$\frac{d\hat{\mathbf{i}}_\mathbf{t}}{dt} = \boldsymbol{\omega} \times \hat{\mathbf{i}}_\mathbf{t} = \dot{\theta}_c \hat{\mathbf{j}}_\mathbf{t} \times \hat{\mathbf{i}}_\mathbf{t} = -\dot{\theta}_c \hat{\mathbf{k}}_\mathbf{t} \qquad (2.98)$$

$$\frac{d\hat{\mathbf{k}}_\mathbf{t}}{dt} = \boldsymbol{\omega} \times \hat{\mathbf{k}}_\mathbf{t} = \dot{\theta}_c \hat{\mathbf{j}}_\mathbf{t} \times \hat{\mathbf{k}}_t = \dot{\theta}_c \hat{\mathbf{i}}_\mathbf{t} \qquad (2.99)$$

and the acceleration in Eq. (2.96) becomes

$$\mathbf{A} = \left[\dot{V}\cos(\gamma) - V\sin(\gamma)\dot{\gamma} + V\sin(\gamma)\dot{\theta}_c\right]\hat{\mathbf{i}}_\mathbf{t}$$
$$+ \left[\dot{V}\sin(\gamma) + V\cos(\gamma)\dot{\gamma} - V\cos(\gamma)\dot{\theta}_c\right]\hat{\mathbf{k}}_\mathbf{t} \qquad (2.100)$$

By observing that

$$\ddot{X}_t = \frac{d}{dt}\left(\dot{X}_t\right) = \dot{V}\cos(\gamma) - V\sin(\gamma)\dot{\gamma} = \frac{d}{dt}[V\cos(\gamma)] \qquad (2.101)$$

$$\ddot{Z}_t = \frac{d}{dt}\left(\dot{Z}_t\right) = \dot{V}\sin(\gamma) + V\cos(\gamma)\dot{\gamma} = \frac{d}{dt}[V\sin(\gamma)] \qquad (2.102)$$

Eq. (2.100) can be written as

$$\mathbf{A} = \left[\ddot{X}_t + V\sin(\gamma)\dot{\theta}_c\right]\hat{\mathbf{i}}_\mathbf{t} + \left[\ddot{Z}_t - V\cos(\gamma)\dot{\theta}_c\right]\hat{\mathbf{k}}_\mathbf{t} \qquad (2.103)$$

The EOM's, written in scalar form in S_t, are

$$m\left(\ddot{X}_t + V\sin(\gamma)\dot{\theta}_c\right) = F_{g_{x_t}} + F_{T_{x_t}} + F_{A_{x_t}} + F_{N_{x_t}} \qquad (2.104)$$

$$m\left(\ddot{Z}_t - V\cos(\gamma)\dot{\theta}_c\right) = F_{g_{z_t}} + F_{T_{z_t}} + F_{A_{z_t}} + F_{N_{z_t}} \qquad (2.105)$$

$$I_{yy}\ddot{\theta}_t = M_{T_{y_t}} + M_{A_{y_t}} + M_{N_{y_t}} \qquad (2.106)$$

where the subscript t indicates that the force and moment components are in S_t frame.

Since only the short-period mode is taken into consideration, the DoF along X_t is eliminated by allowing the origin of the coordinate system to move with velocity $\mathbf{V}$ and acceleration $\ddot{X}_t$, because its effects on vehicle stability are considered negligible [10, 72]. We can therefore obtain an approximate system of equations in the form

$$m\ddot{Z}_t = F_{T_{z_t}} + F_{A_{z_t}} + F_{N_{z_t}} + mV\cos(\gamma)\dot{\theta}_c - mg\sin(\theta_c - \psi_{ver}) \qquad (2.107)$$

$$I_{yy}\ddot{\theta}_t = M_{T_{y_t}} + M_{A_{y_t}} + M_{N_{y_t}} \qquad (2.108)$$

In Eq (2.107) the last two terms account for the difference between the centrifugal and gravitational acceleration. Most trajectory are shaped such that the vehicle flies

a gravity turn trajectory. For this condition, also called zero lift and zero angle of attack trajectory, the LV velocity $\mathbf{V}$ is aligned with the X_t direction (γ is zero) and pitch rate $\dot{\theta}_c$ is commanded such that

$$\dot{\theta}_c = \frac{g \sin \theta_c}{V} \tag{2.109}$$

Finally, considering that the angle ψ_{ver} is negligible during the entire boost phase of flight, thus $\psi_{ver} \ll \theta_c$, the two last terms of Eq. (2.107) are zero, and the equations that describe the lateral and rotational motion with respect to the reference trajectory become

$$m\ddot{Z}_t = F_{T_{z_t}} + F_{A_{z_t}} + F_{N_{z_t}} \tag{2.110}$$

$$I_{yy}\ddot{\theta}_t = M_{T_{y_t}} + M_{A_{y_t}} + M_{N_{y_t}} \tag{2.111}$$

2.3.1 Small-disturbance theory and reference state assumptions

In order to study the stability of the attitude motion, Eqs. (2.110) and (2.111), are linearized using the small-disturbance theory. To this end, we assume that the state variable are expressed as the sum of a reference state value identified by subscript 0 and a perturbation component with prefix Δ as follows

$$\ddot{Z}_t = \ddot{Z}_{t_0} + \Delta \ddot{z}_t \qquad \dot{Z}_t = \dot{Z}_{t_0} + \Delta \dot{z}_t \qquad Z_t = Z_{t_0} + \Delta z_t$$

$$\ddot{\theta}_t = \ddot{\theta}_{t_0} + \Delta \ddot{\theta}_t \qquad \dot{\theta}_t = \dot{\theta}_{t_0} + \Delta \dot{\theta}_t \qquad \theta_t = \theta_{t_0} + \Delta \theta_t$$

$$\beta_z = \beta_{z_0} + \Delta \beta_z \qquad \alpha = \alpha_0 + \Delta \alpha$$

The reference flight condition is specified using the so-called "time slice" approach which is standard practice in launcher control design [11, 10, 8], where time-varying mass and inertial properties are "frozen" over a short period of time. Moreover, the EOMs are linearized about different time point along the ascent trajectory, which, as said, is shaped such that the vehicle flies a gravity turn path. In this flight condition the LV longitudinal axis and $\mathbf{V}$ are aligned with the X_t direction, and, consequently, $\ddot{Z}_{t_0}$, $\dot{Z}_{t_0}$, Z_{t_0}, $\ddot{\theta}_{t_0}$, $\dot{\theta}_{t_0}$, θ_{t_0}, α_0 are zero and β_{z_0} is a small quantity that may be considered zero [9]. Thus, one has

$$\cos \theta_t = \cos(\theta_{t_0} + \Delta \theta_t) \approx \cos(\theta_{t_0}) - \Delta \theta_t \sin(\theta_{t_0}) = 1$$

$$\sin \theta_t = \sin(\theta_{t_0} + \Delta \theta_t) \approx \sin(\theta_{t_0}) + \Delta \theta_t \cos(\theta_{t_0}) = \Delta \theta_t$$

Introducing the small-diturbance notation into Eqs. (2.110) and (2.111), and incorporating the reference flight condition assumption noted above, the following

linear equations are obtained

$$m\Delta\ddot{z}_t = F_{T_{z_t 0}} + \Delta F_{T_{z_t}} + F_{A_{z_t 0}} + \Delta F_{A_{z_t}} + F_{N_{z_t 0}} + \Delta F_{N_{z_t}} \tag{2.112}$$

$$I_{yy}\Delta\ddot{\theta}_t = M_{T_{y_t 0}} + \Delta M_{T_{y_t}} + M_{A_{y_t 0}} + \Delta M_{A_{y_t}} + M_{N_{y_t 0}} + \Delta M_{N_{y_t}} \tag{2.113}$$

Finally, eliminating the reference state terms, that is, the reference forces and moments from Eqs. (2.112) and (2.113), that become

$$m\Delta\ddot{z}_t = \Delta F_{T_{z_t}} + \Delta F_{A_{z_t}} + \Delta F_{N_{z_t}} \tag{2.114}$$

$$I_{yy}\Delta\ddot{\theta}_t = \Delta M_{T_{y_t}} + \Delta M_{A_{y_t}} + \Delta M_{N_{y_t}} \tag{2.115}$$

2.3.2 Force and moments

In this section the expressions of force and moment presented in section 2.2.2 are expressed with respect to the trajectory axes and linearized by using the small-perturbance theory, that assumes all the perturbation components and their derivatives to be small, so that their squares and products are negligible compared to first-order quantities.

Thrust

The thrust force and moment components are

$$F_{T_{z_t}} = -(T_s + T_c \cos\beta_z)\sin\theta_t + T_c \sin\beta_z \cos\theta_t \tag{2.116}$$

$$M_{T_{y_t}} = T_{c_0}\sin(\beta_z)l_c \tag{2.117}$$

Therefore, performing the linearization, force and moment perturbation components of the thrust are

$$\Delta F_{T_{z_t}} = -(T_{s_0} + T_{c_0})\Delta\theta_t + T_{c_0}\Delta\beta_z \tag{2.118}$$

$$\Delta M_{T_{y_t}} = T_{c_0}l_c\Delta\beta_z \tag{2.119}$$

Aerodynamics

The aerodynamic force and moment components are expressed as

$$F_{A_{z_t}} = D\sin(\theta_t) - N\cos(\theta_t) \tag{2.120}$$

$$M_{A_{y_t}} = Nl_\alpha \tag{2.121}$$

thus, the linearized perturbation expressions are

$$\Delta F_{A_{z_t}} = D_0 \Delta \theta_t - \Delta N \tag{2.122}$$

$$\Delta M_{A_{y_t}} = \Delta N l_\alpha \tag{2.123}$$

where N and D are normal and drag forces in S_B, discussed already in section 2.2.2, being $D = D_0 + o(\alpha^2)$ and $N = N_\alpha \alpha$. Therefore, it is

$$\Delta N = N_\alpha \Delta \alpha \tag{2.124}$$

In order to completely define the aerodynamic forces, it is necessary to define the perturbed angle of attack with respect to the trajectory frame. Therefore, considering Eq. 2.50 and recalling that in reference flight condition $\alpha_0 = 0$, the perturbed angle of attack is

$$\alpha = \frac{w}{U_0} \tag{2.125}$$

Then, using the relation between the body axis velocity components and the trajectory axis velocity

$$u = \dot{X}_t \cos \theta_t - \dot{Z}_t \sin \theta_t \tag{2.126}$$

$$w = \dot{X}_t \sin \theta_t + \dot{Z}_t \cos \theta_t \tag{2.127}$$

that, assuming $u = U_0 + \Delta u$ and $w = W_0 + \Delta w$, in linear form are

$$U_0 + \Delta u = \dot{X}_{t_0} + \Delta \dot{x}_t \rightarrow U_0 = \dot{X}_{t_0} \tag{2.128}$$

$$\Delta w = \dot{X}_{t_0} \Delta \theta_t + \Delta \dot{z}_t \tag{2.129}$$

Finally, recalling that in reference condition $\dot{X}_{t_0} = V_0$ and using Eqs. (2.128) and (2.129) in Eq. (2.125), the perturbed angle of attack is

$$\Delta \alpha = \frac{V_0 \Delta \theta_t + \Delta \dot{z}_t}{V_0} = \Delta \theta_t + \frac{\Delta \dot{z}_t}{V_0} \tag{2.130}$$

A more accurate formulation also takes into account the aerodynamic damping in the form $l_\alpha \Delta \dot{\theta}_t$ [9], and when a lateral wind is considered, Eq. (2.130) is rewritten as

$$\Delta \alpha = \theta_t + \frac{\Delta \dot{z}_t}{V_0} - \frac{l_\alpha \Delta \dot{\theta}_t}{V_0} - \alpha_w \tag{2.131}$$

where $\alpha_w = v_w / V_0$ is the wind-induced angle of attack and v_w the wind velocity.

Nozzle inertia

The planar linearized force and moment components due to the inertial effect of nozzle rotation are obtained linearized the Eq. (2.85) and (2.87) resulting to be

$$
\begin{aligned}
\Delta F_{N_{z_t}} = &- m_N l_N (-\Delta\beta_y \Delta\beta_z \Delta\dot{\beta}_z + \Delta\dot{\beta}_y)(p_0 + \Delta p) \\
&+ m_N l_N (\Delta\beta_y \Delta\dot{\beta}_y + \Delta\beta_z \Delta\dot{\beta}_z)(q_0 + \Delta q) + m_N l_N \Delta\ddot{\beta}_z
\end{aligned}
\tag{2.132}
$$

$$
\begin{aligned}
\Delta M_{N_{z_t}} = &- I_{N_x}(r_0 + \Delta r)\Delta\beta_y \Delta\dot{\beta}_z + I_{N_y}(\Delta\beta_y \Delta\dot{\beta}_y \Delta\dot{\beta}_z + \Delta\ddot{\beta}_z) \\
&m_N l_N l_c \Delta\dot{\beta}_z - (-I_{N_z}\Delta\dot{\beta}_y - m_N l_N l_c(\Delta\beta_y \Delta\dot{\beta}_z + \Delta\dot{\beta}_y))(p_0 + \Delta p)
\end{aligned}
\tag{2.133}
$$

where it is assumed that β_{y_0} and β_{z_0} are zero. Neglecting the higher order terms, the above equations becomes,

$$
\Delta F_{N_{z_t}} = m_N l_N \Delta\ddot{\beta}_z + m_N l_N p_0 \Delta\dot{\beta}_y
\tag{2.134}
$$

$$
\Delta M_{N_{z_t}} = (I_{N_y} + m_N l_c l_N)\Delta\ddot{\beta}_z + p_0(I_{N_z} + m_N l_c l_N)\Delta\dot{\beta}_y
\tag{2.135}
$$

where the second terms in the Eqs. (2.134) and (2.135) are coupling effects between yaw and pitch due to the roll motion. These terms can be neglected because the roll rate is typically controlled, and it is small during the ascent flight. Finally, introducing the latter simplification, the linear effects of the nozzle rotation are

$$
\Delta F_{N_{z_t}} = m_N l_N \Delta\ddot{\beta}_z
\tag{2.136}
$$

$$
\Delta M_{N_{z_t}} = (I_{N_y} + m_N l_c l_N)\Delta\ddot{\beta}_z
\tag{2.137}
$$

2.3.3 Linear equations collected

LV governing equations in linear form are obtained from Eqs (2.112) and (2.115) incorporating force and moment expressions reported in section 2.3.2, as

$$
m\Delta\ddot{z}_t = -(T_{s_0} + T_{c_0})\Delta\theta_t + T_{c_0}\Delta\beta_z + D_0\Delta\theta_t - N_\alpha\Delta\alpha + m_N l_N \Delta\ddot{\beta}_z
\tag{2.138}
$$

$$
I_{yy}\Delta\ddot{\theta}_t = T_{c_0}l_c\Delta\beta_z + N_\alpha l_\alpha \Delta\alpha + (I_{N_y} + m_N l_c l_N)\Delta\ddot{\beta}_z
\tag{2.139}
$$

Finally, using Eq. (2.131) for the angle of attack, one obtains

$$
\begin{aligned}
\Delta\ddot{z}_t = &\frac{D_0 - (T_{s_0} + T_{c_0}) - N_\alpha}{m}\Delta\theta_t - \frac{N_\alpha}{mV_0}\Delta\dot{z}_t + \frac{N_\alpha l_\alpha}{mV_0}\Delta\dot{\theta}_t \\
&+ \frac{T_{c_0}}{m}\Delta\beta_z + \frac{m_N l_N}{m}\Delta\ddot{\beta}_z + \frac{N_\alpha}{m}\alpha_w
\end{aligned}
\tag{2.140}
$$

$$\Delta \ddot{\theta}_t = \frac{N_\alpha l_\alpha}{I_{yy}} \left(\Delta \theta_t + \frac{\Delta \dot{z}_t}{V_0} - \frac{l_\alpha \Delta \dot{\theta}_t}{V_0} - \alpha_w \right) + \frac{T_{c_0} l_c}{I_{yy}} \Delta \beta_z \\ + \frac{I_{N_y} + m_N l_c l_N}{I_{yy}} \Delta \ddot{\beta}_z \tag{2.141}$$

2.4 Flexible body dynamics
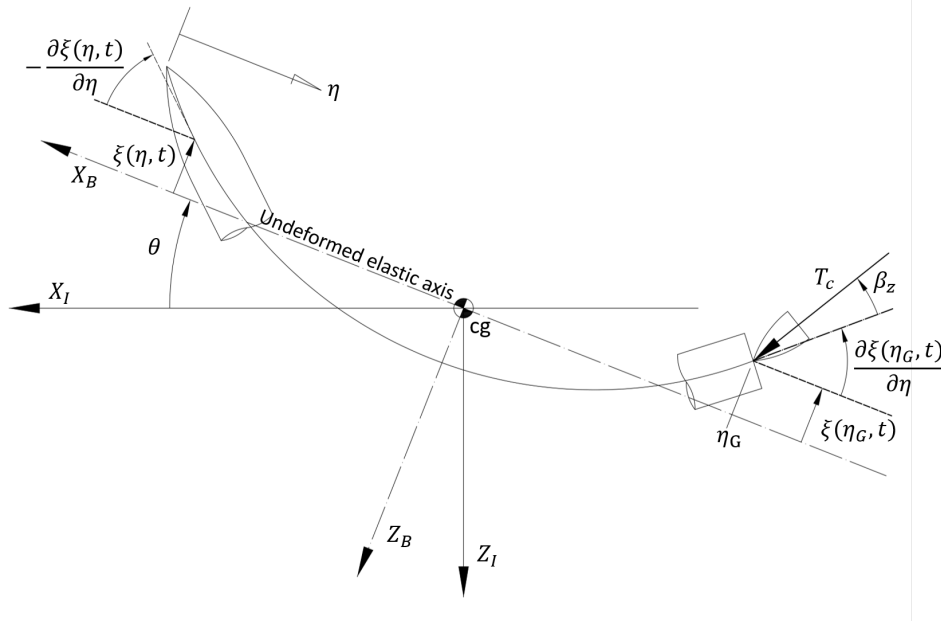
Figure 2.9. Sketch of relevant variables and parameters for the model of elastic DoFs.

In order to complete the vehicle model, the elastic DoFs are described, and to this end, the modal decomposition method [9] is exploited.

LV is assumed to be quasi-rigid, where free-free normal flexible modes are superimposed as small vibrations about the rigid body states. The bending modes are decoupled from the rigid motion and are exited by engine thrust and nozzle rotation inertial effect, whereas the aerodynamic effects are neglected. The latter assumptions are coherent when the class of LV having relatively constant cross-section over their length, with not major aerodynamic surfaces (fins, wing, etc.), and controlled by TVC with a nozzle located at the base of the rocket are considered [11, 54, 76, 77]. In particular, the aerodynamic forces, due to an elastic modal deflection, are low relative to the elastic forces and its effect is usually important only during the time of high dynamic pressure and can be ignored during the other flight times. A detailed review of the subject is contained in [78].

Relevant variables describing flexible dynamics are recalled in Fig. 2.9, where

a simple sketch of the deflected shape of the LV is reported, showing the elastic deflection $\xi(\eta, t)$, the longitudinal coordinate of the nozzle η_G, and the thrust control force T_c.

The elastic deflection at any point along the vehicle in S_B is given by

$$\xi(\eta, t) = \sum_{i=1}^{\infty} \Phi_i(\eta) q_i(t) \tag{2.142}$$

where η is the abscissa along the LV longitudinal axis (x_B), $\Phi_i(\eta)$ is the normalized mass i^{th} mode shape in the pitch plane, and $q_i(t)$ is the generalized coordinate of ith mode. The motion of each bending mode is approximated by a second-order system as follows

$$\ddot{q}_i + 2\zeta_i \omega_i \dot{q}_i + \omega_i^2 q_i = Q_i \tag{2.143}$$

where ω_i and ζ_i are the natural frequency and damping ratio of ith bending mode, respectively, and Q_i is the generalized force associated with the ith mode given by

$$Q_i = \int_0^L \left(\sum F_{z_b} \Phi_i(\eta) + \sum M_{z_b} \sigma_i(\eta) \right) d\eta \tag{2.144}$$

where F_{z_b} and M_{z_b} are the force and moment components due to aerodynamic, thrust and nozzle inertia, already discussed in Section 2.2.2. Being the local rotation σ_i

$$\sigma_i = -\frac{d\Phi_i}{d\eta}$$

Q_i depends on the moments and normal forces acting on the vehicle. According to [8, 34] the ith bending mode is exited primary by engine thrust and nozzle rotation. Therefore, Q_i is expressed, in linear form, as

$$\begin{aligned} Q_i &= \int_0^L \left[(-T_c \Delta \beta_z - m_N l_N \Delta \ddot{\beta}_z) \Phi_i(\eta) + (I_N \Delta \ddot{\beta}_z) \sigma_i(\eta) \right] d\eta \\ &= (-T_c \Delta \beta_z - m_N l_N \Delta \ddot{\beta}_z) \Phi_i(\eta_G) + (I_N \Delta \ddot{\beta}_z) \sigma_i(\eta_G) \end{aligned} \tag{2.145}$$

2.5   State-space model

A LV linear model suitable for the goal of this study is defined taking into account the rigid-body pitch axis rotational (Eq. (2.141)) and lateral drift dynamics (Eq. (2.140)) with respect to vehicle reference trajectory, together with contributions of first bending mode (Eq. (2.143)), whereas aerodynamic damping and tail-wags-dog (TWD) effects are neglected. The latter assumptions are coherent with the level of accuracy of the model and somewhat conservative, as TWD effects, that usually

occur at frequency between the first and second bending mode would be slightly stabilizing for the present LV configuration. Also, aerodynamic damping terms would influence the stability of elastic mode higher than first, while the effects on the rigid modes of the controlled LV are negligible [11].

Therefore, the equations of motion in linear form are

$$\ddot{\theta} = \frac{N_\alpha l_\alpha}{I_{yy}}\theta + \frac{N_\alpha l_\alpha}{I_{yy}V}\dot{z} + \frac{T_c l_c}{I_{yy}}\beta - \frac{N_\alpha l_\alpha}{I_{yy}}\alpha_w \tag{2.146}$$

$$\ddot{z} = \frac{D - T_t - N_\alpha}{m}\theta - \frac{N_\alpha}{mV}\dot{z} + \frac{T_c}{m}\beta + \frac{N_\alpha}{m}\alpha_w \tag{2.147}$$

$$\ddot{q} + 2\zeta_{BM}\omega_{BM}\dot{q} + \omega_{BM}^2 q = -\hat{\phi}_{TVC}T_c\beta \tag{2.148}$$

$$\alpha = \theta + \frac{\dot{z}}{V} - \alpha_w \tag{2.149}$$

where, eliminating the prefix "Δ" for the perturbed component of state variable, and subscripts "t" and "0" hereafter, for the sake of simplicity, z and $\dot{z}$ are, respectively, drift and drift rate of center of mass along the normal axis of the trajectory frame, θ is the perturbed pitch angle, q is the generalized coordinate of the first elastic mode. In the same manner, eliminating the subscript "z", β is the nozzle angle. Furthermore, ω_{BM}, ζ_{BM} and $\hat{\phi}_{TVC}$ are, respectively, first bending mode natural frequency, damping ratio and displacement component over generalized mass at TVC location.

In order to write the LV dynamics in state-space form

$$\dot{\mathbf{x}} = \mathbf{A}\mathbf{x} + \mathbf{B}\mathbf{u}, \qquad \mathbf{y} = \mathbf{C}\mathbf{x} + \mathbf{D}\mathbf{u} \tag{2.150}$$

the state vector, including rigid body and flex states, is defined as

$$\mathbf{x} = \begin{bmatrix} \theta & \dot{\theta} & z & \dot{z} & q & \dot{q} \end{bmatrix} \tag{2.151}$$

and the governing equations are written as

$$
\begin{bmatrix} \dot{z} \\ \ddot{z} \\ \dot{\theta} \\ \ddot{\theta} \\ \dot{q} \\ \ddot{q} \end{bmatrix} = \begin{bmatrix} 0 & 1 & 0 & 0 & 0 & 0 \\ 0 & -\frac{N_\alpha}{mV} & \frac{D-T_t-N_\alpha}{m} & 0 & 0 & 0 \\ 0 & 0 & 0 & 1 & 0 & 0 \\ 0 & \frac{N_\alpha l_\alpha}{I_{yy}}/V & \frac{N_\alpha l_\alpha}{I_{yy}} & 0 & 0 & 0 \\ 0 & 0 & 0 & 0 & 0 & 1 \\ 0 & 0 & 0 & 0 & -\omega_{BM}{}^2 & -2\zeta_{BM}\omega_{BM} \end{bmatrix} \begin{bmatrix} z \\ \dot{z} \\ \theta \\ \dot{\theta} \\ q \\ \dot{q} \end{bmatrix}
$$
$$
+ \begin{bmatrix} 0 \\ \frac{T_c}{m} \\ 0 \\ \frac{T_c l_c}{I_{yy}} \\ 0 \\ -\hat{\phi}_{TVC}T_c \end{bmatrix} \beta + \begin{bmatrix} 0 \\ \frac{N_\alpha}{m} \\ 0 \\ -\frac{N_\alpha l_\alpha}{I_{yy}} \\ 0 \\ 0 \end{bmatrix} \alpha_w \tag{2.152}
$$

According to typical notation for LV dynamic models [20], the following parameters are defined

$$
A_6 = \frac{N_\alpha l_\alpha}{I_{yy}} \quad K_1 = \frac{T_c l_c}{I_{yy}} \quad a_1 = -\frac{N_\alpha}{mV} \quad a_3 = \frac{T_c}{m} \quad a_4 = -\frac{(T_t - D)}{m} \tag{2.153}
$$

where A_6 and K_1 are dubbed, respectively, aerodynamic and control moment coefficient.

The output vector $\boldsymbol{y} = \begin{bmatrix} \theta_{INS} & \dot{\theta}_{INS} & z_{INS} & \dot{z}_{INS} \end{bmatrix}^T$, related to sensor measurements, where the contribution of flexible motion at sensor location is summed to that of rigid motion, is expressed as

$$
\mathbf{y} = \begin{bmatrix} \theta_{INS} \\ \dot{\theta}_{INS} \\ z_{INS} \\ \dot{z}_{INS} \end{bmatrix} = \begin{bmatrix} 0 & 0 & 1 & 0 & \sigma_{INS} & 0 \\ 0 & 0 & 0 & 1 & 0 & \sigma_{INS} \\ 1 & 0 & 0 & 0 & -\phi_{INS} & 0 \\ 0 & 1 & 0 & 0 & 0 & -\phi_{INS} \end{bmatrix} \begin{bmatrix} z \\ \dot{z} \\ \theta \\ \dot{\theta} \\ q \\ \dot{q} \end{bmatrix} \tag{2.154}
$$

where ϕ_{INS} and σ_{INS} represent, respectively, bending mode displacement and rotation components at the location of inertial navigation system (INS).

2.6   TVC actuators dynamics

The actuator dynamic model features two serially connected transfer functions, representing a second order model and a pure delay. The time delay $\tau = 20\,\text{ms}$, due to hardware processing times, is modelled through a second order Padé approximation, as

$$\begin{bmatrix} \dot{d} \\ \ddot{d} \end{bmatrix} = \begin{bmatrix} 0 & 1 \\ -\frac{12}{\tau^2} & -\frac{6}{\tau} \end{bmatrix} \begin{bmatrix} d \\ \dot{d} \end{bmatrix} + \begin{bmatrix} 0 \\ -\frac{12}{\tau^2} \end{bmatrix} \beta_c \tag{2.155}$$

$$\beta_{\hat{c}} = \dot{d} + \beta_c \tag{2.156}$$

where β_c and $\beta_{\hat{c}}$ are respectively, the TVC command and the same signal with delay. The transfer function of the TVC dynamics is

$$W_{TVC}(s) = \frac{\beta}{\beta_{\hat{c}}} = \frac{\omega_{TVC}^2}{s^2 + 2\zeta_{TVC}\omega_{TVC}s + \omega_{TVC}^2} \tag{2.157}$$

where ζ_{TVC} and ω_{TVC} are damping ration and natural frequency, the values of which are reported in Table 2.1.

The actuation chain model is completed by saturations that bound the gimbal angle and angular rate to $\pm 6\,\text{deg}$ and $10\,\text{deg/s}$ respectively.

2.7   Wind models

In this study, two different wind models are adopted for the synthesis and verification of the the flight control systems.

Deterministic Gust generator

A synthetic step-like wind gust has been specifically designed for stressing the system This wind profile, graphically depicted in Fig. 2.10(a), is represented by a piecewise continuous function of time:

- 0-45 s: a parabolic profile with magnitude varying between [0, 2.5] m/s

- 45-50 s: a linear profile with magnitude varying between [2.5, -30] m/s

- 50-100 s: an exponential profile with magnitude varying between [-30, 0] m/s

$$v_w(t) = \begin{cases} V_a \left(\frac{t}{t_a} \right)^2 & \text{for} \quad 0 \le t < t_a \\ (V_b - V_a)\frac{t-t_a}{t_b-t_a} + V_a & \text{for} \quad t_a \le t \le t_b \\ V_b e^{\frac{t-t_b}{t_f-t_b}\log\frac{0.1}{|V_b|}} & \text{for} \quad t_b < t \le t_f \end{cases} \tag{2.158}$$

where the coefficients are specified as $t_f = 100$ s, $t_a = 70$ s, $t_b = 75$ s, $V_a = 5$ m s^{-1}, $V_b = -30$ m s^{-1}.

Stochastic Gust generator

In order to stress and validate the flight control systems, a random wind disturbance is generated according to the most recent NASA guidelines [79], in the same fashion as in previous works dealing with atmospheric rocket attitude control [36, 76]. The wind is made of an altitude-dependent steady-state profile with shear envelope $v_{wp}(h)$ defined in Eq. (2.159) together with a stochastic wind gust $v_w(s,h)$. The envelope (blue line in Figure 2.10(b)) is characterized for the first 20 Km of altitude ($H_f = 20000$ m) by a constant gust amplitude $A = 14$ m/s, an exponential leading edge ($H_l = 2000$ m) and a 1-cosine shape trailing edge ($H_u = 2500$ m).

$$v_{wp}(h) = \begin{cases} 10A[(\frac{h}{H_l})^{0.9} - 0.9\frac{h}{H_l}] & \text{for} \quad 0 \leq h < H_l \\ A & \text{for} \quad H_l \leq h \leq H_f - H_u \\ \frac{A}{2}[1 - \cos(\frac{\pi}{H_u}(h - H_f))] & \text{for} \quad H_f - Hu < h \leq H_f \end{cases} \quad (2.159)$$

The stochastic wind velocity component v_w is modeled by coloring white noise n_w through a Dryden filter with the following transfer function

$$G_w(s,h) = \frac{v_w(s,h)}{n_w(s)} = \frac{\sqrt{\frac{2}{\pi}\frac{V(h)-v_{wp}(h)}{L(h)}\sigma^2(h)}}{s + \frac{V(h)-v_{wp}(h)}{L(h)}} \quad (2.160)$$

where $L(h)$ and $\sigma(h)$ are the turbulence length scale and the standard deviation versus altitude h and their values are given in tabular form in [79].
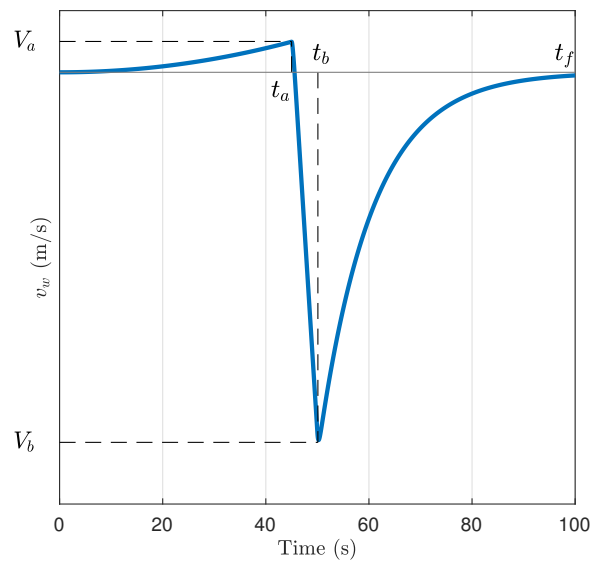
(a) Deterministic step-like wind gust profile.
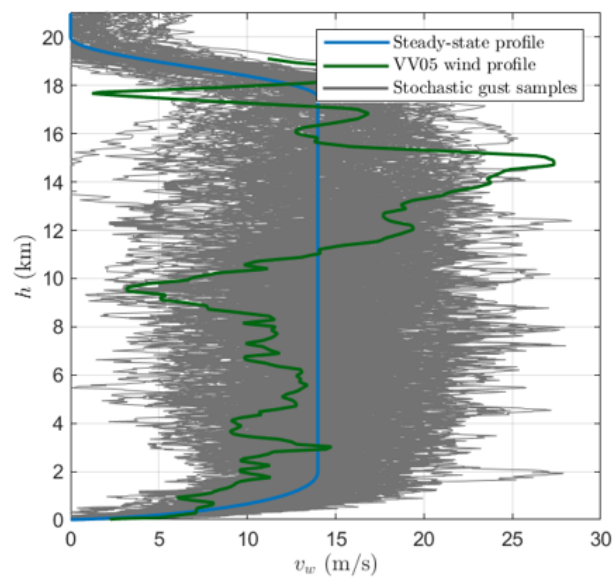
(b) Stochastic wind gust profile.

Figure 2.10. wind model

Figure 2.10(b) shows the estimated wind encountered in the VEGA VV05 mission (green line) and a few random samples of the stochastic gust (gray lines). Figure 2.10(b) visually confirms that a set of 100 samples are able to cover the estimated wind encountered in the VEGA VV05 mission (green line), similarly to what was done in [36, 76].

2.8 Time domain simulation model

The performance assessment of LV FCS is conducted by means of time-varying planar model of the atmospheric phase of flight. The vehicle dynamics are derived from a linear perturbation model that includes rigid and flexible dynamics, equations of which are presented in Sec. 2.5, and the TVC actuator dynamics reported in Sec. 2.6. In most instances, the presented time-varying linear model is sufficiently accurate to capture all relevant effects for attitude control design overcome difficulties encountered in using a model with many complex subsystems having nonlinear dynamics [8, 51]. In order to describe the perturbed motion about the reference trajectory of the LV all along the time span of ascent flight, the time-varying model is realized by varying the linear model parameters with time using scheduled look-up table.

The reference LV model, considered in this study, is representative of a medium-size vehicle (lift-off mass 120.000 kg) of the same payload class as VEGA and the detailed description of which can be found in Ref. [9].
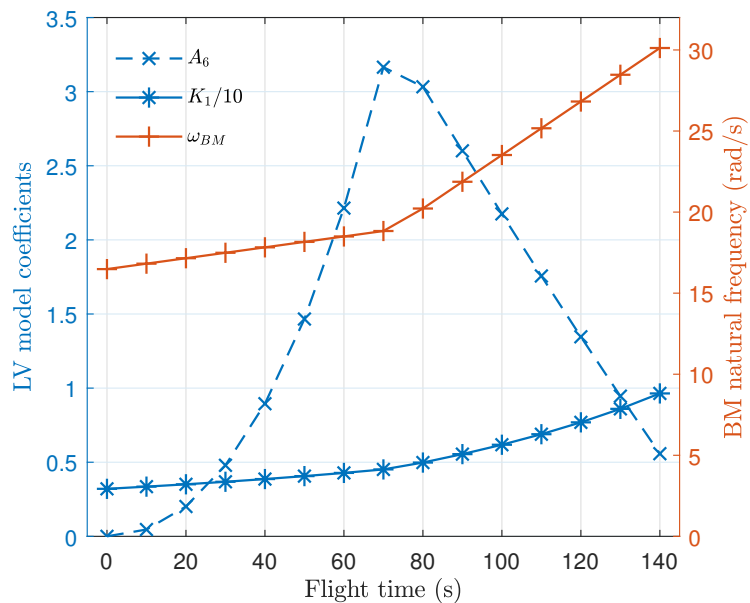
Figure 2.11. Aerodynamic and control moment coefficients, and bending mode natural frequency vs. flight time.

Variations of principal LV parameters, that is, A_6, K_1 and ω_{BM}, as functions of flight time are shown in Figure 2.11 for a representative ascent trajectory from launch pod through an altitude of 60 km. The complete set of model data at the maximum dynamic pressure (max-Q) condition ($t = 72$ s) is reported in Table 2.1[2].

---

[2]The LV model is freely available on GitHub https://github.com/AlessandroZavoli/Rocket-Attitude-Dynamics for FCS performance evaluation and benchmarking.

Table 2.1. LV model parameters at $t = 72$ s (max-Q condition).

	Unit	Value
m	kg	7.38×10^4
l_α	m	10.39
l_c	m	9.84
I_{yy}	$\mathrm{kg\,m^2}$	3.28×10^6
V	m/s	937.70
Alt	m	$15,143$
T_c	N	1.52×10^6
$T_t - D$	N	1.71×10^6
N_α	N/rad	1.07×10^6
A_6	$1/\mathrm{s}^2$	3.3818
K_1	$1/\mathrm{s}^2$	4.5647
a_1	$1/\mathrm{s}^2$	-0.0154
a_3	$1/\mathrm{s}^2$	20.6090
a_4	$1/\mathrm{s}^2$	-27.2710
ω_{BM}	rad/s	18.9
ζ_{BM}	-	0.005
ϕ_{INS}	-	0.8
σ_{INS}	rad/m	0.178
$\hat{\phi}_{TVC}$	1/kg	4.31×10^{-5}
ω_{TVC}	rad/s	70
ζ_{TVC}	-	0.7

Chapter 3

Baseline controller

3.1 Statement of the LV control problem

A prerequisite to the design of LV autopilot is the determination of mission profile, reference trajectory, and overall vehicle configuration. This task is accomplished by the guidance function that defines the reference trajectory in terms of position and velocity of the vehicle and thrust vector orientation. Usually, the guidance commands are suitably translated into pitch and yaw (or pitch and yaw rates) commands whose purpose is to orient the vehicle in a prescribed direction. Thus, the launch vehicle guidance system provides the pitch and yaw commands as reference input of the FCS.

Unlike traditional approaches to the design of the FCS, where the study of short-period dynamics may be carried out independently of the guidance problem, the two topics cannot be dealt with separately [11] when attitude control of a LV is taken into consideration. Attitude control has a significant influence on trajectory dispersion, because it is required to minimize trajectory deviations in terms of attitude error and lateral drift, and also to minimize the angle of attack in order to guarantee the structural integrity of the vehicle. Therefore, FCS design is conducted with multiple objectives, the first of which is to stabilize the short-period motion due to the fact that the LV is aerodynamically unstable and highly flexible.

In general, the principal tasks of the FCS are to achieve

- **Stability** with respect to

  - aerodynamic instability of vehicle
  - high flexibility

- **Performance** in terms of

  – aerodynamic load minimization

  – trajectory error minimization

- **Robustness** provided for

  – model parameter uncertainties

  – anticipated exogenous wind disturbances.

As aforementioned, LVs are usually aerodynamically unstable because the location of the aerodynamic center of pressure is forward of the vehicle center of gravity position. Hence, in order to provide adequate short-period stability, traditional FCS architectures control attitude angle and rate using proportional and derivative (PD) actions, as reported in Refs. [11, 34, 20, 10].

Further issues are caused by vehicle flexibility, particularly when bending mode and control frequencies are of the same order of magnitude. This problem arises because structural bending modes may be excited by control actions required for maneuvering and, without some form of compensation, resonance would amplify bending mode oscillations. According to conventional methods for stabilizing the bending modes, notch and low-pass filters are placed in the feedback loop. The problem is complicated by the fact that passive filtering may reduce gain and phase margins of the short-period control loop.

After stabilizing the short-period dynamics of the vehicle, it is necessary to examine the influence of the FCS on aerodynamic loads and trajectory tracking. Angle of attack variations due to winds gusts (especially in regions of high dynamic pressure) must be limited, to avoid loss of control. Angle of attack must also be controlled in order to limit aerodynamic moments. In this respect, a load relief feature is included in the control system, whose effect is to turn the vehicle into the wind direction to reduce the angle of attack, which may lead to attitude deviations as well as translational effects with respect to the reference trajectory.

The widely adopted control strategy, presented in the well-known monograph by Greensite [11, 62], to satisfy the two conflicting requirements adds an angle of attack feedback, that allows to manage angle of attack and lateral drift rate. Another control architecture with the same aim is presented in study on FCS for VEGA LV [20], based a PD controller on lateral drift. It is realized by placing proportional actions on the lateral drift and lateral drift rate measurements provided by an INS, that is able to maintain the launcher on the reference trajectory as well as to improve the wind gust response. The latter architecture is used in this study to design the attitude control system, that will be referenced as baseline controller (BC) in what follows.

3.2   Baseline controller
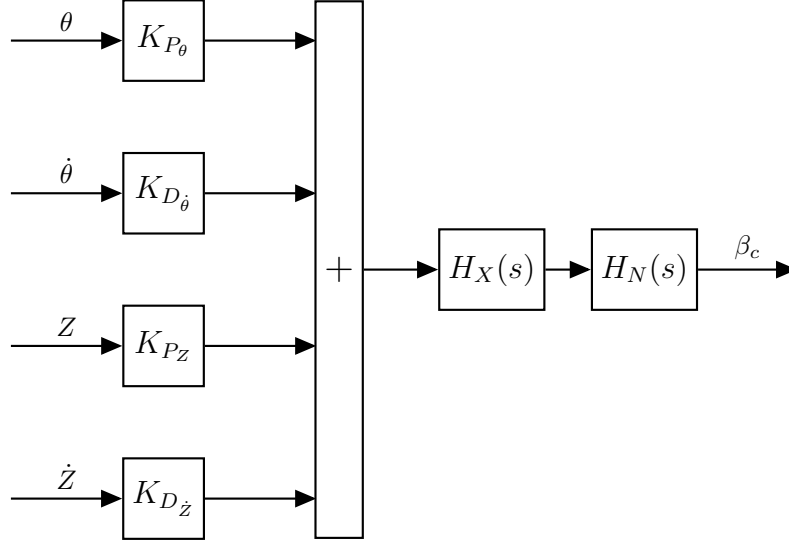
Figure 3.1. BC architecture.

As mentioned above, the goal of the FCS is to stabilize LV attitude motion, maintain the programmed trajectory and reject external disturbances, by acting on TVC nozzle deflections. The architecture of proposed BC is shown in Fig. 3.1 and features the classical PD components for attitude and lateral dynamics, plus filters to phase-stabilize and attenuate the bending modes [11, 10]. In more details, the controller includes

- a PD element on pitch angle θ channel with gains K_{P_θ} and K_{D_θ}

- a PD element on lateral displacement z (gain K_{P_z}) and drift velocity $\dot{z}$ (gain K_{D_z}), to maintain the launcher on the reference flight path and improve the response to wind gusts

- a second-order, non-minimum phase low-pass filter H_X to phase-stabilize the first bending mode

- a notch filter H_N to attenuate the bending-mode magnitude.

The controller is fed by the output vector $\boldsymbol{y} = \begin{bmatrix} \theta_{INS} & \dot{\theta}_{INS} & z_{INS} & \dot{z}_{INS} \end{bmatrix}^T$ (see Sec. 2.5), and the corresponding control law is described in the frequency domain as

$$\boldsymbol{K}_{BC}(s) = [K_{P_\theta} \quad K_{D_\theta} \quad K_{P_z} \quad K_{D_z}]H_X(s)H_N(s) \tag{3.1}$$

Table 3.1 shows a classical set of requirements for robust stability, in terms of stability margins, for the VEGA launcher [76], that, as said, is in the same weight class of LV model considered in this thesis (see Sec 2.8).

**Table 3.1.** FCS stability requirements.

Rigid-Body margins			Flexible-body margins	
Aero GM	Rigid DM	Rigid GM	Flex GM	Flex DM
≥ 6 dB	≥ 100 ms	≤ -6 dB	≤ -3 dB	≥ 50 ms

Table 3.2. FCS performance requirements.

Requirements	Metrics	Bounds
Aerodynamic load	$Q\alpha$	$< Q\alpha$ safety envelope
Lateral drift	z_{max}	< 500 m
Lateral rate drift	$\dot{z}_{max}$	< 15 m/s
TVC angle deflection	β_{max}	< 6 deg

In order to better understand the robust stability requirements is needed to analyze the system in frequency domain through Nichols plot. To this end, the open-loop system (controller, TVC actuator dynamic and LV model) is re-arranged and broken at the controller output in order to reduce the system to a SISO configuration. The Nichols plot of the open-loop frequency response at $t = 72$ s is shown in Fig. 3.2. The frequency response presents two groups of stability margins defined for each crossing frequency around the critical instability points. The first one includes low-frequency margins (frequency below 8.4 rad/s), namely Aero gain margin (GM), Rigid GM, and Rigid phase margin (PM), that are associated to the rigid-body dynamics (RB). The group of high-frequency margins (frequency above 8.4 rad/s), that is, Flex GM and Flex PM, refer to the bending mode (BM). The hump of the curve between the critical points confirms the bending mode attenuation and phase-stabilization realized by the filters. Phase Margin (PM) requirements are commonly expressed in terms of Delay Margin (DM), defined as $DM = PM/\omega_{0dB}$, where ω_{0dB} is the crossover frequency of the open loop system.

Performance requirements in Table 3.2 are verified through time-domain simulations by using the LTV model presented in Sec. 2.8. One of the requirements that must be met by FCS in atmospheric flight is to limit the structural loads within a given envelope defined on the flight time. This load requirement is expressed as $Q\alpha$, which is the product of the dynamic pressure Q and the angle of attack α. It is apparent that $Q\alpha$ is sensitive to wind disturbances and, therefore, the control
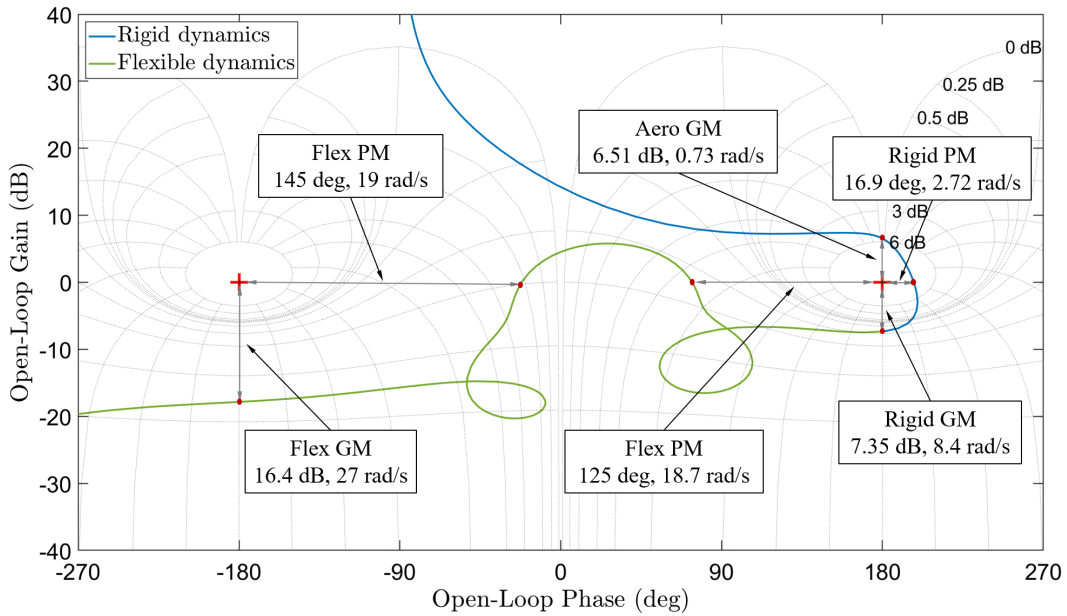
Figure 3.2. Nichols plot of open-loop response at $t = 72$ s.

law must be particularly robust against moderate and strong wind gusts at different altitudes. Furthermore, since the guidance is open-loop, the FCS must limit the lateral drift with respect to reference trajectory (z) and drift rate ($\dot{z}$). It is also important to limit the actuation effort in order to avoid TVC servo saturation.

FCS synthesis is conducted in several phases. First, a controller that achieves adequate short-period stability and performance is developed. Then, the bending mode stabilization is dealt with by designing compensator filters that provide appropriate gain and phase stabilization. Finally, the BC is completed by introducing the lateral drift and drift rate control.

As said above, in order to manage LV parameter variations over flight time, the BC synthesis process described above is to be repeated at specific design points along the reference trajectory. Therefore, controller gains and filter parameters are scheduled based on suitable variable, such as time or non-gravitational velocity. The scheduling time grid must be dense in order to obtain BC effective in managing the relevant variations of LV dynamical characteristics during the flight.

In what follows, the steps in BC synthesis are discussed with reference to the maximum dynamic pressure condition at $t = 72$ s.

3.2.1 Short-period stabilization

First requirement of FCS on LV stabilization is satisfied by means a PD controller on the attitude feedback channel, the design of which is conducted by considering

the rotational dynamics of the LV, obtained from the Eq. 2.146 having neglected lateral, TVC and bending mode dynamics [34], as

$$\ddot{\theta} = A_6 \theta + K_1 \beta \tag{3.2}$$

with transfer function relating θ to β as follows

$$\frac{\theta}{\beta} = G(s) = \frac{K_1}{s^2 - A_6} \tag{3.3}$$

The system poles are of $\pm\sqrt{A_6}$, with A_6 positive when the a.c. location is forward of the c.g., so that a root is in the right-half s-plane as shown in Fig. 3.3.
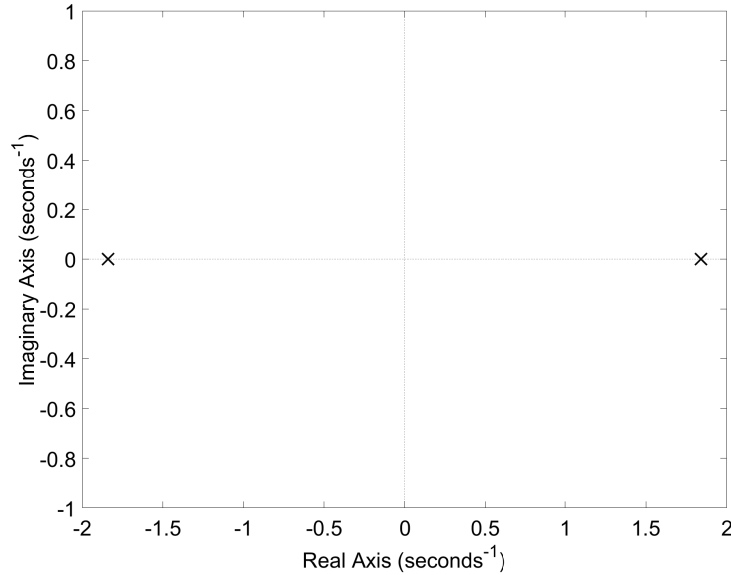
Figure 3.3. Location of rotational dynamics poles.

In order to stabilize the system, PD controller is used

$$K(s) = K_{P_\theta} + K_{D_\theta} s \tag{3.4}$$

and Fig. 3.4 shows the root locus when the PD controller is applied to the open-loop transfer function of Eq. (3.3). The zero introduced by the derivative component of PD controller attracts the pole with positive real part in the left-half of s-plane, achieving positive stability.

Suitable values of K_{P_θ} and K_{D_θ}, so as to satisfy the stability margin requirements, are obtained by enforcing the following conditions

  i) 6 dB gain margin at low frequency
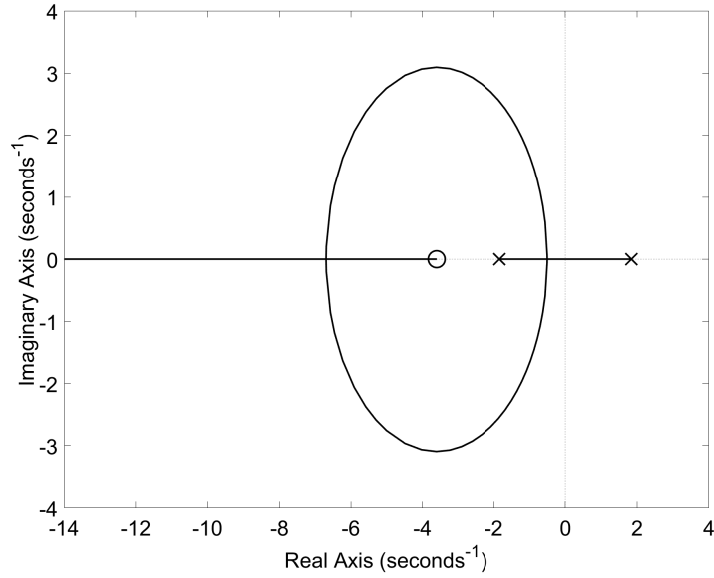
Figure 3.4. Root locus of the open loop system $K(s)G(s)$ for positive variations of K_{P_θ}.

ii) 30 deg phase margin at high frequency

for the open-loop transfer function of the controlled system

$$K(s)G(s) = \frac{K_1(K_{D_\theta}s + K_{P_\theta})}{s^2 - A_6} \tag{3.5}$$

In particular, by imposing a 6 dB margin at low frequency ($\omega \to 0$) we have

$$K(j\omega)G(j\omega) = \frac{K_1(K_{D_\theta}j\omega + K_{P_\theta})}{-\omega^2 - A_6} = 2 \tag{3.6}$$

so that K_{P_θ} is given by

$$K_{P_\theta} = \frac{2A_6}{K_1} \tag{3.7}$$

The K_{D_θ} is obtained when a 30 deg phase-margin is specified as

$$K(j\omega)G(j\omega) = \frac{K_1(K_{D_\theta}j\omega + K_{P_\theta})}{-\omega^2 - A_6} = \cos(30°) + j\sin(30°) = (-0.86 + 0.5j) \tag{3.8}$$

and therefore

$$\frac{K_1(K_{D_\theta}j\omega + K_{P_\theta})}{-\omega^2 - A_6} = (-0.86 + 0.5j) \tag{3.9}$$

The next step consist in equating the real parts of the right- and left-hand side

of Eq. (3.9) as follows

$$K_1 K_{P_\theta} = -0.866(-\omega^2 - A_6) \tag{3.10}$$

By substituting Eq. (3.7) into Eq. (3.10), ω is obtained as

$$\omega = \sqrt{1.3 A_6} \tag{3.11}$$

Finally, by equating the imaginary part of the right- and left-hand side of Eq. (3.9) and using Eq. (3.11), one obtains

$$K_1 K_{D_\theta} \omega = 0.5(-\omega^2 - A_6) \tag{3.12}$$

$$K_{D_\theta} = \frac{\sqrt{A_6}}{K_1} \tag{3.13}$$

Equations (3.7) and (3.13) are based on parameters A_6 and K_1, allowing to mechanize the synthesis procedure for all the design point throughout the reference trajectory. The Nichols plot of the uncontrolled LV short-period dynamics $G(s)$ and the controlled system $K(s)G(s)$ at $t = 72\,\mathrm{s}$ in Fig. 3.5, shows that the action of $K(s)$ is to move upward and in right side the open-loop response curve of the system $G(s)$ providing the required $6\,\mathrm{dB}$ gain margin and $30\,\mathrm{deg}$ phase margin.
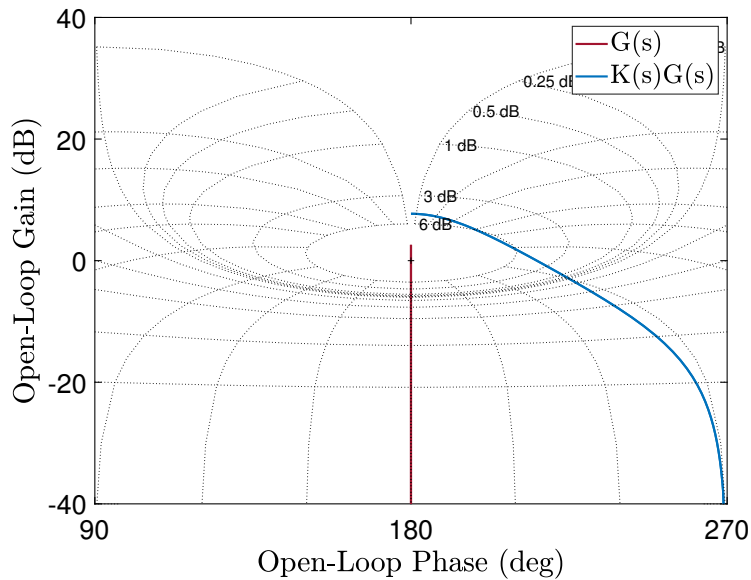
Figure 3.5. Nichols plots of LV short period open loop $G(s)$ (red line) and the controlled $K(s)G(s)$ (blue line) dynamics.

TVC actuator dynamics

At this point, the TVC actuator dynamic (see Sec. 2.6) must be taken into account. Since it maybe in the bandpass of the first bending mode and therefore has significant effects on their stability properties. Being the TVC frequency response a second-order low-pass filter with the additional phase-shift due to computational delay time, its effect is to add a phase-lag and magnitude attenuation at intermediate and high frequencies. The TVC actuator dynamics are often
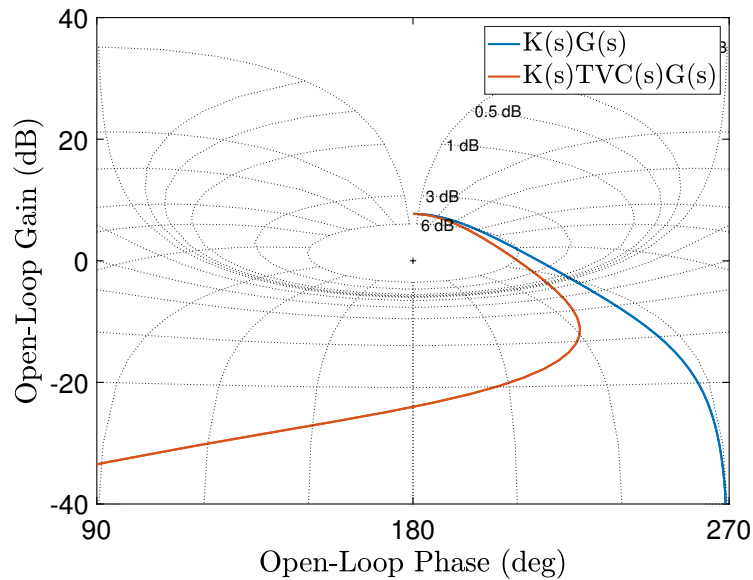
Figure 3.6. Nichols plots of the open-loop responses of controlled short period dynamics $K(s)G(s)$ with (red line) and without (blue line) TVC actuator dynamics.

The Nichols plots of Fig. 3.6 shows the effect of the TVC actuator dynamics on system phase. Note that the Rigid PM decreases with respect to the system without the TVC, while the Aero GM margin is marginally affected.

3.2.2 Bending mode stabilization

Bending mode stabilization is the most distinctive and difficult problem encountered in designing LV attitude control, because the bending mode properties are not known with great precision, and they vary with flight time. In particular, when there is not an adequate separation in frequency between bending and rigid-body modes, it is increasingly more difficult to ensure satisfying rigid-body response and, at the same time, stabilize the elastic dynamics.

The INS sensor measures both angle and rate of the elastic body and, in turn, feeds these signals back into the control loop. This usually causes degradation of the control system stability and may even drive the system to instability.

Since the bending mode is excited by TVC nozzle rotation, the transfer function of rigid body and flexible dynamics is

$$\frac{\theta(s)}{\beta(s)} = G(s) + G_{flex}(s) \tag{3.14}$$

where $G_{flex}(s)$ is obtained from Eq. (2.148)

$$G_{flex}(s) = \frac{-\hat{\phi}_{TVC}T_c}{s^2 + 2\zeta_{BM}\omega_{BM}s + \omega_{BM}^2} \tag{3.15}$$

The Bode plot of the open-loop response of the uncontrolled LV when both rigid and flexible dynamics are considered is shown in Fig. 3.7(a) of different time steps during the flight. Resonant peaks are apparent at high frequency due to the bending mode dynamics, the magnitude and frequency of which increase as flight time increases. Figure 3.7(b) shows that the complex poles associated to the bending mode dynamics move away from the real axis. Therefore, as the flight time increases the bending mode exhibit a faster and more oscillatory behavior. At the same time, the real poles associated to rigid body translate towards faster dynamics and then return towards the real axis exhibiting slower dynamics at the end phase of flight.

(a) Bode plot   (b) System roots location
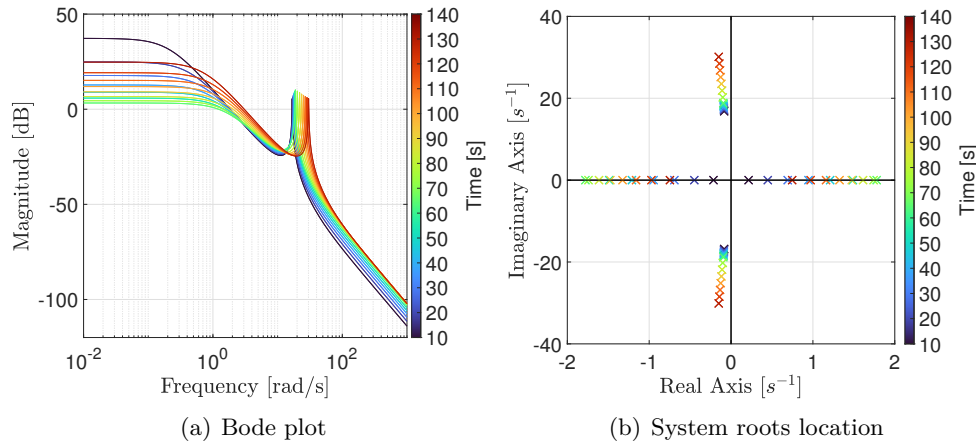
Figure 3.7. LV short-period and bending mode dynamics as functions of time.

Figure 3.8 shows the root locus of the LV system at the maximum dynamic pressure condition, comprehensive of rigid and flexible dynamics and featuring the PD controller on the pitch angle presented in Eq. (3.4). The bending mode dynamics introduces an additional pole-zero pair in the open-loop system. It is apparent in Fig. 3.8 that the PD controller is not able to stabilize the system and, in particular, the poles of bending mode move in the right-half of the complex plane as K_{P_θ} increases. The location of the roots shown in Figure 3.8 is typical of LV having

attitude sensor located on the nose of the vehicle [11].
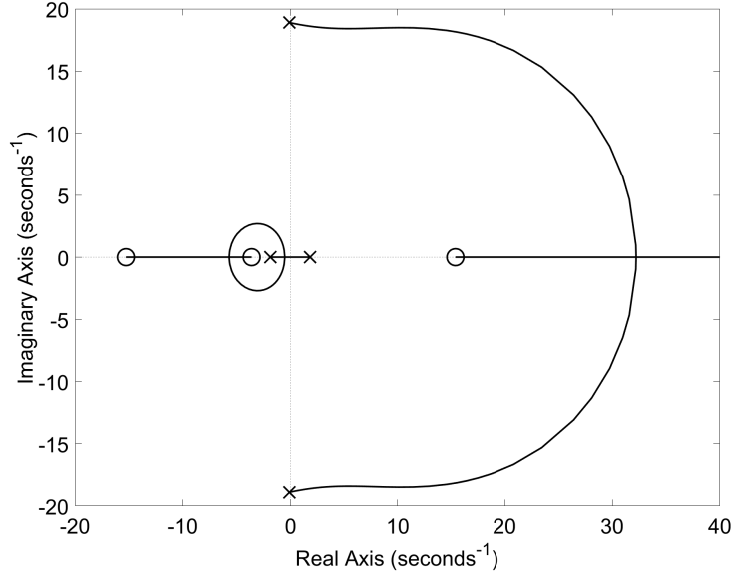
Figure 3.8. Root locus of the controlled LV model, including short-period and bending mode dynamics for positive variations of K_{P_θ}.

Considering the instability due to the first bending mode, some type of compensation is necessary to stabilize the system. To this end, the conventional approach relies on the implementation of second-order structural filters for appropriate gain-phase stabilization of flexible modes, as for instance, low-pass and notch filters. In this study, low-pass and notch filters are designed according to the guidelines provided by Wie [80].

Phase stabilization

Phase stabilization provides the desired gain and phase characteristics at the specified frequency. A phase-stabilized bending mode is one that has a finite phase margin. To this end a non-minimum phase, second-order, low-pass filter

$$H_X(s) = \frac{s^2 - 2\zeta_z\omega_z s + \omega_z^2}{s^2 + 2\zeta_p\omega_p s + \omega_p^2} \tag{3.16}$$

is considered. Pole and zero locations are specified so that they share the same natural frequency ($\omega_z = \omega_p = 1.3\,\omega_{BM}$) with $\zeta_p > \zeta_z$, and the values $\zeta_p = 0.5$ and $\zeta_z = 0.2$ have been selected in order to provide the desired phase shift.

In the present control problem, phase stabilization is realized when the phase of the first bending mode is near $0\,\mathrm{deg}$ (in general between -180 and 180 deg).

The reason is apparent from Fig. 3.9, where the Nichols plot of open-loop response of the rigid-body (blue line) and bending mode dynamics (red line) of the model controlled by PD (Fig. 3.9(a)), and PD and low-pass filter (Fig. 3.9(b)) are shown. The low-pass filter phase-stabilizes the system by shifting the phase of the open-loop

(a) Unstable system   (b) Phase stabilized system
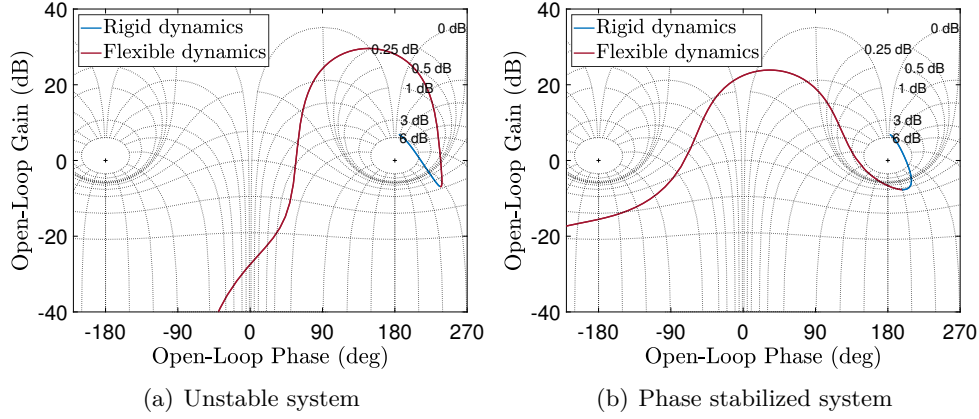
Figure 3.9. Phase stabilization of the LV model at $t = 72\,\text{s}$.

response curve relative to the flexible dynamics to the left of critical point [0dB, 180 deg]. Even though the open-loop response is stable (the critical point is encircled clockwise), Fig. 3.9(b) shows that the bending mode magnitude is too high so that attenuation is required. As consequence, a notch filter is introduced in order to gain-stabilize the bending mode.

Gain stabilization

Notch filtering suppresses unwanted signal in the control loop, ensuring that the specific mode is not to be destabilized by feedback control. Moreover, provides gain stabilization, reducing control loop gain at the desired frequency so as to obtain stability regardless of phase uncertainties. According to [80], the notch filter is realized in the form

$$H_{notch}(s) = \frac{s^2 + 2\zeta_N\omega_N s + \omega_N^2}{s^2 + 2\zeta_D\omega_D s + \omega_D^2} \tag{3.17}$$

for $\omega_N = \omega_D = \omega_{BM}$. The notch filter is designed to have the zeros near the undesirable, light-damped poles of the system, in order to achieve an approximate cancellation, and the poles placed so as to increase the damping of the system. Therefore, the parameters ζ_N and ζ_D, with $\zeta_N < \zeta_D$, specify bandwidth and peak level of filter attenuation. The frequency response is reported in the Bode plot of Fig. 3.10 for different values of the damping ratio ζ_D.

The provided attenuation of the filter is obtained at $\omega_N = \omega_D = \omega_{BM}$ as
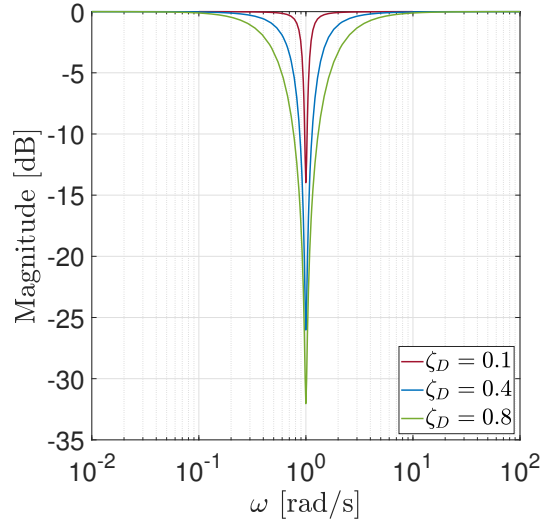
Figure 3.10. Bode plot of a notch filter for different values of ζ_D.

$$K_{notch} = 20 \log_{10} \left(\frac{\zeta_N}{\zeta_D} \right) \tag{3.18}$$

As reported in [77], in order to deal with the uncertainty of the bending mode frequency, the notch filter is realized by three cascaded second-order filters centered, respectively, at the nominal bending mode frequency ω_{BM}, and at the minimum and maximum expected dispersed frequencies of the bending mode due to modelling uncertainties ($\underline{\omega}_{BM}$ and $\overline{\omega}_{BM}$). The overall transfer function is

$$H_N(s) = \frac{s^2 + 2\zeta_N \underline{\omega}_{BM}s + \underline{\omega}_{BM}^2}{s^2 + 2\zeta_D \underline{\omega}_{BM}s + \underline{\omega}_{BM}^2} \cdot \frac{s^2 + 2\zeta_N \omega_{BM}s + \omega_{BM}^2}{s^2 + 2\zeta_D \omega_{BM}s + \omega_{BM}^2} \cdot \frac{s^2 + 2\zeta_N \overline{\omega}_{BM}s + \overline{\omega}_{BM}^2}{s^2 + 2\zeta_D \overline{\omega}_{BM}s + \overline{\omega}_{BM}^2}$$

$$\tag{3.19}$$

where ω_{BM} is the (nominal) bending mode frequency and, considering an uncertainty of $\omega_{BM} \pm 10\%$, it is $\underline{\omega}_{BM} = 0.9\,\omega_{BM}$ and $\overline{\omega}_{BM} = 1.1\,\omega_{BM}$, and we set $\zeta_N = 0.02$ and $\zeta_D = 0.1$. The frequency response of $H_N(s)$ is shown in Fig. 3.11. In conclusion, using of cascaded notch filters provides bending mode peak attenuation into a specific bandwidth defined to accommodate the frequency uncertainty (Fig. 3.11(a)). Moreover, as shown in Fig 3.11(b), it also provides additional phase stabilization, that increases the Flex-PM relative to the banding mode.

Finally, bending mode stabilization is achieved by the series connection of low-pass filter and notch filter, as follows

$$H_F(s) = H_x(s)H_N(s) \tag{3.20}$$

(a) Magnitude (b) Phase
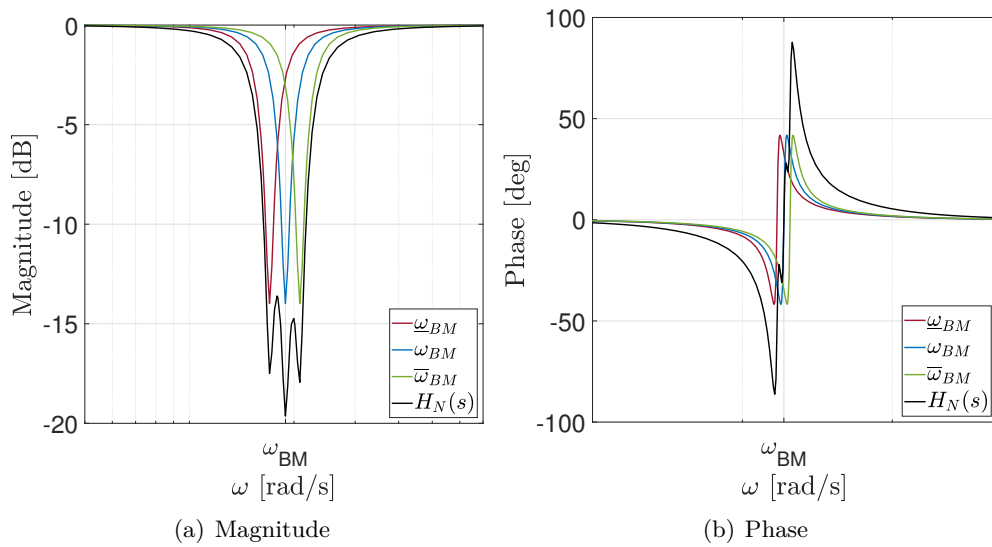
Figure 3.11. Bode plot of a the cascaded notch filters $H_N(s)$.

The bending filter $H_F(s)$ acts on the output of the PD controller eliminating the frequency content in the signal that may excite the bending mode. Finally, the resulting Nichols plot of the controlled system with the bending mode filter $H_F(s)$ is shown in Fig 3.12, where the attenuation of the flexible dynamics with respect to the system featuring the low-pass filter (Fig 3.9(b)) only is clearly visible.
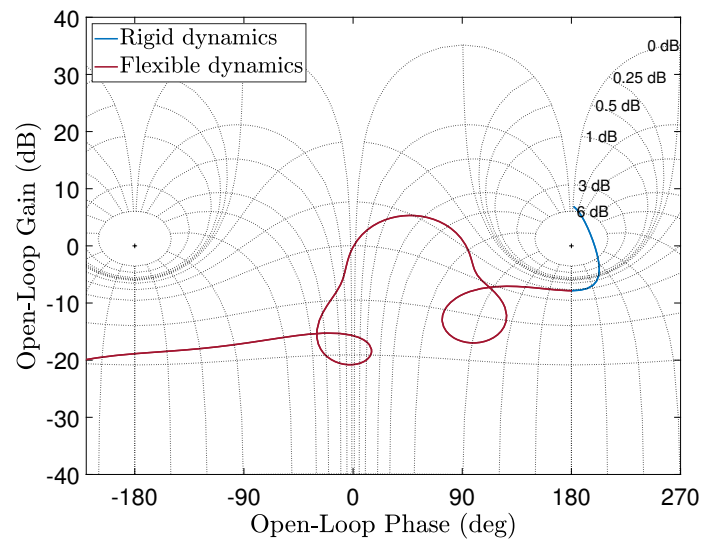
Figure 3.12. Nichols plots of the LV dynamics, including rigid (blue line), flexible (red line) and TVC actuator dynamics, featuring the bending mode filters $H_F(s)$.

3.2.3 Drift control

The PD controller discussed above, is able to meet the stability requirements illustrated in Table 3.1. However, the FCS is also required to meet the performance specification reported in Table 3.2. In particular, the FCS should limit aerodynamic load, lateral drift and drift rate, that are primary due to the wind disturbances. The reduction of the aerodynamic load for LV is achieved by minimizing the angle of attack, the aerodynamic load $Q\alpha$ being expressed as,

$$Q\alpha = Q(\theta + \frac{\dot{z}}{V} - \alpha_w) \tag{3.21}$$

It is apparent that, the so-called load minimum condition [81], that is, angle of attack variations are minimized, can be obtained by using a θ feedback controller. According to [11], since the fundamental time constant of the lateral drift dynamics is much greater than that associated to the attitude dynamics, an appropriate selection of K_θ may be obtained by analyzing the so called quasi steady-state form of the rigid body equation wherein the first and high order derivatives in θ are set equal to zero. Therefore, considering the rigid-body attitude dynamics (Eq. (2.146)) and using Eq. (2.153), one has

$$\ddot{\theta} = A_6\alpha + K_1\beta \tag{3.22}$$

By substituting the PD control law for $\beta(s)$

$$\beta(s) = -(K_{P_\theta} + K_{D_\theta}s)\theta(s) \tag{3.23}$$

the following transfer function for θ results

$$\theta(s) = \frac{A_6}{s^2 + K_1 K_{D_\theta}s + (K_1 K_{P_\theta} - A_6)}\left(\frac{\dot{z}_{ss}}{V} - \alpha_w\right) \tag{3.24}$$

where $\dot{z}_{ss}$ is the drift rate value at steady-state. Finally, setting the first and second derivative of θ to zero gives

$$\theta_{ss} = \frac{A_6}{(K_1 K_{P_\theta} - A_6)}\left(\frac{\dot{z}_{ss}}{V} - \alpha_w\right) \tag{3.25}$$

By substituting Eq. (3.25) in Eq. (2.149) the steady-state value of α is obtained

$$\alpha_{ss} = \frac{K_1 K_{P_\theta}}{(K_1 K_{P_\theta} - A_6)}\left(\frac{\dot{z}_{ss}}{V} - \alpha_w\right) \tag{3.26}$$

It is apparent that the load minimum condition ($\alpha_{ss} = 0$) is achieved for $K_{P_\theta} = 0$.

This solution is not feasible because the system becomes unstable. In this respect, to accomplish the tasks of limiting the aerodynamic load and the lateral drift with respect to the reference trajectory, an additional feedback on drift z and drift rate $\dot{z}$ is introduced, so as to obtain the control low already presented (Eq. (3.1)), that is here recalled for the sake of clarity,

$$\boldsymbol{K}_{BC}(s) = [K_{P_\theta} \quad K_{D_\theta} \quad K_{P_z} \quad K_{D_z}]H_X(s)H_N(s)$$

where, as said, K_{P_z} and K_{D_z} are the control gain for the feedback on z and $\dot{z}$, respectively.

It is worth to recall that, even thought the proportional control on θ has an effect on the angle of attack, it is difficult to select a K_{P_θ} value able to satisfy the stability requirements as well as to limit the variation of the angle of attack and, consequently, the aerodynamic load. Therefore, using Eqs. (3.7) and Eqs. (3.13), only minor adjustments of K_{P_θ} and K_{D_θ} obtained are required in order to obtain adequate robustness with respect to lateral dynamics, that are neglected in the selection procedure of K_{P_θ} and K_{D_θ} discussed in Sec. 3.2.1. Moreover, small values for K_{P_z} and K_{D_z} provide a satisfying way for reducing lateral drift and aerodynamic loads without degrading the attitude tracking performance. Note also that using large values of K_{P_z} and K_{D_z} leads the system to instability.
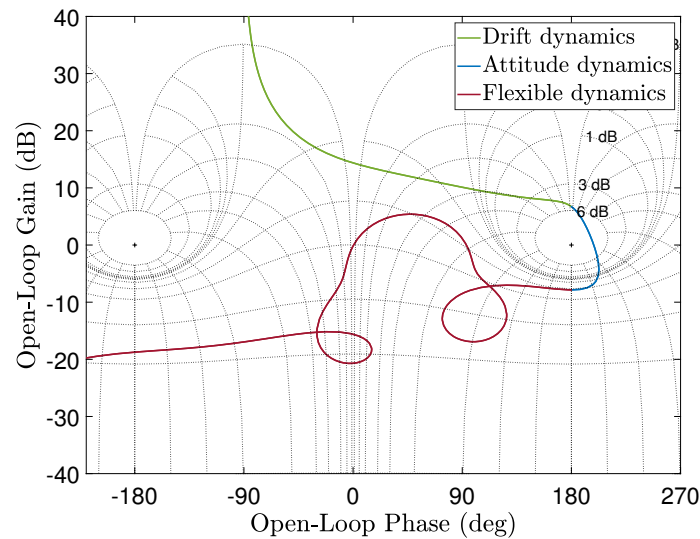
Figure 3.13. Nichols plot of the LV model at $t = 72\,\text{s}$, including rigid and flexible body and TVC actuator dynamics, controlled by the BC.

The Nichols plot of the system featuring the controller of Eq. (3.1) is shown in Fig. 3.13, where three sections of the open-loop response curve are visible, that is, the low-frequency section relative to the lateral drift controlled dynamics (green

line), the attitude dynamics (blue line), and the high-frequency dynamics relative to the bending mode stabilized using the filter $H_F(s)$ (red line).

3.2.4 Gain scheduling

As discussed in Section 2.5, most of the LV parameters are dependent on time; mass and inertial properties, aerodynamics coefficients, bending mode frequency and thrust vary rapidly during the flight.

A suitable strategy to manage the parameter variations and guarantee the appropriate stability margin and performance during the atmospheric phase, is the Gain Scheduling (GS) of the control law [20, 18]. GS approach consists in decomposing the LV control problem into a number of linear designs performed along the flight envelope at a number of operational points so as to obtain a scheduled global controller by interpolating design points. In this study, the PD control gains are synthesized with a time step of 10 s along the trajectory, and linearly interpolated as functions of flight time (Fig. 3.14).

The main drawback of the GS methodology is that the stability and performance robustness are not guaranteed between the design points [18]. This problem is generally overcome by analyzing the linear stability of the system using a finer grid of analysis points and also by an extensive time-domain simulation analysis.
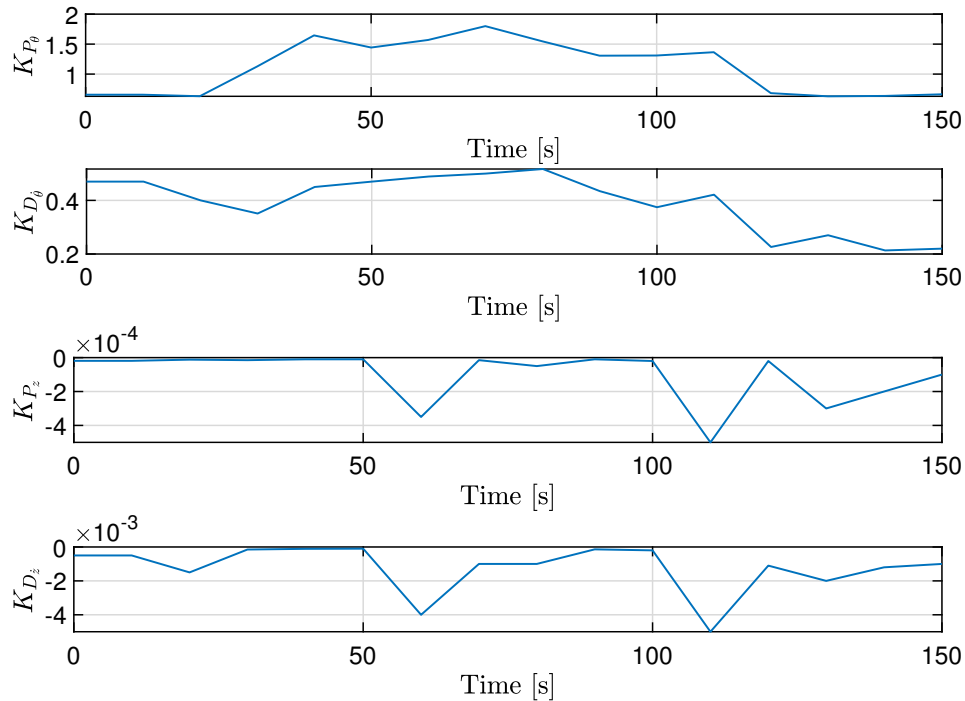
Figure 3.14. PD controller gains versus time.

3.3 Results

In this section, the BC stability and performance are assessed via classical linear stability analysis and time-domain simulations. The simulations are carried out using the linear time-varying model presented in Sec. 2.8, from launch through an altitude of $60\,\mathrm{km}$ ($t = 140\,\mathrm{s}$) in situations where the LV undergoes the Dryden wind disturbances discussed in Sec. 2.7. The analysis is conducted both in nominal condition, and taking into account the effects of parameter uncertainties.

3.3.1 Performance in nominal conditions

In nominal conditions system stability requires to have all the closed-loop poles on the left side of the complex plane, which can be easily assessed in the frequency domain through Nichols plot. In this respect, the Nichols plots of open-loop responses at time steps of $10\,\mathrm{s}$ from $t = 10$ to $140\,\mathrm{s}$ in Fig. 3.15, show that the LV featuring the BC developed in this chapter, is stable throughout the flight.
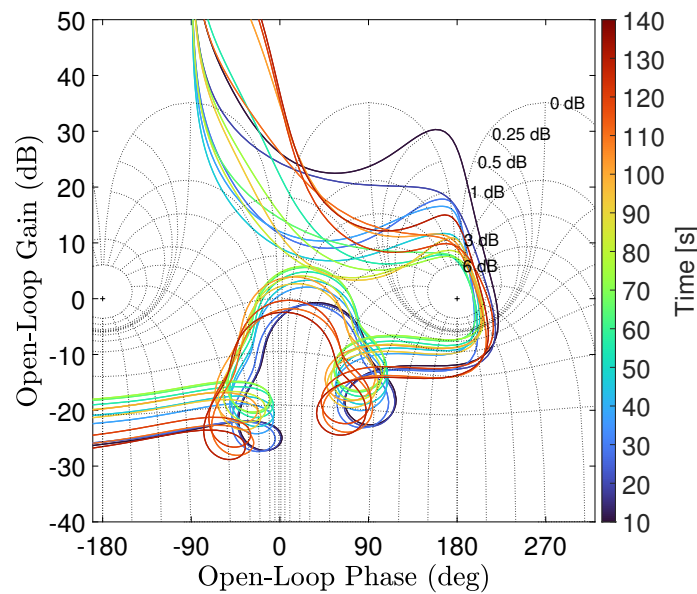
Figure 3.15. Nichols plots at design points.

The levels of stability are analyzed through classical metrics, such as gain and phase margins at different crossing frequencies, as outlined in Sec. 3.2. The margins evaluated in the time range from $10\,\mathrm{s}$ to $140\,\mathrm{s}$ are shown in Fig. 3.16 together with the design requirements (red lines) of Table 3.1. Figure 3.16(a) shows that the rigid-body gain margin (Aero GM and Rigid GM) meet the robustness requirement reported in Table 3.1, although with narrower stability margins when aerodynamic loads become more intense. BC is able to meet the specification on the rigid phase
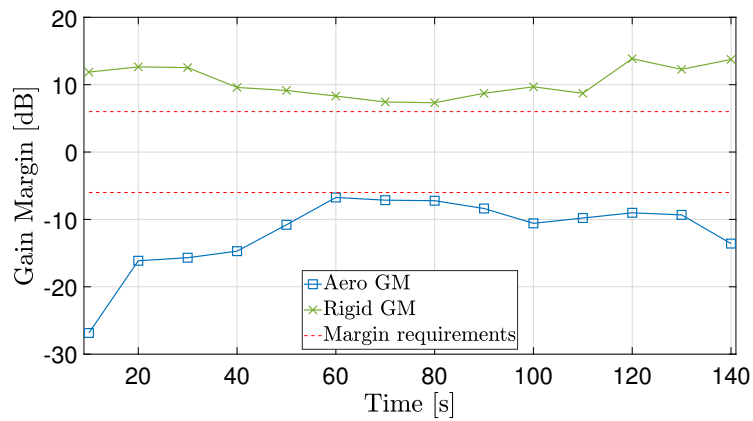
(a) Rigid-body gain margins
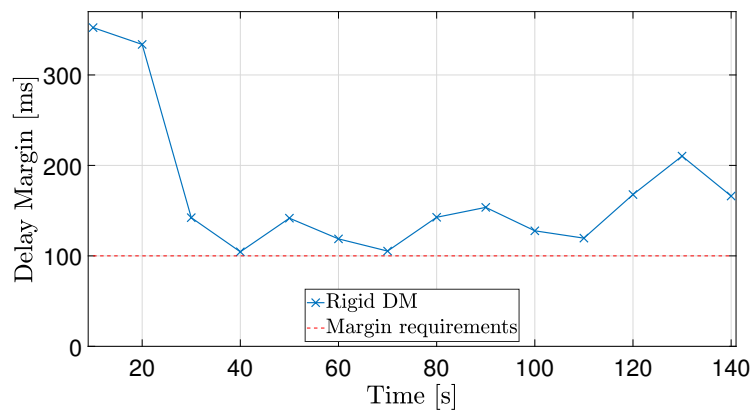
(b) Rigid-body delay margins
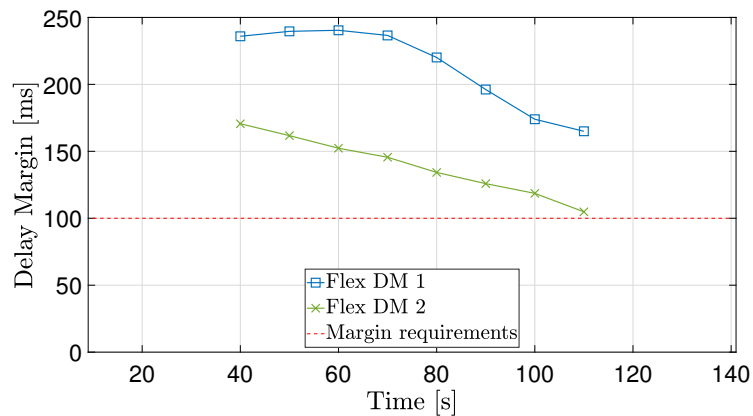
(c) Flexible-body delay margins

Figure 3.16. Classical stability margins as functions of flight time.

margin, as shown in Fig 3.16(b), reported in terms of delay margin to match the requirement formulation (Table 3.1). Moreover, flexible-body dynamics is effectively stabilized by BC and the robustness requirements are met as it is apparent from Fig 3.16(c). The delay margins relative to the flexible dynamics not reported are

equal to ∞.

3.3.2   Performance in off-nominal conditions

In LV FCS design the analysis of the effect of parameter uncertainties on BC stability and performance is of great interest. In fact, LV model is inherently uncertain and parametric uncertainty may determine significant variations in the behavior of the model.

Each uncertain parameter p is represented using a multiplicative model as follows

$$p = p_{NOM}(1 + p_r\Delta) \qquad \Delta \in [-1, 1] \tag{3.27}$$

where p_{NOM} is the nominal value and p_r is the uncertainty range.

As said above, parameter uncertainties may have a significant effect on the stability of the controlled system, that is assessed using classical indicators (e.g. gain and phase stability margin) and tools such as Nichols plots. In this respect, in what follows an analysis is conducted by varying only some parameters that have a major impact on the system behavior, that is, the so-called aerodynamic parameter A_6, the controllability parameter K_1, and the first bending-mode frequency ω_{BM}.
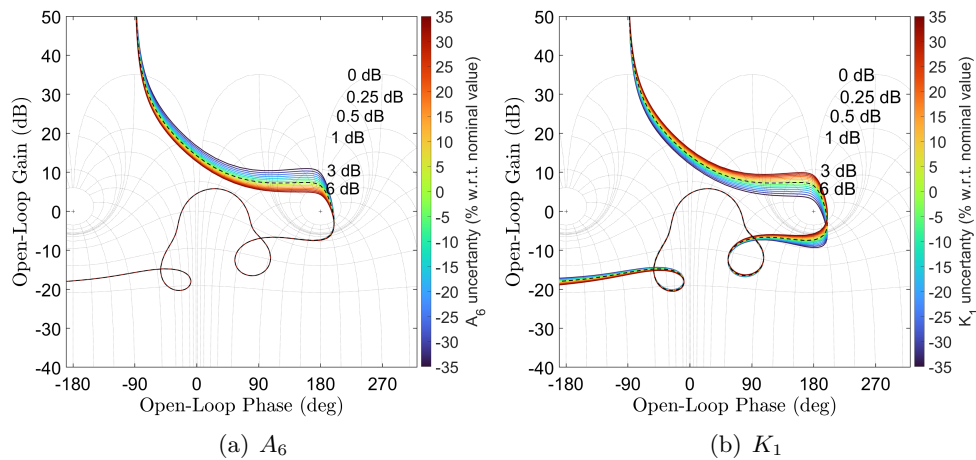
Figure 3.17. Nichols plots of the open-loop response for perturbed values A_6 and K_1 at $t = 72\,\mathrm{s}$.

Figure 3.17 shows the of Nichols plots of the open-loop linear model at $t = 72\,\mathrm{s}$ (high dynamic pressure region) for A_6 and K_1 uncertainties in the range $\pm 35\%$. It is apparent in Fig. 3.17(a), that the increase on A_6 determines a reduction of stability as Nichols plot shifts in the direction of the stability point and the Aero GM is reduced. Conversely, Fig. 3.17(b) shows that the Aero GM is degraded as K_1 decreases. Therefore, variations on A_6 and K_1 have opposite effects on the stability

at low-frequency. Nevertheless, this is an expected result as, in fact, the ratio A_6/K_1 is a critical factor for LV control, because the first requirement of attitude control is that there exist sufficient control capability to limit aerodynamic loads, that is, $K_1\beta > A_6\alpha$. Consequently, as the ratio A_6/K_1 increases, control capability of the TVC is reduced, and the allowable TVC nozzle deflection must be greater to balance the aerodynamic moment.
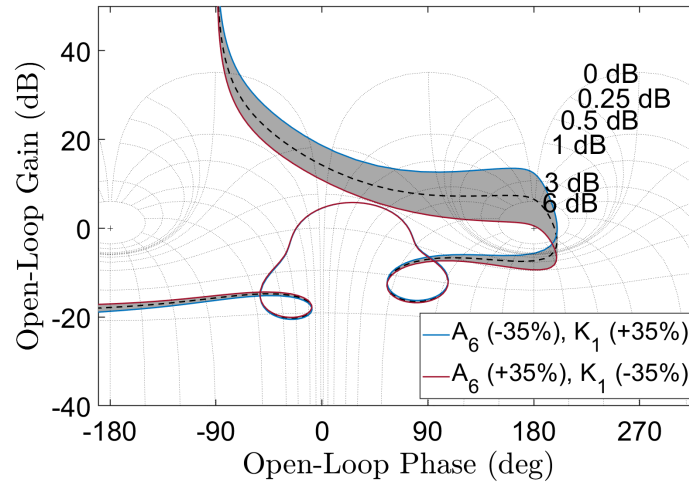
Figure 3.18. Effects on stability of combined variations of A_6 and K_1.

In this respect, the worst case for the rigid body stability is identified when K_1 is reduced and A_6 is increased as shown in Fig. 3.18, where the Nichols plots obtained for different combination of A_6 and K_1 uncertainties in the range $\pm35\%$ are traced in gray. The red line represents the frequency response for variations of $+35\%$ on A_6 and -35% on K_1, that drive the system in a condition where the Aero GM is approximately zero.

Figure 3.18 also shows the Nichols plot obtained for scattering of -35% on A_6 and $+35\%$ of K_1, in this case, a relevant increment of the Aero GM together with a small reduction of the Rigid GM with respect to the nominal case is visible.

The performance degradation of the BC occurring when an increase on A_6 and reduction of K_1 is taken into account, is confirmed by the result of time domain simulation shown in Fig. 3.19. In particular, Fig. 3.19 reports the comparison between the model response, in terms of aerodynamic loads $Q\alpha$, for different level of uncertainty obtained increasing A_6 and reducing K_1 by the same percentage respect to their nominal values, the maximum variation being $\pm40\%$. It is apparent that the maximum amplitude of $Q\alpha$ rapidly increases with the level of uncertainty, and, for a $+10\%$ of A_6 and -10% of K_1, the aerodynamic load reaches its $Q\alpha$ safety envelope, whereas for greater scattering $Q\alpha$ requirement is violated. Eventually, for
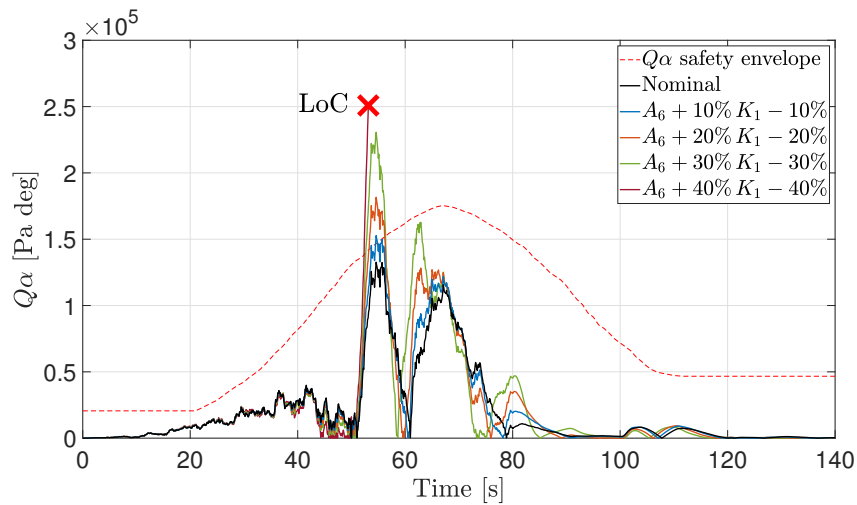
Figure 3.19. $Q\alpha$ time histories for combined variations of A_6 and K_1.

a scattering level of 40% the BC is not longer able to control the LV in the presence of severe Dryden gust, and a loss of control (LoC) occurs, that is, the control cannot be recovered. Further insight on the effect of the increasing level of uncertainty on BC performance is provided from the time history of the pitch angle (Fig. 3.20(a)), lateral drift (Fig. 3.20(b)) and lateral drift rate (Fig. 3.20(c)), where, similar to $Q\alpha$ behavior, the maximum amplitude of these variables increase for greater level of scattering.

The other parameter that has a major impact on the system behavior is the bending mode natural frequency ω_{BM}. The effects of its variations are shown in the Nichols plots of Fig. 3.21 for scattering in the range between -35% and +35%. As the dispersion increases for both positive and negative variations, Fig. 3.21 shows that the "hump" in the range [180 deg, -180 deg], relative to the bending mode, rapidly grows because the notch-filter, centered on the nominal value of ω_{BM}, is not able to effectively attenuate the bending mode. In particular, negative variation of ω_{BM} leads to a considerable reduction of Rigid GM as well as Flex PM.

The reduction of the Rigid GM due to a negative variation of ω_{BM} is apparent in Fig 3.22, where the Rigid GM at different flight times are reported for a reduction of the bending mode frequency up tp 50%. In particular, the figure shows that the reduction of Rigid GM is not uniform as the bending mode decreases. In fact, for variation up to 20% the margin degradation in limited, whereas it decreases rapidly for uncertainties larger than 20%. Indeed, the notch filter (see Sec. 3.2.2), is designed to accommodate a 10% uncertainty of the bending mode natural frequency, and its effectiveness in attenuating bending mode dynamics is increasingly reduced as ω_{BM} becomes higher than 10%.
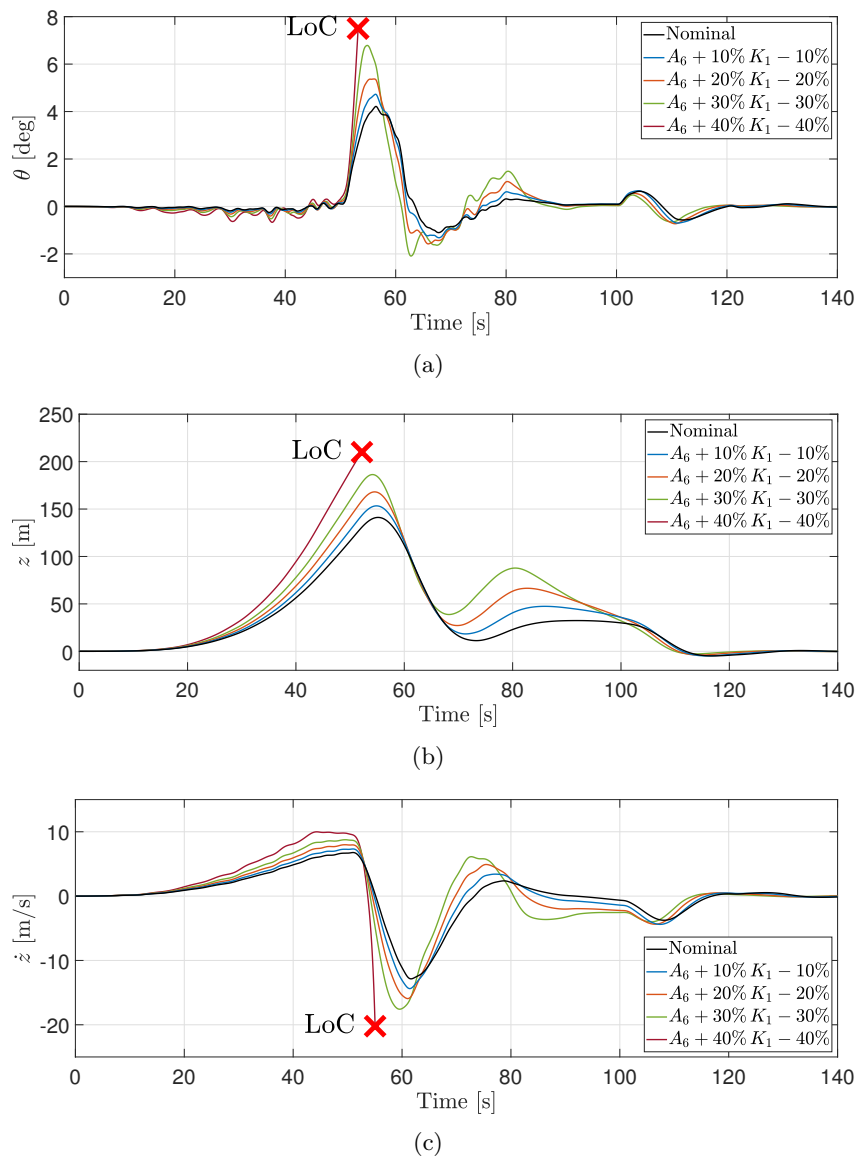
Figure 3.20. Simulation results for different combined uncertainty variations of A_6 and K_1.

Figure 3.23 shows the simulation results in terms of pitch angle responses when the bending mode frequency is reduced up tp 50%.

It is apparent that the BC effectively manages up to -20% of uncertainty on the ω_{BM}, and the responses are similar to those resulting in nominal conditions. Conversely, for a ω_{BM} reduction of -40%, pitch angle oscillations appear between t = 60-100 s, and the BC is not longer able to control the LV for a variation of -50%. These results are confirmed when the Rigid GM is analyzed in Fig 3.22; for a 40% reduction of ω_{BM} the Rigid GM assumes small values and is negative between t =
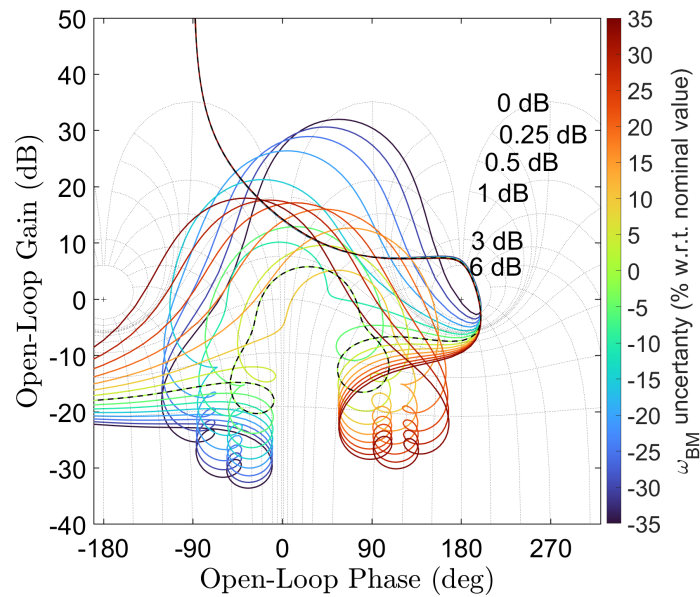
Figure 3.21. Nichols plots for scattering of ω_{BM}.
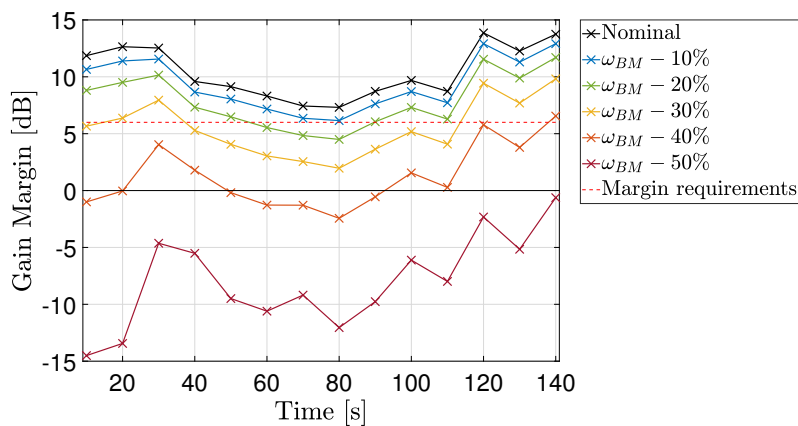
Figure 3.22. Rigid GM for scattering of ω_{BM}.

$50 - 90$ s, that indicates that the system is unstable, whereas the -50% variation of the frequency drives the system unstable throughout the flight, as the Rigid GM is negative for all the design points.

It is also worth to mention that, although the Rigid GM in Fig 3.22 shows that the LV model is unstable in the time range 50-90 s for a reduction of the bending mode frequency of 40%, no divergence occurs in the time-domain simulation (Fig. 3.23). Further analyses carried out by removing saturation on TVC angular and angle rate show that the observed behavior is related to these nonlinear components. In particular, it appears that saturations on angular and angular rate limit the amplitude of the high frequency oscillations of thrust axis that develop in the model without saturation (Fig. 3.24), as the high-frequency oscillations excite the bending
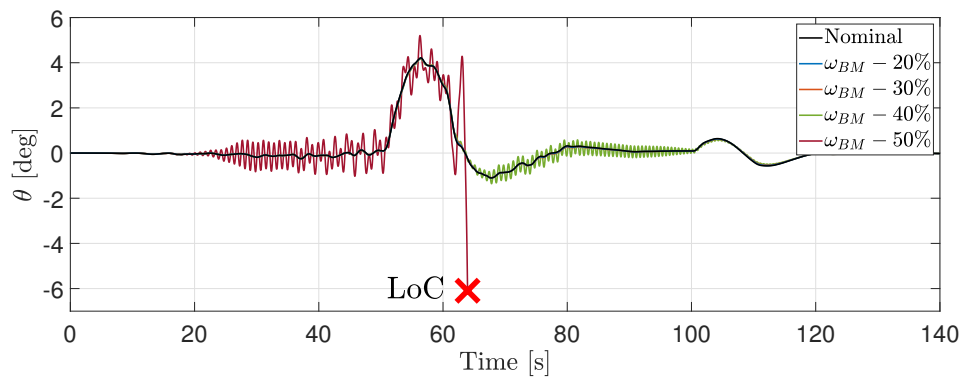
Figure 3.23. Pitch angle response for different scattering levels of ω_{BM}.
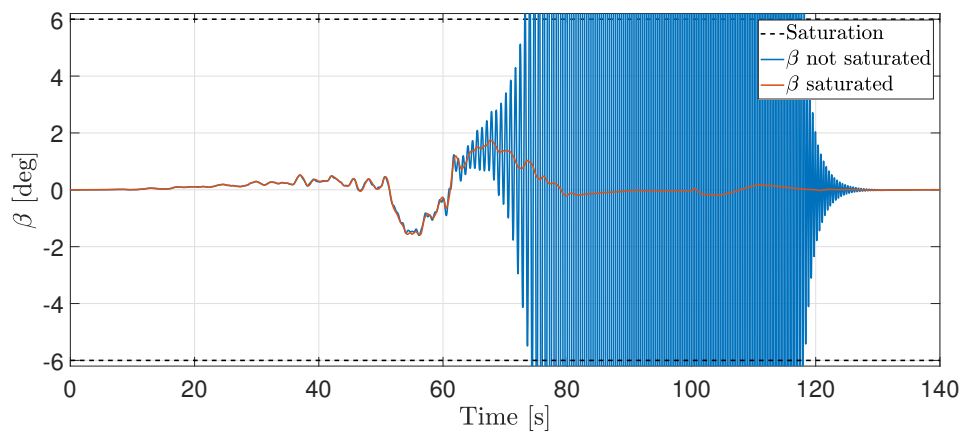
Figure 3.24. TVC nozzle rotation response with (red line) and without (blue line) angle and angle rate saturations.

mode and driving the model unstable.

Chapter 4

Adaptive augmenting control

4.1 Introduction

An adaptive controller is a control system with a mechanism for adjusting the parameters in order to achieve a certain desired behavior in response to the system variation and/or disturbances [41]: In other words, it has the ability to modify control gains depending on input to the plant in order to accommodate system uncertainty [40]. The adjustable parameters are called adaptive and the adjusting mechanism, which is described by a set of mathematical equations, is called an adaptive law. In most cases, this kind of controller is nonlinear because of the adaptive law, making adaptive control inherently difficult to design and analyze by using traditional design and analysis methods for linear time-invariant (LTI) control systems, such as Bode plot, Nichols plot, phase and gain margins and eigenvalue analysis [39].

The model reference adaptive system (MRAS) is, probably, one of the adaptive methods most frequently used. The adaptive gains are adjusted according to the error signal given by the difference between system output and output of a reference model expressing the desired performance of the closed-loop control system [39, 82]. The mechanism for adjusting the parameters in MRAS is usually realized by using two well-know approaches, that is, the gradient descent method, know as the MIT rule, and the Lyapunov stability theory [83]. Beside the above mentioned techniques, many other adaptive controllers have been successfully developed and deployed for research applications. On the other hand an adaptive control system has never been implemented on any safety-critical systems, the main problem being the difficulty in the verification and validation of the controller, since existing certification methods control systems cannot be readily used for nonlinear adaptive control systems [40].

In order to realize the potential benefits of adaptive control and address the flight

certification for a safety-critical aerospace system, Adaptive Augmenting Control (AAC) [51, 52, 54] has been proposed and developed in the framework of the Space Launch System (SLS) program [53]. This approach provides an adaptation layer on top of a classically designed linear control system. In this architecture it is assumed that, in nominal condition, a well-designed linear controller is able to provide the required stability and performance, and the AAC gives little or no augmentation. Conversely, in the event that the BC is unable to provide expected performance due to parameter variation, external disturbances, or large modeling error, the adaptive controller modifies the output of the BC so as to recover adequate performance.

In other words, AAC acts only when the BC loses effectiveness, and has been proposed as a mean to retain the consolidated performance and certification practices of classically designed linear control systems, while consistently expanded the flight envelope improving their performance and robustness in off-nominal conditions [51]. In facts, BC is augmented by an adaptive control law that has the following main objectives: i) to provide minimal adaptation in nominal conditions, ii) to increase performance and command tracking in dispersed conditions and in presence of external disturbances, iii) to prevent loss of vehicle (LoV) in extreme off-nominal conditions [84]. From another point of view, the AAC contribute in improving BC robustness, that is the ability of the system to be insensitive to parameter variations, could make the scheduling and BC implementation simpler reducing the burden of re-tuning activities that are needed for variations of payload mass or mission profile.

4.2 AAC Architecture

In this section the architecture and main features of the AAC system proposed by Orr [51], are recalled, together with, the more modern version of AAC [54] realized in the framework of continuing development of the adaptive gain algorithm for SLS program. In what follows, the original formulation, called AAC first law [51], is first discussed and, then, the modified formulation, dubbed AAC second law [54], is presented.

4.2.1 AAC first law

Adaptive control augments a classical control system (such as, but not necessarily, a PID) with a multiplicative gain that is tuned online, during the flight, in order to minimize deviations with respect to a reference model. In the block diagram shown in Figure 4.1, the output of the adaptive control law is the total adaptive gain k_T, that, multiplied by the output of the BC, regulates the control action β_c. In

BASELINE CONTROLLER

ADAPTIVE AUGMENTING CONTROL
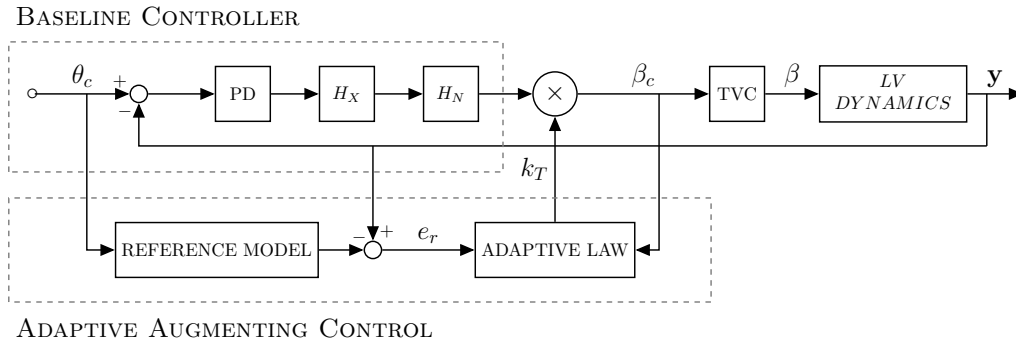
Figure 4.1. Architecture of a LV attitude control system with AAC.

nominal conditions, the BC is expected to manage all control tasks without requiring the intervention of the AAC; conversely, in off-nominal conditions or in presence of significant external disturbances, the AAC should provide an additional robustness layer.

The total adaptive gain k_T is obtained by summing a positive constant gain k_0, that represents the lower bound of k_T, to the output k_a of the adaptive control law, as follows

$$k_T = k_0 + k_a \tag{4.1}$$

In nominal conditions, AAC action should be minimal, so that k_T is as close as possible to unity. The total adaptive gain is only allowed to vary in a limited range of values: upper and lower bounds are set according to stability requirements on gain margins of the system controlled by BC, that are, according to Table 3.1, Aero GM and Rigid GM greater than or equal to 6 dB.

Note also that the total adaptive gain changes the overall gain of the BC, increasing or decreasing the system gain margins, as it is apparent from the Nichols plot in Fig. 4.2 for k_T minor of unity. In facts, the open-loop curve of the systems (LV featuring BC) moves downwards with adaptive control due to the decreased gain. If the adaptive gain is smaller than the system gain margin, the curve passes on the left of the critical point [0 dB, 180 degrees], indicating that the system is unstable. Therefore, if an open-loop gain margin of 6 dB is required and the lower bound for k_T is $k_{T_{min}} = k_0 = 0.5$, then the maximum value that k_a can assume is 1.5, that is, an upper limit for $k_{T_{max}} = 2$, with a gain margin increment of exactly 6 dB, as a larger value of k_T would make the system unstable.

The adaptive control law, that regulates the adaptive gain k_a, is a first order,
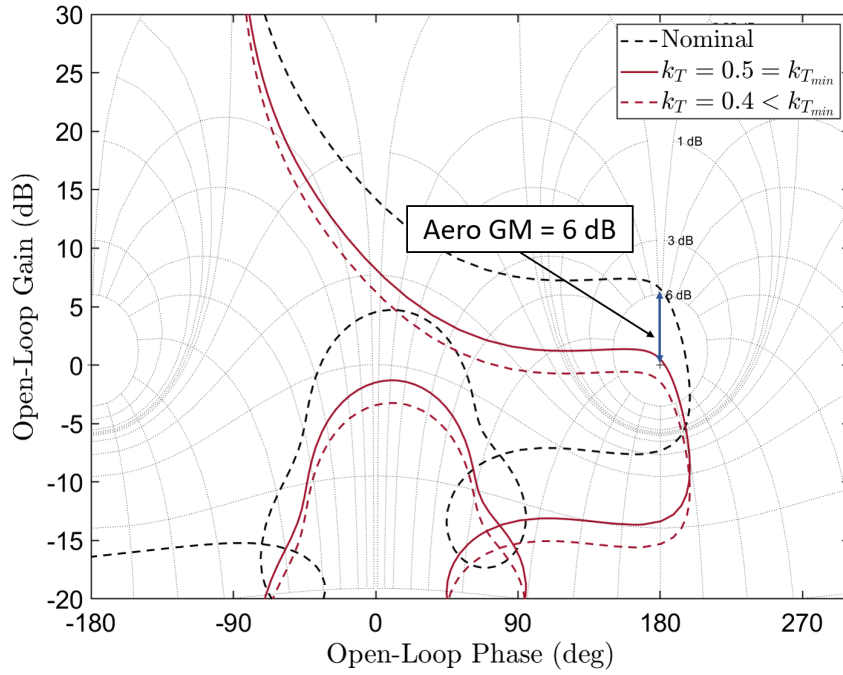
Figure 4.2. Effect of adaptive total gain on the open-loop response curve of the LV featuring BC.

nonlinear, differential equation

$$\dot{k}_a = \left(\frac{k_{a_{max}} - k_a}{k_{a_{max}}} \right) a_{AAC} e_r^2 - \alpha_{AAC} k_a y_s - \beta_{AAC} \left(k_T - 1 \right) \qquad (4.2)$$

where

1. the first component depends on the error e_r between the output of the reference model and the system output, with a saturation term for k_a

2. the second term, called spectral damper, reacts to undesired high-frequency dynamics in the control signal by reducing the adaptive gain

3. the third term acts to bring the system back to the nominal condition, i.e., pushing k_T to unity.

Reference model error and logistic gain limiting

The first term of the adaptive control law in Eq. (4.2)

$$\left(\frac{k_{a_{max}} - k_a}{k_{a_{max}}} \right) a_{AAC} e_r^2 \qquad (4.3)$$

provides adaptation by increasing the adaptive gain proportionally to the square error of a reference model that approximates the closed-loop dynamics of the vehicle [54], expressed as $e_r = \theta_{INS} - \theta_r$. The reference attitude angle θ_r is usually computed according to a second-order linear reference model

$$\frac{\theta_r}{\theta_c} = \frac{2\zeta_r\omega_r s + \omega_r{}^2}{s^2 + 2\zeta_r\omega_r s + \omega_r{}^2} \tag{4.4}$$

The reference model parameters, ω_r and ζ_r, are set so that the response is as similar as possible to the response of the system closed by the BC. Since in the simulation model used in this study the reference frame is tangent to the nominal trajectory, the angle θ_{INS} above represents the angular displacement relative to the nominal condition, and θ_r is zero for the entire flight.

The saturation term $(k_{a_{max}} - k_a)/k_{a_{max}}$, called logistic gain limiting, prevents the adaptive gain from making the system unstable. Furthermore, the logistic gain limiting smoothly brings k_a to its upper limit $k_{a_{max}}$, reducing the adaptive rate.

Spectral damper

The second term in Eq. (4.2), namely, the spectral damper

$$\alpha_{AAC} k_a y_s \tag{4.5}$$

realizes a negative adaptation rate to eliminate frequency components in the control signal that might excite TVC actuators and bending mode dynamics. The spectral damper takes the command β_c as input and generates an output signal y_s proportional to the average power in a specific spectral band. In particular, the nozzle actuator command β_c passes through two filters

$$y_{HP} = H_{HP}(s)\,\beta_c \tag{4.6}$$

$$y_s = H_{LP}(s)\,y_{HP}^2 \tag{4.7}$$

where H_{LP} and H_{HP} are second-order filters that identify the high-frequency content of β_c and quantify the average spectral power of the input, respectively, given by

$$H_{HP} = \frac{s^2 + 2\omega_z^{HP}\,s + \omega_z^2}{s^2 + 2\omega_p^{HP}s + \omega_p^2} \qquad H_{LP} = K^{LP}\frac{s^2 + 2\omega_z^{LP}s + \omega_z^2}{s^2 + 2\omega_p^{LP}s + \omega_p^2} \tag{4.8}$$
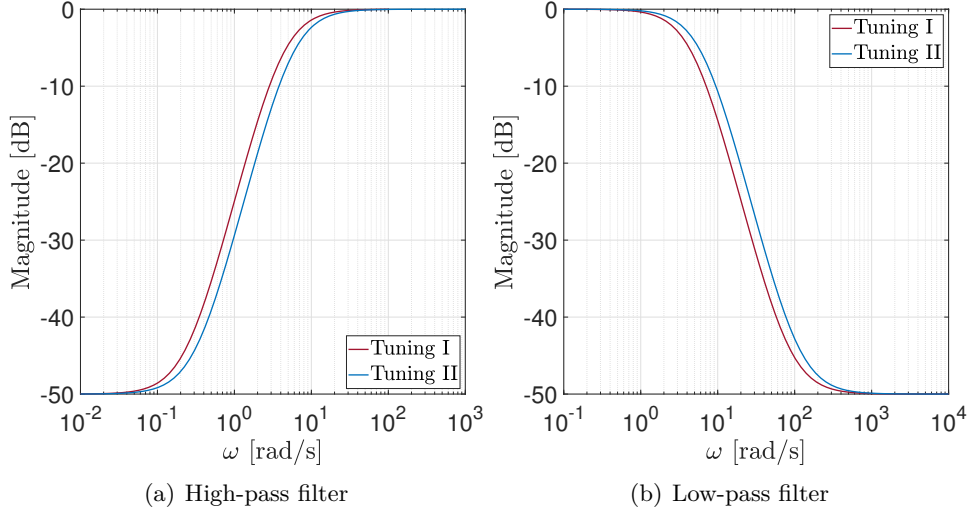
where $K^{LP} = 0.0032$, in order to achieve an attenuation of $50\,\mathrm{dB}$ at high frequency, and the other parameters are expressed in terms of the cut-off frequencies ω_c^{HP} and

ω_c^{LP} as [38, 85]

$$\omega_p^{\text{HP}} = 0.7\omega_c^{\text{HP}} \quad \omega_z^{\text{HP}} = 10^{-5/4}\omega_p^{\text{HP}} \quad \omega_p^{\text{LP}} = 1.6\omega_c^{\text{LP}} \quad \omega_z^{\text{LP}} = 10^{5/4}\omega_p^{\text{LP}}$$

The Bode plots of H_{LP} and H_{HP} are shown in Figure 4.3.

(a) High-pass filter

(b) Low-pass filter

Figure 4.3. Bode plots of spectral damper filters.

In order to generate the spectral damper output y_s, the high-pass filter $H_{HP}(s)$ selects the undesired high-frequency content of β_c, the signal y_{HP} being squared for rectification, and then the low-pass filter $H_{LP}(s)$ provides a measure of the average spectral power of the input. The signal y_s is then multiplied by α_{AAC} and k_a in order to limit the adaptive gain and keep the system within the stability limits.

Spectral damper preliminary tests. Some of the characteristics of the spectral damper, using the transfer functions reported in Eqs. (4.8) (Figure 4.3), are evaluated through two simple simulation tests. In the first one, the spectral damper receives as input the signal β composed of the sum of two sine waves, with frequencies $1\,\text{rad/s}$ and $10\,\text{rad/s}$. As said, the spectral damper acts to eliminate undesired high frequency content in the command signal, thus, the ω_c^{HP} is set to $5\,\text{rad/s}$ and, consequently, $\omega_c^{LP} = \omega_c^{HP}/2 = 2.5\,\text{rad/s}$ according to the guidelines proposed in Sec. 4.2.1. Figure 4.4 shows the filter input β, the output y_{HP} and the squared output y_{HP}^2. In particular, the low frequency content of the input is cancelled, and the amplitude of the high-frequency components is identified. Figure 4.5 shows that the low-pass filter generates a signal proportional to the average power of the input y_S by using y_{HP}^2 as input signal.

In the second test, the input simulates a controller command β including an
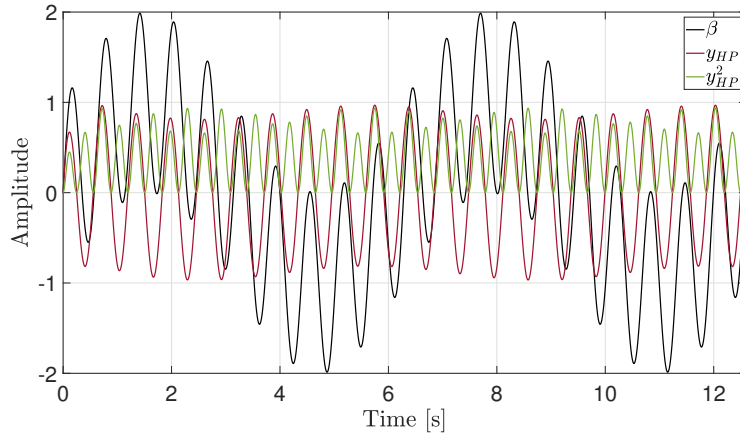
Figure 4.4. Spectral damper H_{HP} action of input signal.
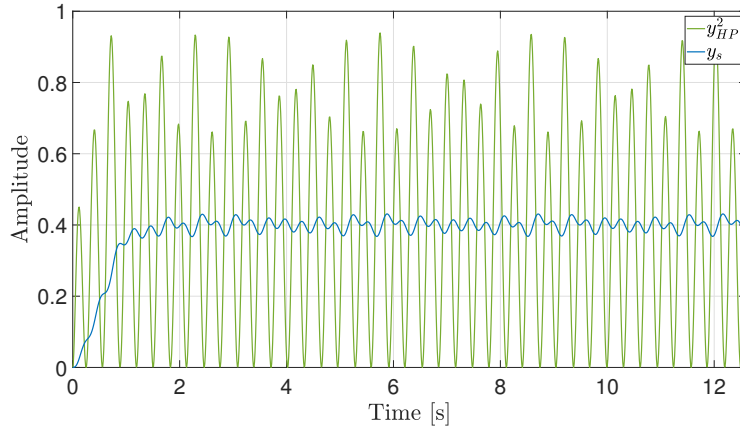
Figure 4.5. Spectral damper H_{LP} action.

undesired high-frequency component (Figure 4.6(a)). Figure 4.6(b) shows that the spectral damper is able to capture the high frequency components of the input command even in case of variable amplitude, generating the output y_s, the amplitude of which follows y_{HP}^2.

Spectral damper filter cut-off frequency set up. A common issue when implementing the AAC system for the first time is figuring out an appropriate value for the cut-off frequencies of the spectral damper filters. Available guidelines in literature [84, 54] are usually quite elusive, and suggest to specify the high-pass cut-off frequency ω_c^{HP} higher than the rigid-body bandwidth, in order to capture high-frequency components of the response; the cut-off frequency ω_c^{HP} of the low-pass filter H_{LP} is then tuned to smooth the spectral damper signal y_s.

According to the example proposed in Ref. [51], the following guidelines, hereafter referred as tuning (I), are adopted

(a) Simulated β (b) Spectral damper filter output
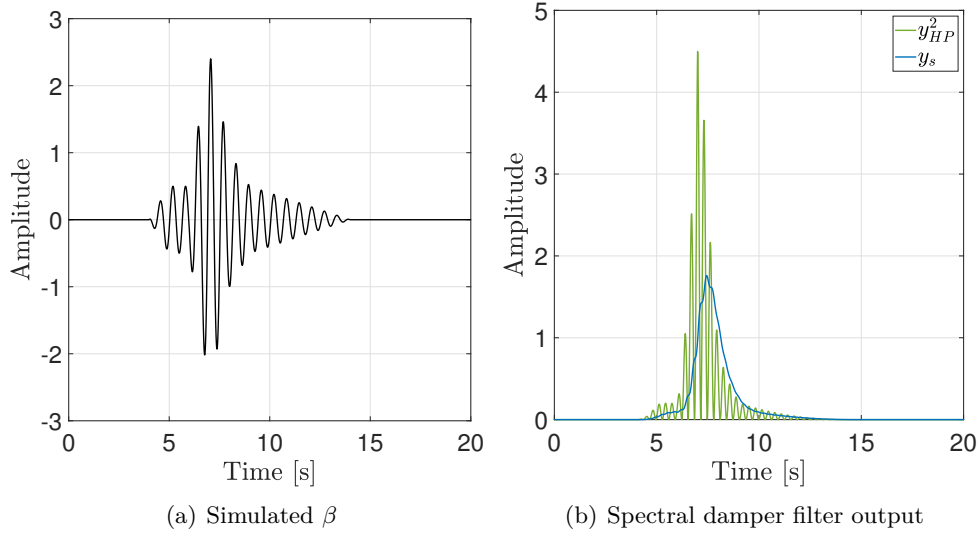
Figure 4.6. Spectral damper action on a simulated TVC command.

- High-pass filter $H_{HP}(s)$

    1. DC gain as small as possible

    2. passband gain of unity

    3. steep transition band, with the -3 dB bandwidth occurring approximately one octave above the rigid-body control frequency.[1]

- Low-pass filter $H_{HP}(s)$

    1. a maximally flat filter (such as a Butterworth filter), that is, a filter having the sharpest roll-off possible without inducing peaks in the Bode plot

    2. low-pass cut-off frequency ω_c^{LP} approximately matching the rigid-body control frequency.

In this study, a minor, yet significant, change in the cut-off frequencies of both filters is proposed, that will be referred as tuning (II) in what follows

- the high-pass cut-off frequency ω_c^{HP} is taken as the Rigid GM frequency

- the low-pass cut-off frequency ω_c^{LP} is one octave below, that is, $\omega_c^{LP} = \omega_c^{HP}/2$.

Figure 4.3 shows the Bode plots of the spectral damper filters according to tunings (I) and (II). The main difference is that the cut-off frequencies of the spectral

---

[1]In this study, the rigid-body control frequency is assumed to be the same as the rigid PM frequency.

damper filters set using tuning (II) are at higher frequency than those obtained with tuning (I), in order to not capture the rigid-body dynamics frequency content in control signal. Even though the difference appears negligible, the results presented in Sec. 4.2.4 will demonstrate the importance of the value of cut-off frequency, up to the point that it may significantly change the system response.

Leakage

The third term in Eq. (4.2), commonly referred to as *leakage*

$$\beta_{AAC}\left(k_T - 1\right) \tag{4.9}$$

acts like an elastic action that draws the value of k_T towards unity. In the absence of external excitation, the adaptive law slowly returns to a gain of $k_T = 1$, so that the BC is expected to effectively control the LV in nominal conditions.

4.2.2 AAC second law

An evolved formulation of the adaptive law is discussed in [54]

$$\dot{k}_T = p_{\text{hi}}(k_T)ae_r^2 - p_{\text{lo}}(k_T)\alpha y_s - \beta(k_T - 1) \tag{4.10}$$

It is apparent that the two adaptive laws (Eqs. 4.2 and 4.10) share the same structure, where the three AAC main features, that is, adaptive error term, spectral damper and leakage term are easily recognizable. The modified formulation of the adaptive gain law is recast directly in terms of the total loop gain k_T and the nonlinear dependence on the adaptive gain k_a is removed.

The terms p_{hi} and p_{lo} are nonlinear saturation functions that replace the logistic gain limiting term and the saturation on the spectral damper, respectively. The saturation functions p_{hi} and p_{lo} are

$$p_{hi}(k_T) = 1 - \left(1 + \exp\left[A\left(\frac{1}{A}\log\left(\frac{\epsilon k_{T_{max}}}{1 - \epsilon k_{T_{max}}}\right)\right) + k_{T_{max}} - k_T\right)\right]\right)^{-1} \tag{4.11}$$

$$p_{lo}(k_T) = \left(1 + \exp\left[A\left(\frac{1}{A}\log\left(\frac{1 - \epsilon k_{T_{max}}}{\epsilon k_{T_{max}}}\right)\right) + k_{T_{min}} - k_T\right)\right]\right)^{-1} \tag{4.12}$$

where A and ϵ are parameters defining the shape of the saturation functions, and

$k_{T_{max}}$ and $k_{T_{min}}$ are the maximum and minimum values of total gain. Figure 4.7 shows the saturation function obtained by setting $A = 100$ and $\epsilon = 0.002$. Unlike the logistic gain limiting, and the linear dependency of the spectral damper term from k_a, the saturation functions determines a sharp reduction of adaptation rate only when the total adaptive gain differs by about 10% of its minimum and maximum values.

(a) Lower bound factor   (b) Upper bound factor
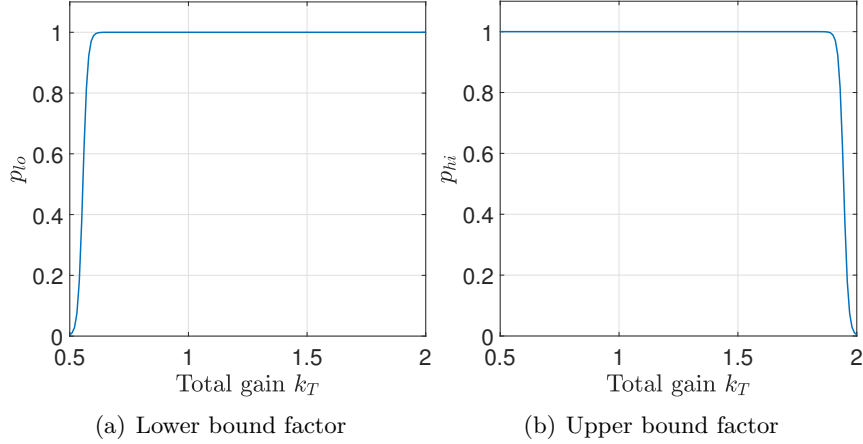
Figure 4.7. Saturation functions.

Moreover, upper limits are set on spectral damper input (y_s) and reference model error (e_r), so as to avoid large values of adaptation rate, in the form

$$e_{lim}^2 = \left(\frac{k_{T_{max}} - k_{T_{min}}}{a_{AAC} \Delta t_{elim}} \right) \tag{4.13}$$

$$y_{s_{lim}} = \left(\frac{k_{T_{max}} - k_{T_{min}}}{\alpha_{AAC} \Delta t_{sd_{lim}}} \right) \tag{4.14}$$

where $\Delta t_{e_{lim}}$ and $\Delta t_{sd_{lim}}$ are suitably specified time constants [54] set to 0.42 and 0.06, respectively.

4.2.3 AAC performance

In this section, the three primary features of the AAC algorithm are discussed, that is, i) minimal adaptation when the BC is performing nominally; ii) system gain increment in response to excessive command tracking errors in the presence of uncertainties; iii) gain reduction to prevent undesirable high frequency parasitic dynamics (i.e. control structure interaction) from driving the system to instability. To this end, the simulations are carried out using the reference model presented in Section 2.5, whose parameters are frozen at the most demanding condition, that

is, maximum dynamic pressure. The BC is designed according to the procedure illustrated in Chapter 3, and the resultant stability margins of the controlled system are reported in Table 4.1. AAC parameters are specified according to the classical tuning procedure reported in [51].

Table 4.1. BC Stability margins.

Stability Margin	Frequency	value
Aero GM	0.73 (rad/s)	6.51 (dB)
Rigid PM	2.72 (rad/s)	19.6 (deg)
Rigid GM	8.4 (rad/s)	7.35 (dB)
Flex PM$_1$	18.7 (rad/s)	125 (deg)
Flex PM$_2$	19 (rad/s)	145 (deg)
Flex GM	27 (rad/s)	16.4 (dB)

For each simulation, initial pitch angle of LV is equal to $2\,\mathrm{deg}$, and external disturbances are zero. Therefore, the simulation are carried out to compare the capability of BC and BC featuring AAC in leading the pitch angle to zero, its equilibrium value.
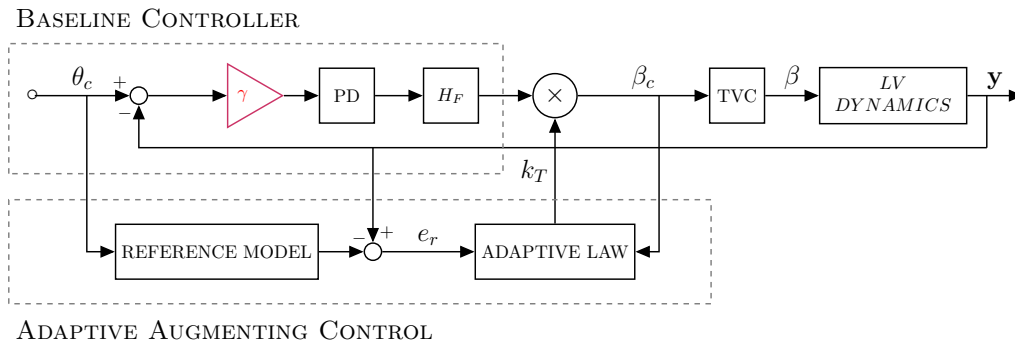
Figure 4.8. Architecture of LV control system with AAC and adjustable gain γ.

Moreover, the test are selected to investigate the effects that each term in the AAC law, Eq. (4.2), produces 'individually'. Therefore, as shown in the block diagram of the system with BC and AAC in Fig. 4.8, a gain γ is used to adjust the nominal BC loop gain up or down in order to demonstrate the system performance with degraded rigid-body low or high-frequency stability margins. The AAC algorithm should also adjust k_T to drive the system back within its nominal performance envelope.

Figure 4.9 shows the open-loop Nichols plot of the system controlled by BC in nominal condition (black dashed line) and for the two conditions obtained degrading the system gain-margin by multiplying BC by γ (solid lines).

(a) Forced low-gain   (b) Forced high-gain
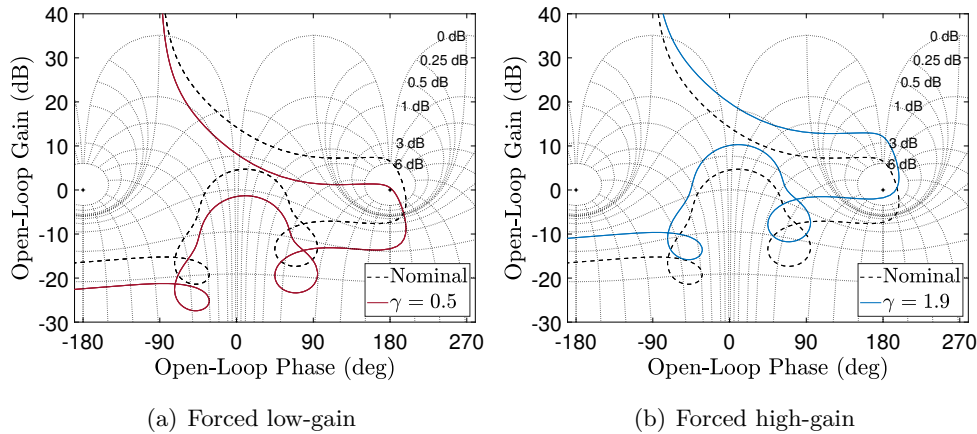
Figure 4.9. Nichols plot for the worst-case stability conditions.

A careful inspection of the typical Nichols plot for LV attitude control in atmospheric flight suggests that it is possible to excite primarily the adaptive error term if the system is forced to a condition, hereafter named Forced low-gain, where the low-frequency rigid-body gain margin (Aero GM) is approximately zero. The Forced low-gain is realized by pre-multiplying the controller output by a factor $\gamma = 0.5$ that is slightly less than the Aero GM in nominal conditions, as shown in Fig 4.9(a). In this case the adaptive error (and partially the leakage) term would try to increase the total adaptive gain k_T in order to recover the stability (i.e., augmenting gain margin).

Conversely, a Forced high-gain may be devised by using $\gamma = 1.9$ close to the inverse of the rigid GM, as shown in Fig 4.9(b), where the high-frequency rigid-body gain margin (Rigid GM) is close to zero. In this situation, the gain margin could be increased only by means of a reduction of the adaptive gain, that, in turns, can be obtained by the spectral damper and the leakage terms only.

Minimal adaptation

In this case, γ is set to 1 and hence the BC is able to control the nominal system. Figure 4.10 shows the comparison between the responses using BC and BC featuring AAC (BC+AAC) in terms of pitch angle θ, TVC rotation β and adaptive total gain k_T. In the absence of external disturbances and uncertainties, θ immediately converges to zero (Fig. 4.10(a)) for both controllers, and the adaptive total gain k_T slightly oscillates about unity as shown in Fig. 4.10(c). The initial spike in k_T is due to the rapid variation of nozzle angle (Fig. 4.10(b)) commanded by BC, that is captured by the spectral damper, that reduces k_T. The reduction of the total adaptive gain is rapidly compensated by the adaptive error term, that keeps
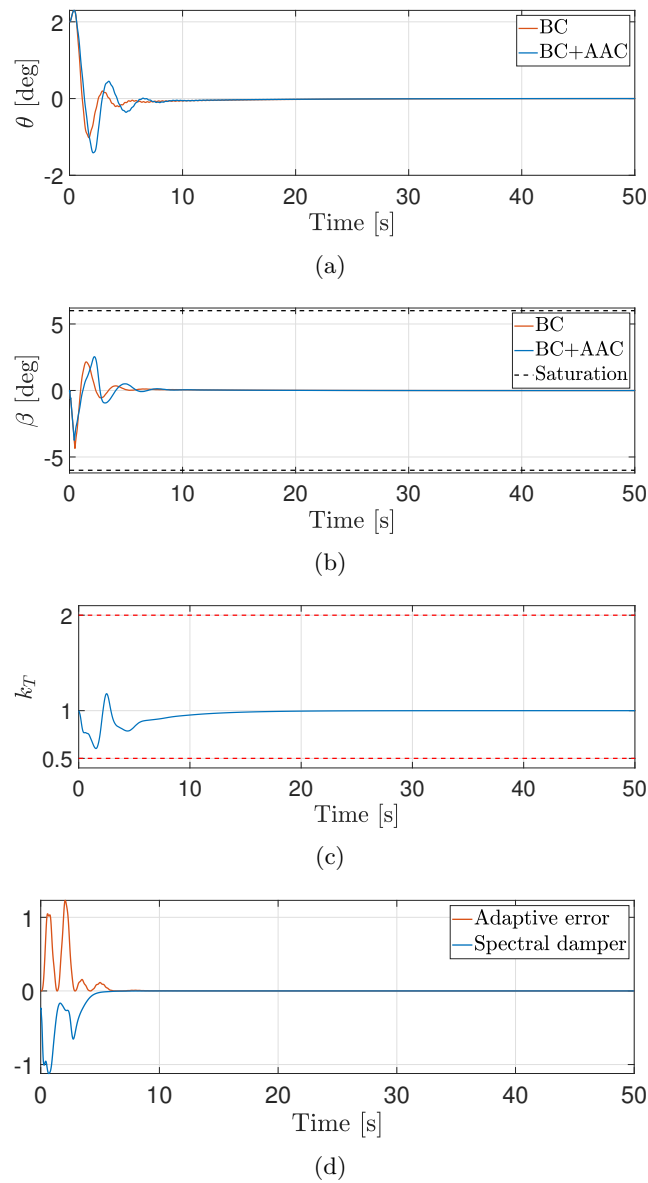
Figure 4.10. Time histories of (a) pitch angle θ, (b) nozzle angle β, (c) adaptive total gain k_T and (d) effects of adaptive error and spectral damper on $\dot{k}_a$ at $\gamma = 1$.

k_T about 1 as shown in Fig. 4.10(d). Note that BC and BC+AAC have similar performances, and minimal adaptation occurs as expected.

Forced low-gain condition

Figure 4.11 shows results for the forced low-gain condition, obtained for $\gamma = 0.5$. The BC operates in a marginally stable condition and the pitch response presents a oscillating behavior as shown in Fig 4.11(a). Conversely, the AAC algorithm immediately detects the error between system output and reference model, and

increases k_T in order to recover the loss of stability (Fig. 4.11(c)). This is clearly visible in Fig. 4.11(d) where the adaptive error term contribution to the adaptive rate $\dot{k}_a$ is greater than that of the spectral damper which results in an increase of k_T.
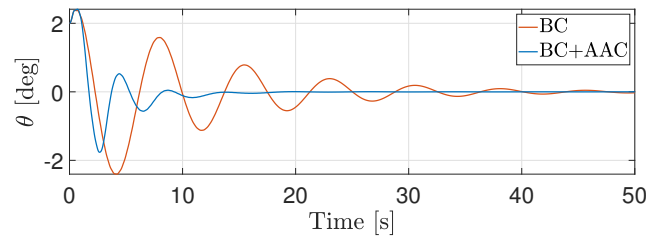
(a)
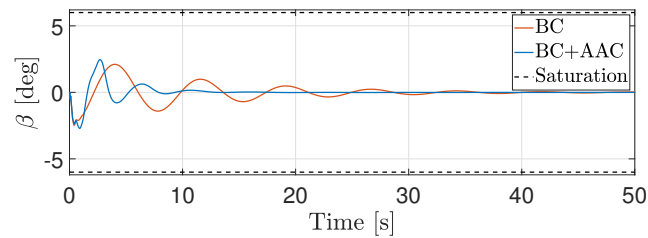
(b)
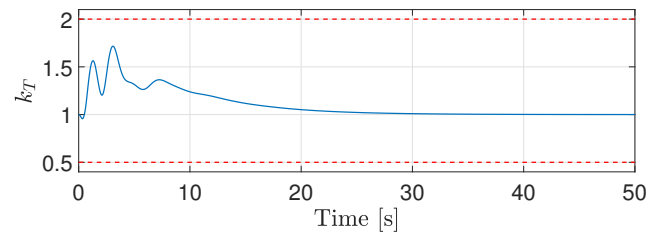
(c)
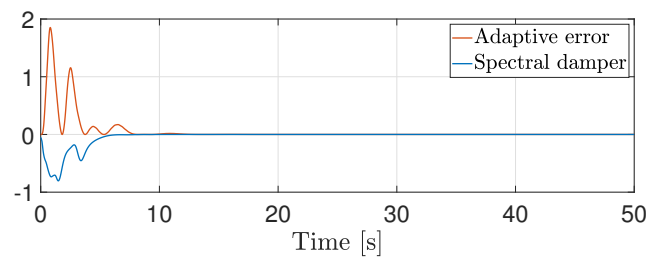
(d)

Figure 4.11. Time histories of (a) pitch angle θ, (b) nozzle angle β, (c) adaptive total gain k_T and (d) effects of adaptive error and spectral damper on $\dot{k}_a$ at $\gamma = 0.5$.

Forced high-gain condition

In this case, where $\gamma = 1.9$, the performance of the BC are degraded, and it is no longer possible to stabilize the system, and a LoV occurs (Fig. 4.12(a)).
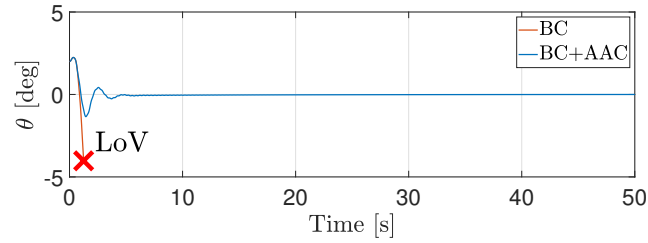
(a)
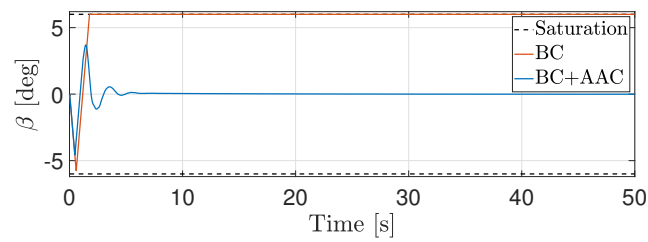
(b)
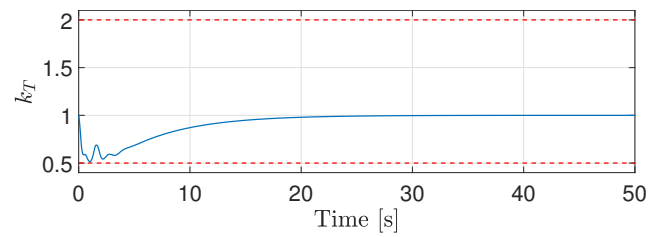
(c)
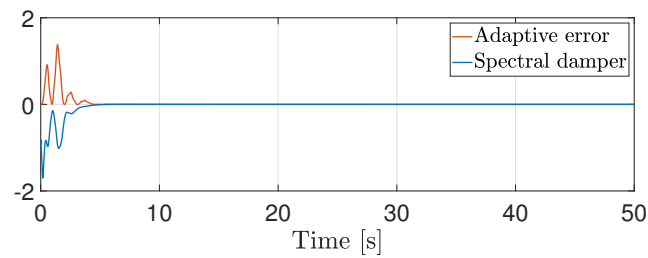
(d)

Figure 4.12. Time histories of (a) pitch angle θ, (b) nozzle angle β, (c) adaptive total gain k_T and (d) effects of adaptive error and spectral damper on $\dot{k}_a$ at $\gamma = 1.9$.

In particular, Fig. 4.12(b), where the TVC nozzle rotation time histories of BC and BC+AAC are reported, shows that the TVC is saturated by the BC command. As shown in Fig. 4.12(c) where k_T vs. time is reported, the AAC algorithm reduces

k_T, increasing the rigid GM and stabilizing the system. Finally, Fig. 4.12(d) shows that the spectral damper term provides the main contribution to the adaptive gain dynamics.

4.2.4   Spectral damper tuning assessment
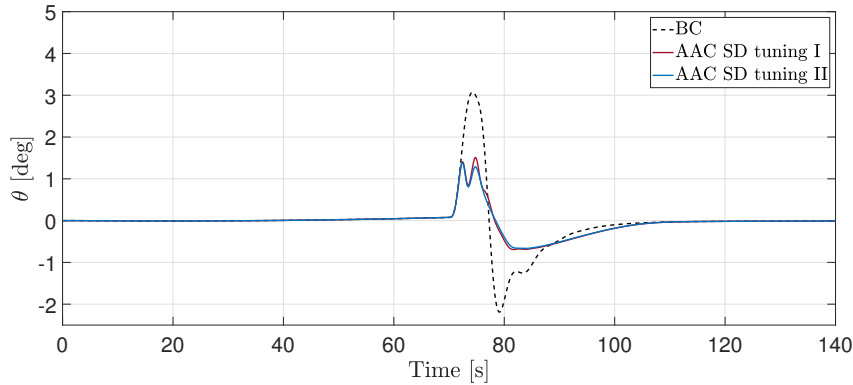
(a) Off-nominal (case A)
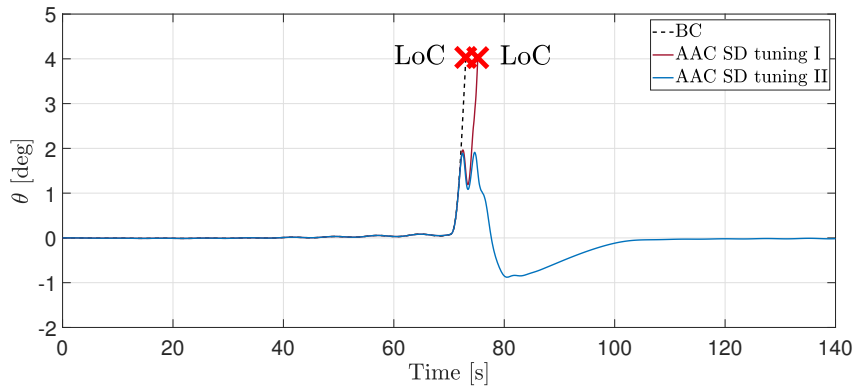
(b) Off-nominal (case B)

Figure 4.13. Pitch angle vs. time response to a synthetic, step-like, wind gust disturbance.

The effect of an incorrect tuning of the spectral damper cut-off frequencies is now discussed. Figure 4.13 shows the results of simulations carried out for two different off-nominal conditions, where the reference LV controlled by BC model is considered with constant parameters corresponding to the maximum dynamic pressure condition. Moreover, the LV is excited by step-like wind gust presented in Sec 2.7. The spectral damper parameters are specified according to the approaches referred as tuning (I) and tuning (II) (Sec. 4.2.1), while retaining the same values of all other parameters of AAC, as reported in Table 4.2.

Figure 4.13(a) refers to an off-nominal condition obtained by considering a positive 30% increment of A_6 and a negative 30% variation in the value of K_1

Table 4.2. AAC parameters.

	a_{AAC}	α_{ACC}	β_{AAC}	ω_c^{HP}	ω_c^{LP}
Tuning (I)	300	30,000	0.05	6 rad/s	3 rad/s
Tuning (II)	300	30,000	0.05	8 rad/s	4 rad/s
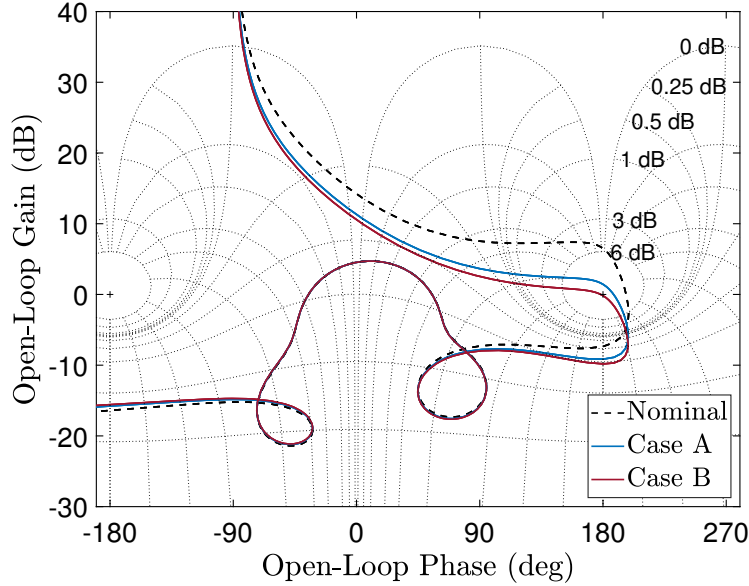
Figure 4.14. Nichols plots for cases A (blue line) and B (red line).

(Case A). As shown in the Nichols plot in Fig. 4.14, relative to the off-nominal condition Case A the system controlled by BC is stable, nevertheless the Aero GM is reduced and its value is close to zero. Response of both systems are in good agreement and an increment in performance with respect to the BC is apparent.

On the other hand, Fig. 4.13(b) reports the results for a slightly more challenging condition, where A_6 is increased by 35%, and the negative variation of K_1 is set at 40% (Case B). In this situation the system controlled by BC alone is unstable as it is apparent in the Nichols plot relative to Case B in Fig. 4.14. Tuning (II) is able to deal with an intense 30 m/s wind step-gust disturbance, while tuning (I) leads to a loss of control (LoC) event.

It is possible to explain this behavior by analyzing the locations of the spectral-damper cut-off frequencies ω_c^{HP} and ω_c^{LP}. For tuning (I) they are placed at a significantly lower values, than for tuning (II). Therefore, the spectral damper action is more invasive, and operates in a condition where only an increase of k_T is needed to recover the loss of gain margin, as shown in Figure 4.14.

4.3 Optimal AAC tuning

Current approach for tuning the AAC controller consists of setting three main elements

  i) Upper and lower bounds of the adaptive gain k_T equal, respectively, the the Aero GM and Rigid GM, related to the rigid-body dynamics of nominal system

 ii) Cut-off frequency of the spectral damper filters, ω_c^{HP} and ω_c^{LP}

iii) Gains a_{AAC}, α_{AAC}, and β_{AAC}.

The latter set of parameters is often specified using a time-consuming trial-and-error-procedures, as suggested in the literature [52, 38], where nonlinear simulations in the time domain are used to confirm that AAC behaves as expected.

In order to reduce the burden due to tuning activities and achieve a suitable tuning of AAC parameters to full exploit its potentiality, a rigorous methodology has been developed in this study, which could be applied to any LV configuration of interest. In particular, two approaches are proposed, both relying on the formulation of a robust design optimization (RDO) problem [69], the goal of which is to maximize a statistical metric that describes FCS performance measured over a set of representative simulations of LV flight. In more detail, adaptive law parameters are tuned with the aim of minimizing attitude error and aerodynamic loads. In so doing, also the occurrence of LoV events may be reduced. The tuning methodologies are based on the metrics $J_1 = \|\Delta\theta\|_\infty$ and $J_2 = \|H_{HP}\Delta\theta\|_1$ that measure FCS performance in a (single) time-domain simulation with respect to maximum angular displacement and unwanted oscillatory behavior, respectively, over the considered flight phase.

The first proposed approach requires minimal understanding of AAC features, and the performance index J_{MC} is identified using MC simulations. However, this procedure is computationally expensive since each evaluation of J_{MC} requires a large number of runs. In order to reduce the computational effort, a second tuning method is developed considering that, in marginal stability conditions, model reference error and spectral damper outputs have a major impact on the multiplicative gain variation. In this respect, the cost function J is evaluated by simulations in two worst-case conditions.

The two approaches rely on performing representative time-domain simulations, where the step-like deterministic wind disturbance, presented in Sec. 2.7, is applied. Nevertheless, the techniques could be easily extended to incorporate other limiting conditions that may be pertinent to a specific LV, and/or accommodate realistic wind

profiles if appropriate, for instance introducing real, in-flight wind measurements from previous missions.

4.3.1 RDO/MC approach

In the first approach, a problem dubbed RDO/MC is formulated as follows. Let c be a randomly generated realization of a scattered subset of LV coefficients, according to a prescribed uncertainty distribution. The vector

$$\boldsymbol{x} = \begin{bmatrix} a_{AAC} \\ \alpha_{AAC} \\ \beta_{AAC} \\ \omega_c^{HP} \\ \omega_c^{LP} \end{bmatrix} \tag{4.15}$$

of tuning parameters is determined that minimizes a combined merit index J_{MC} based on the worst performance, in terms of J_1 and J_2, across a set $\mathcal{C}$ of realizations $c \in \mathcal{C}$ that, in fact, is a Monte Carlo simulation campaign. The optimization problem is written as

$$\min_{\boldsymbol{x}} J_{MC}(\boldsymbol{x}) = \min_{\boldsymbol{x}} \left\{ \max_{c \in \mathcal{C}} J_1^{(c)} + \max_{c \in \mathcal{C}} J_2^{(c)} \right\} \tag{4.16}$$

where, following a few tests, it turns out that $\|\mathcal{C}\| = 100$ can provide a consistent statistic evaluation of J_{MC}.

A genetic algorithm (GA) [70] is used for solving the RDO/MC problem. GAs are well-known population-based, derivative-free, meta-heuristic techniques inspired by natural evolution, that have been successfully applied to a wide range of real-world problems of significant complexity. GA performs a global optimization and, thanks to its stochastic selection and mutation operators, has greater chances to evade from local optima than greedy methods [86]. Although population-based methods usually result in an order of magnitude lower convergence rate than deterministic optimization algorithms, adoption of GA for problem (4.16) is motivated by the fact that the objective function J_{MC} is non-differentiable and intrinsically noisy, as it is the result of a number of Monte-Carlo simulations. In this respect, the GA peculiarity of replacing most (if not all) of the population at each generation dramatically improves the success over other meta-heuristic algorithms [70].

Figure 4.15 shows the flowchart of the tuning procedure using GA. At the beginning, the algorithm creates a random initial population, the individuals of which are the candidate solutions of the problem. Next, for each individual, MC simulations are run using the set $\mathcal{C}$ of random scattered parameters. Then, the fitness
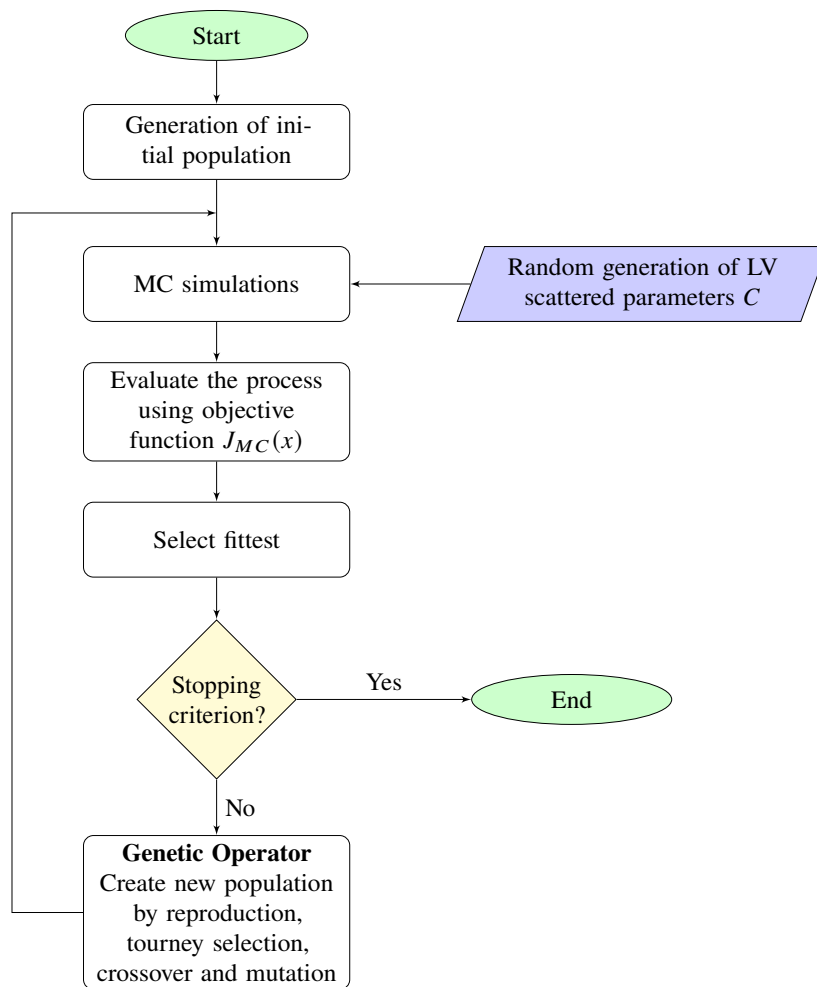
Figure 4.15. Flowchart of RDO/MC approach for tuning.

value of each possible solution is evaluated by calculating the objective function J_{MC}.

At this point, the GA uses the current population to create the children that make up the next generation. The algorithm selects a group of individuals in the current population, called parents, who contribute their genes (the elements of the solution vector) to their children. The algorithm usually selects individuals that have better fitness values as parents, identified through K-random tourney selections. Tournament selection involves running several "tournaments" among a few individuals chosen at random from the population. The winner of each tournament (the one with the best fitness) is selected for crossover. Simulated binary crossover with probability $p_c = 0.9$ combines subparts of two parent solutions to produce offspring. Moreover, GA creates mutation children by randomly changing the genes of individual parents. Through adaptive uniform mutation with probability

$p_m = 0.05$ the search space is explored by looking for better points.

Algorithm performance is further improved by using elitism, that is, the individuals in the current generation with the best fitness values automatically survive to the next generation, to ensure monotonic improvement in the best solution at any generation, and a partial restart mechanism that activates whenever the population diversity is low, in order to move away from the current population in which the GA is stuck and avoid sub-optimal solution. The process continues until the population converges to the global maximum or another stop criterion is reached. Further details on the GA optimization methodology can be found in [87].

4.3.2 RDO/min-max approach

The second tuning method should address the major issues experienced in the application of RDO/MC, that is, high computational cost and noisy objective function J_{MC} due to the quality of the approximate randomness generated by MC simulations. As outlined in Sec. 4.2.1, a suitable tuning of spectral damper can be achieved by selecting the cut-off frequencies as functions of the rigid-body GM frequency $\omega_{\text{GM rigid}}$, that is

$$\omega_c^{HP} = \omega_{\text{GM rigid}} \tag{4.17}$$

$$\omega_c^{LP} = \omega_c^{HP}/2 \tag{4.18}$$

The other gains a_{AAC}, α_{AAC}, and β_{AAC} define the relative weight of model-reference error, spectral damper, and leakage terms, respectively. Since the leakage is usually well-behaved, provided that a sufficiently small value of β_{AAC} is selected in the range $[0.05, 0.3]$, $\beta_{AAC} = 0.25$ is hereafter assumed.

(a) c_{A-GM} (b) c_{R-GM}
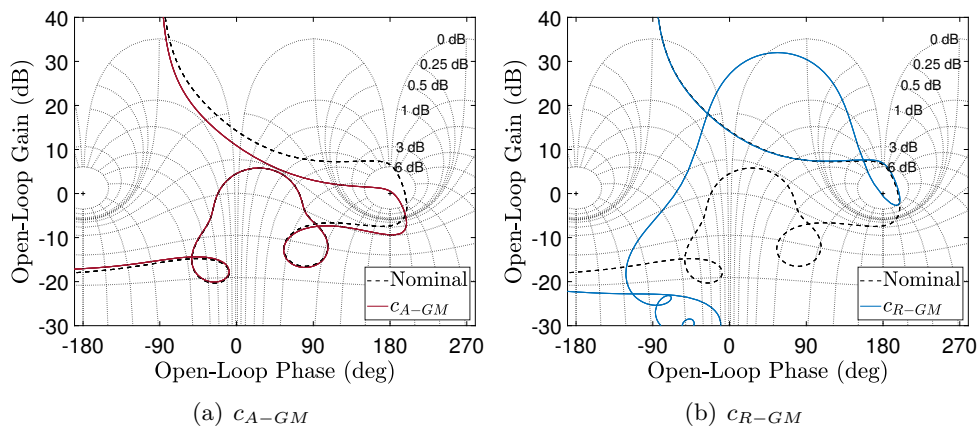
Figure 4.16. Nichols plots of the worst-case tuning conditions at $t = 72\,\text{s}$.

In facts, the design problem consists of tuning the remaining parameters, $\tilde{\boldsymbol{x}} = [\alpha_{AAC}, a_{AAC}]$ and, to this end, according to the comments in Sec 4.2.3 two limiting cases, due to parameter variations or off-nominal operations, may cause high values of either the reference model error or the spectral damper output. More precisely, when the system operates with a nearly zero low-frequency rigid-body GM (Aero GM), the large reference model error (and related term) provides the increment of total adaptive gain k_T necessary to recover the stability margin. Conversely, whenever the high-frequency rigid-body GM (Rigid GM) gets close to zero, k_T is reduced by the spectral damper action to, again, preserve system stability.

Therefore, a set of realizations $\mathcal{C}^\star = \{c_{\text{A-GM}}, c_{\text{R-GM}}\}$ is specified with reference to the aforementioned situations, that is, $c_{\text{A-GM}}$ is defined by increasing A_6 and decreasing K_1 by the same amount until the Aero GM approximates zero (Figure 4.16(a)), whereas $c_{\text{R-GM}}$ is obtained by reducing the elastic mode frequency ω_{BM} until the Rigid GM becomes negligible, while keeping A_6 and K_1 at their nominal values (Figure 4.16(b)). The design goal is thus to optimize FCS performance with respect to the most demanding (in terms of control action) of the two limit conditions, once a step-like wind gust [Eqs. 2.158] is assigned as disturbance. As a result, the RDO/min-max optimization problem is formulated as

$$\min_{\tilde{\boldsymbol{x}}} J(\tilde{\boldsymbol{x}}) = \min_{\tilde{\boldsymbol{x}}} \left\{ \max_{c \in \mathcal{C}^\star} J_1^{(c)} + \max_{c \in \mathcal{C}^\star} J_2^{(c)} \right\} \qquad (4.19)$$

that can be regarded as a scaled-down form of problem (4.16) where only two simulations per objective function evaluation are needed and, as an advantage, the objective function J is well-behaved with respect to the MC-based function J_{MC}.

The RDO/min-max problem is tackled by the Nelder-Mead simplex method [71], a local, derivative-free, optimization technique, so as improve convergence by limiting numerical errors in the finite-difference evaluation of J derivatives.

Figure 4.17 shows the flowchart of this second optimal tuning procedure. Nelder - Mead algorithm uses a simplex of $n+1$ points for n-dimensional solution vector, that is, $\tilde{\boldsymbol{x}}$ with $n = 2$. The algorithm first makes a simplex around the initial guess x_0, and for each test point (the vertices) of the simplex evaluates the objective function J. The method then performs a sequence of transformations of the simplex, named *reflected, expand, contract* and *shrink*, aimed at decreasing the cost function values at its vertices. At each step, the transformation is determined by computing one or more test points, together with their cost function values, and by comparison of these function values with those at the vertices, the algorithm replace the worst point with a point *reflected* through the centroid of the remaining n points. If this point
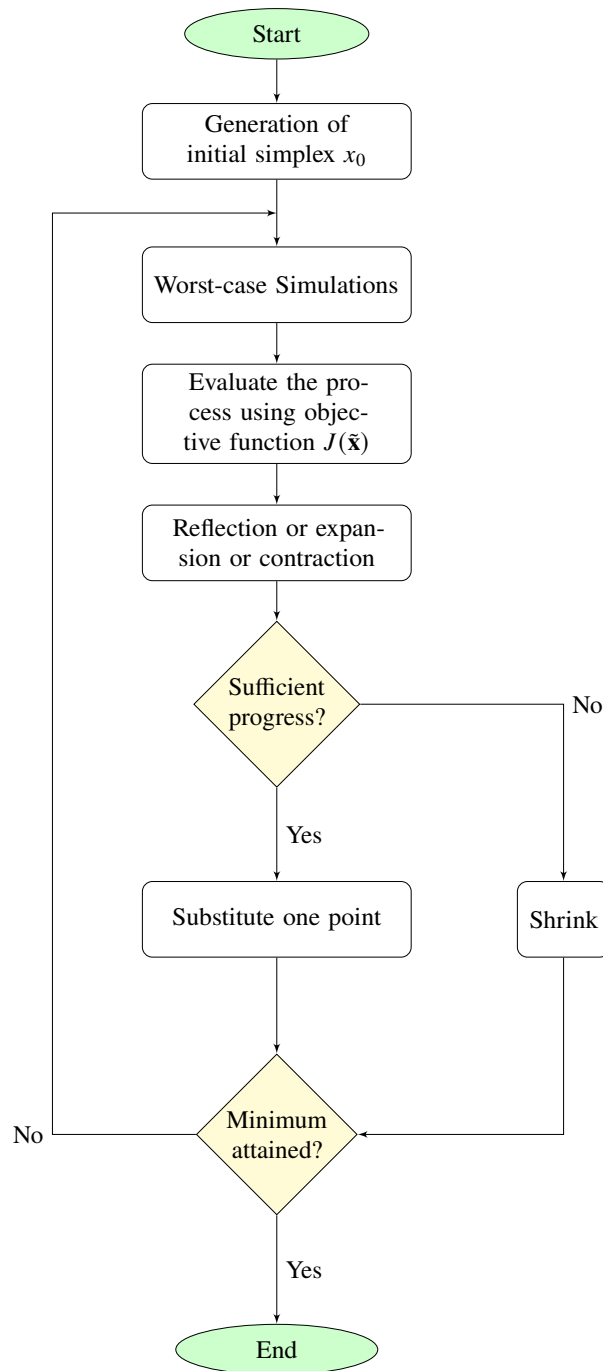
Figure 4.17. Flowchart of RDO/min-max approach for tuning.

is better than the best current point, the algorithm try to *expand* simplex along this line. If this new point is not much better than the other simplex point, but it is better than its previous value, the algorithm proceeds to *contract* the research point in the direction of the other test points. On the other hand, if this new point is

not much better than the worst previous value, the algorithm goes on to *shrink* the simplex towards the simplex vertex with the minimum value of the cost function. The iterations proceed until their stopping criterion is satisfied.

Provided that a reasonable initial guess is given, convergence is about one order of magnitude faster than a population-based global optimization algorithm. Global optimality of the solution can be pursued by repeatedly performing a random-start (or multiple-start) initialization procedure.

4.3.3 Results

Table 4.3 shows the AAC first law tuning parameters evaluated according to the two procedures discussed in Sections 4.3.1 and 4.3.2. As for the bounds on k_T, the values $k_0 = \mathrm{GM}_{aero}$ and $k_{a_{max}} = \mathrm{GM}_{rigid} - k_0$ are set, where the small margins in the max-Q condition (critical for stability) are taken into consideration. It is apparent that the optimal solutions present minor differences, as expected to some extent. The point is that the RDO/min-max method is significantly more efficient from a computational point of view. In particular, the solution is determined in about 15 min using an Intel Core i7-9700K CPU @ 3.60 GHz with 8 physical cores in spite of the fact that Nelder-Mead is a serial algorithm, whereas the RDO/MC approach takes roughly 16 hr on the same hardware while running a fully parallel algorithm. In this respect it is worth to remark that the deterministic Nelder–Mead simplex method can be effectively used for the RDO/min-max optimization in place of the stochastic GA because of the minor complexity of the problem and the smoother cost function.

As for RDO/MC, a minor tweaking of GA hyper-parameters is required in order to improve convergence and, notably, suitable values of population size N_P and number of generations N_G are to be selected. After a few tests showing that large values of the above parameters significantly increase computational time without improving quality of solution, N_P and N_G were set to 64 and 100, respectively.

Table 4.3. AAC optimally tuned parameters.

Tuning method	k_0	$k_{a_{max}}$	a_{AAC}	α_{AAC}	β_{AAC}	ω_c^{HP}	ω_c^{LP}
RDO/min-max	0.50	1.50	3,192.00	22,806.00	0.25	8.00	4.00
RDO/MC	0.50	1.50	3,856.00	43,277.00	0.17	8.77	1.67

Performance assessment for the FCS is carried out through extensive sets of simulations in the time domain, that consider the LV flight from lift-off to the first stage separation, for a wide scattering range of model parameters, as shown in

Table 4.4. Stochastic disturbances are generated by a Dryden wind model presented in Sec. 2.7.

Table 4.4. Scattering ranges for Monte Carlo simulations.

Parameter	Scattering range (%)
A_6	± 30
K_1	± 30
a_1	± 10
a_3	± 10
a_4	± 10
ω_{BM}	± 30

Tuning approaches are robust against the wind profiles used in the optimization process. This is demonstrated in Fig. 4.18, where the envelopes of the structural load $Q\alpha$ computed from MC campaigns of 1,000 simulations are shown for the FCS using the AAC tuned with two different wind profiles, that is, the step gust in Eq. 2.158 and a randomly generated wind based on the Dryden model in Eq. 2.159 (Fig. 4.18(a)). It is apparent in Fig. 4.18(b) that the wind profile used for tuning (the RDO/min-max method is used) has no effect on AAC performance as the two envelopes are indistinguishable. Similar results are obtained with different wind profiles, provided that a smooth and reasonably large variation of v_w near the max-Q condition is specified.

(a) Wind profiles for AAC tuning

(b) $Q\alpha$ envelope and safety limit vs. time: model parameters scattered as in Table 4.4, single wind profile
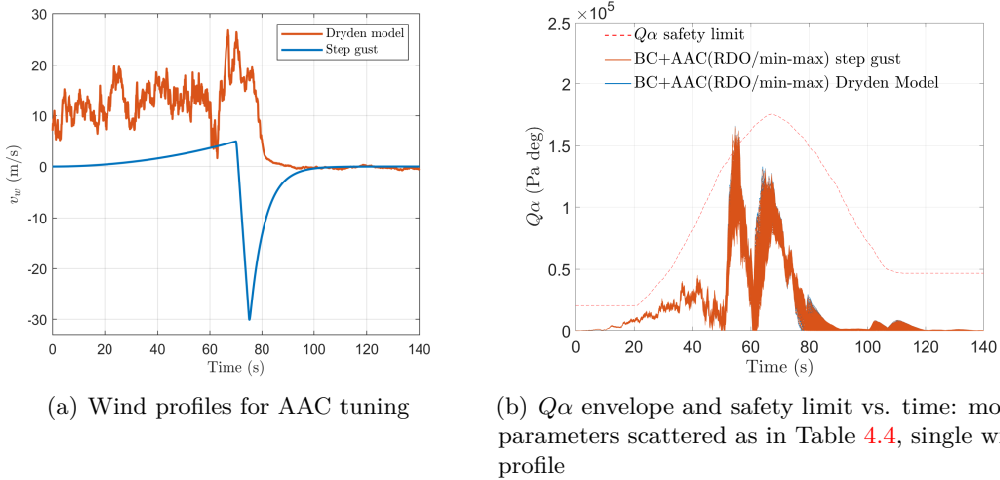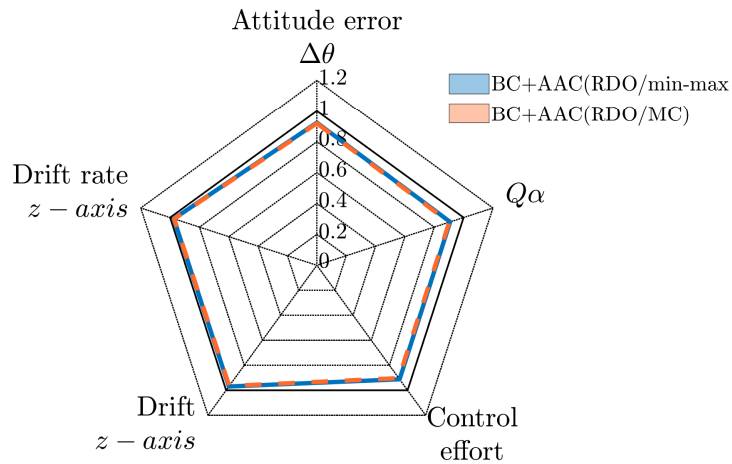
Figure 4.18. Effect of wind profiles on AAC tuning.

Figure 4.19 shows the L_2-norm of attitude error $(\Delta\theta)$, z-axis drift (z) and drift rate $(\dot{z})$, and structural load $(Q\alpha)$, together with the overall control effort (i.e. $\|\beta\|_1$), as computed for the AAC using the two tuning solutions. The norms are averaged

Figure 4.19. Normalized performance metrics over a Monte Carlo campaign based on 1,000 simulations.

over 1,000 simulations (model parameters are scattered according to Table 4.4) and normalized with respect to the same metrics computed for the LV controlled by the BC without augmentation. The results for the two formulations of the minimization problem are, in fact, indistinguishable, as was expected given the close values of optimal AAC gains. Control system performance is improved by AAC in terms of $Q\alpha$ (-13%) and attitude error (-8%), while keeping the same performance levels as BC on z-axis drift rate and displacement.

Table 4.5. Average L_∞-norm of performance parameters from Monte Carlo simulations

Controller	$\|\Delta\theta\|_\infty$ [deg]	$\|z\|_\infty$ [m]	$\|\dot{z}\|_\infty$ [m/s]	$\|Q\alpha\|_\infty$ [kPa deg]
BC	4.45	136.33	13.26	13.41
BC + AAC (RDO/MC)	4.04	136.13	12.58	11.73
BC + AAC (RDO/min-max)	4.05	136.48	12.62	11.79

Further insight in the outcome of AAC optimal tuning is provided in Table 4.5, where the effects of the adaptive law are shown in terms of L_∞-norms of $\Delta\theta$, z, $\dot{z}$, and $Q\alpha$, averaged over the MC runs. It is apparent that, even in terms of worst performance, $Q\alpha$ and attitude error are reduced, while $\dot{z}$ and, to an even lesser extent, z are only slightly affected by the adaptive law. The latter is due to the fact that the adaptive gain k_T does not depend on z-drift, but for the effect of θ on the reduction of $\dot{z}$ under wind disturbances.
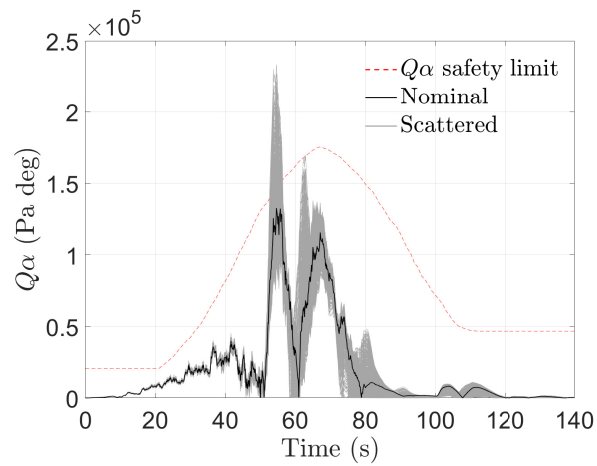
(a) BC
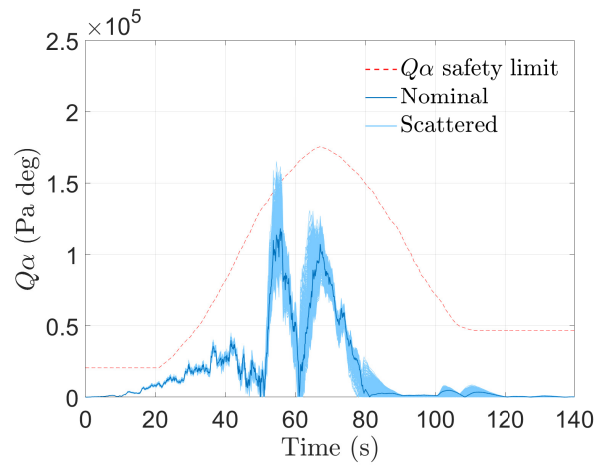
(b) BC + AAC (RDO/min-max)
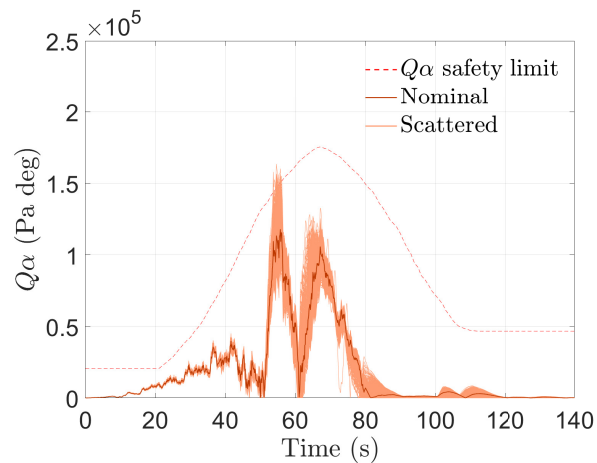
(c) BC + AAC (RDO/MC)

Figure 4.20. $Q\alpha$ envelope and safety limit vs. time: model parameters scattered as in Table 4.4, single wind profile; bold continuous lines indicate no scattering.

It is worth to observe that AAC performance assessment by averaging the aforementioned metrics over a large number of cases, many of which easily managed by the BC, does not properly represent the results and benefits of AAC action.

In this respect, Figure 4.20 shows the envelope of $Q\alpha$ together with the corresponding safety limit [9] over a Monte Carlo campaign based on 1,000 simulation runs, where model parameters are scattered as in Table 4.4 and a single wind profile is considered in all runs. Controller performances are compared for the LV featuring BC (Fig. 4.20(a)) and BC with augmentation, that is, RDO/min-max and RDO/MC tunings in Figs. 4.20(b) and 4.20(c), respectively. It is apparent in the figures, where the time-histories of $Q\alpha$ for nominal values of the parameters are also reported as bold continuous lines, that the two methodologies for optimal tuning provide similar results. Considering that simulations where $Q\alpha$ exceeds the threshold may end up with a LoV event, that is, a mission failure, the benefit of the AAC on mission success rate is now clearly visible, as RDO/min-max tuning prevents 270 out of 295 situations where the safety limit is violated that would have occurred without augmentation. Note that such a large number of cases with $Q\alpha$ above threshold is due to the combined effects of an extended scattering range and a tight safety envelope.
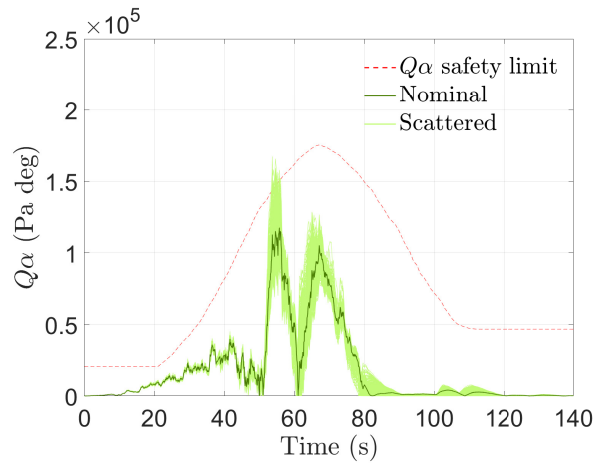
Figure 4.21. Application of RDO/min-max tuning procedure to the evolved AAC, Eq. (4.10): $Q\alpha$ envelope and safety limit vs. time; model parameters scattered as in Table 4.4, single wind profile; bold continuous line indicates no scattering.

As said, adaptive algorithms developed for SLS have evolved and consolidated over time. In this respect, the suitability of the proposed tuning approaches for the evolved AAC formulation [54] of Eq. 4.10 is investigated through the application of the RDO/min-max approach. Provided that the formulation of the optimal problem is straightforward, Fig. 4.21, where the structural load vs. time is reported for the

same MC campaign and wind profile of Fig. 4.20, shows that the FCS performance is comparable to that obtained with the adaptive law considered in this study.

A closer and final view of simulation outcome shows that AAC can successfully deal with scattering of rigid-body parameters as large as 30%, whereas relevant variations of bending mode frequency are more troublesome (mostly when the frequency decreases), particularly when the spectral damper is not properly tuned. In those circumstances, the AAC may occasionally degrade BC performance, and even lead the system to instability, as gain stabilization can hardly manage large offsets from nominal of elastic mode characteristics.

Chapter 5

Adaptive notch filter

5.1 Introduction

As discussed in Sec. 3.2.2, BCs for flexible LVs employ notch filters centered on the expected bending mode frequencies, resulting in a simple and effective way to suppress unwanted signal in the control loop and stabilize a specific mode. Low-pass filters are also included in the BC to provide the appropriate phase characteristics at the desired frequency so as to obtain a closed-loop damping of the mode greater than the passive damping [80]. Filter tuning is not trivial, as their performances depend on the accuracy in the determination of bending mode frequencies, which may be affected by uncertainties in the structural modeling of the vehicle. As the elastic mode frequencies present relevant variations during the flight due to the variation of vehicle inertial characteristics, BC design requires scheduling of filter parameters [62]. Moreover, effectiveness of the notch filter is sensitive to modeling errors.

In this respect, an adaptive notch filer using appropriate sensor output to exactly estimate frequency could be considered, in order to produce improved performance. In particular, the bending mode frequencies would be automatically tracked during flight and this information used to vary the filter frequency accordingly.

As mentioned in Sec 1.2 this approach has been studied extensively, and different methods to identify the elastic frequencies and adapt the notch filter have been proposed. A number of papers [67, 88, 89, 48] describe an adaptive notch filters, the design parameters of which are continuously updated by an adaptation algorithm that uses the pitch rate sensor output to estimate the unknown parameters of the filter and match in real-time the bending mode frequency. To this end, the recursive least-squares (RLS) method [68] is adopted that minimizes the weighted root-mean-square of the filter output.

This approach is used in this thesis to improve the BC robustness. Moreover, an Extended Adaptive Augmenting Control (EAAS) is developed, the architecture of which is based on the implementation of an adaptive algorithm for the bending mode filter of the BC augmented by AAC. Therefore, the EAAC should provide not only gain-margin adaptation by means of AAC, but also phase-margin adaptation.

5.2 Adaptive notch filter design

In this section, the main features of the adaptive notch filter (ANF) design are recalled. For implementation of the ANF, the number of parameters to be adapted should be kept at a minimum. Accordingly, the second-order notch filter, suitable for application to the adaptive algorithm has the following structure in the z-domain [67]

$$H_{AN}(z^{-1}) = \frac{N(z^{-1})}{D(\gamma z^{-1})} = \frac{1 + 2az^{-1} + z^{-2}}{1 + a(1 + \gamma)z^{-1} + \gamma z^{-2}} \tag{5.1}$$

where γ and a define, respectively, the notch filter bandwidth, that becomes narrower as γ approaches unity, and the notch frequency, adjusted by the adaptive algorithm as the bending mode frequency changes.

Being the pitch rate sensor signal $\dot{\theta}_{INS}(n)$ the filter input at the nth time step, the output is

$$y(n) = H_{AN}(z^{-1})\dot{\theta}_{INS}(n) = \frac{N(z^{-1})}{D(\gamma z^{-1})}\dot{\theta}_{INS}(n) \tag{5.2}$$

that is expressed as

$$y(n) = x(n) + 2ax(n - 1) + x(n - 2) \tag{5.3}$$

where $x(n)$ is given by

$$x(n) = \frac{1}{D(\gamma z^{-1})}\dot{\theta}_{INS}(n) \tag{5.4}$$

In order to design the adaptation algorithm by using the recursive least-square (RLS) method [68] , the AN parameter a is chosen so as to minimize a cost function that consists of the sum of filter output squares

$$E(n) = \sum_{i=0}^{n} \lambda^{n-i}y(i)^2 \tag{5.5}$$

where λ, the so-called forgetting factor, is a positive constant close to, but less than, unity. The forgetting factor is intended to ensure that 'older' data are forgotten in order to follow the statistical variations of the observable data.

By using the Eqs. (5.3) and (5.4), Eq. (5.5) can be written as

$$E(n) = \sum_{i=0}^{n} \lambda^{n-i}[A(i)a + B(i)]^2 \qquad (5.6)$$

where the parameters are expressed as

$$A(i) = 2x(i-1) \qquad B(i) = x(i) + x(i-2)$$

The design parameter a that minimizes the cost function is found imposing the condition $\partial E/\partial a = 0$, which leads to the following relationship

$$a(n) = -\frac{\sum_{i=0}^{n} \lambda^{n-i} A(i)B(i)}{\sum_{i=0}^{n} \lambda^{n-i} A^2(i)} = -\frac{\eta(n)}{2\Phi(n)} \qquad (5.7)$$

where $\Phi(n)$ and $\eta(n)$ are, respectively, the time-average correlation and cross-correlations. In the recursive implementations of the least-squares method, the estimation of notch frequency is started with prescribed initial conditions, and the information contained in the new data samples is used to update the old estimates. In this respect, $\Phi(n)$ and $\eta(n)$ are expressed in their recursive form [68] as

$$\Phi(n) = \lambda\Phi(n-1) + x(n-1)^2 \qquad (5.8)$$

and

$$\eta(n) = \lambda\eta(n-1) + x(n-1)\{x(n) + x(n-2)\} \qquad (5.9)$$

Finally, the natural frequency of the bending mode is estimated as follows

$$\omega_{id}(n) = \frac{\cos(-a(n))^{-1}}{\Delta T} \qquad (5.10)$$

where ΔT is the the sampling time.

5.3 Extended adaptive augmenting control

The ANF is integrated in a control architecture featuring the BC augmented by the AAC presented in Sec 4.2. The resulting control architecture shown in Fig. 5.1 is called Extended Adaptive Augmenting Control (EAAC).

In its classic implementation for LVs, the BC transfer function, reported in Eq. (3.1), presents the product $H_F = H_X(s)H_N(s)$, which refers to the non-adapted filters recalled in Section 3.2.2 (Eqs. (3.19)-(3.16)). When the ANF is devised, the
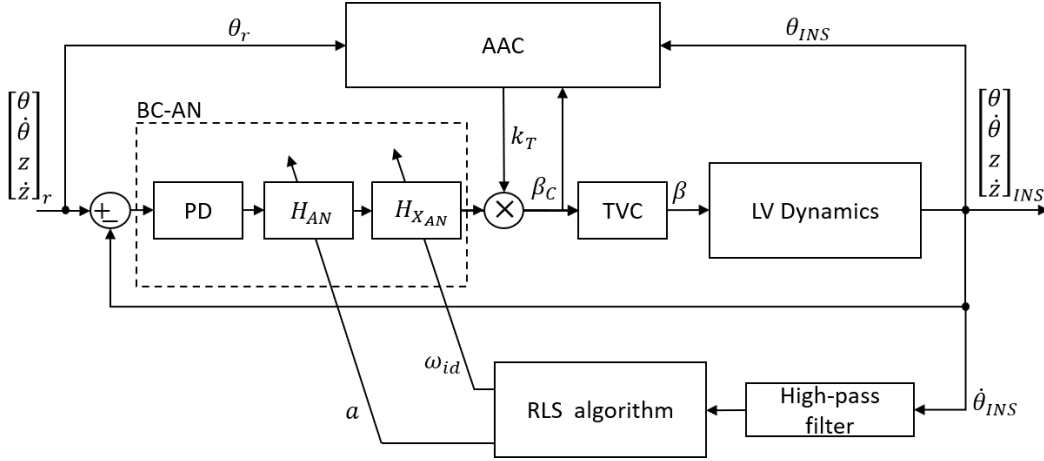
Figure 5.1. Architecture of EAAC system.

transfer function of the BC, dubbed BC-AN, is

$$\boldsymbol{K}_{BC-AN}(s) = [K_{P_\theta} \quad K_{D_\theta} \quad K_{P_z} \quad K_{D_z}]H_{X_{AN}}(s)H_{AN}(s) \tag{5.11}$$

where $H_{AN}(s)$ is the ANF in Eq. (5.1), and $H_{X_{AN}}(s)$ is the adaptive form of the low-pass filter H_X, that is realized by using the bending mode frequency identified by the RLS adaptive algorithm, that is, with reference to Eq. (3.16), $\omega_p = 1.3\,\omega_{id}$.

A high-pass filter is applied to the pitch rate signal in order to cancel out the frequency component related to the rigid-body dynamics so as to improve the tracking capabilities of the adaption algorithm. The filter transfer function is

$$H_{HP_{AN}}(s) = \frac{s^2}{s^2 + 2\zeta_{HP_{AN}}\omega_{HP_{AN}}s + \omega_{HP_{AN}}^2} \tag{5.12}$$

where $\zeta_{HP_{AN}}$ is set to 0.7, and $\omega_{HP_{AN}}$ is equal to the highest frequency of rigid-body dynamics.

Finally, the output a of the adaptive algorithm (Eq. (5.7)) is regularized by the smoothing function

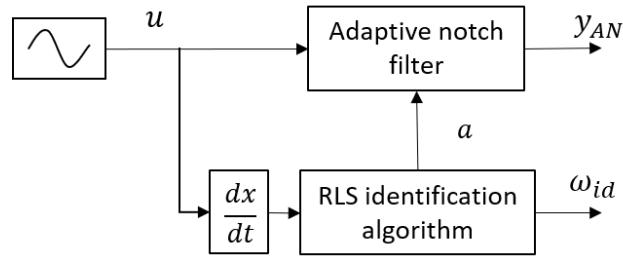$$a_{actual}(n) = a(n)0.05 + (1 - 0.05)a(n-1) \tag{5.13}$$

5.4 Results

In this section, simulations are carried out to analyze the features and evaluate the performance, in term of frequency tracking, of the ANF. To this end, a simulation model has been devised, the block diagram of which is presented in Fig. 5.2, where

the RLS ANF is fed by different sine wave signals.

Figure 5.2. ANF scheme used in simulation tests.
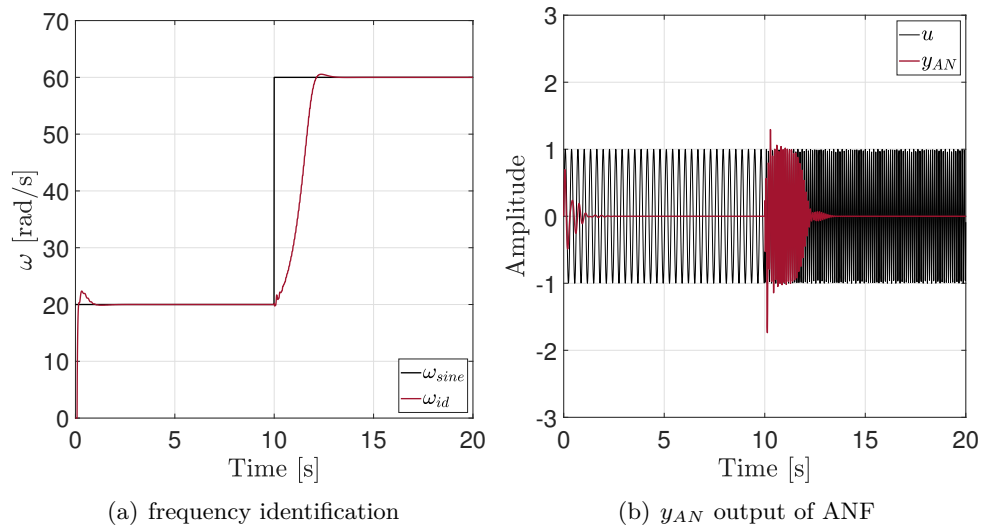
5.4.1   Variable frequency sine wave

The first test aims to verify the capacity of the ANF to identify and notch a time-varying frequency sine wave signal u

$$u(t) = \sin\left(\omega t\right) \qquad \text{with} \qquad \omega = \begin{cases} \omega_i = 20\,\text{rad/s} & t < 10\,\text{s} \\ \omega_f = 60\,\text{rad/s} & t > 10\,\text{s} \end{cases} \tag{5.14}$$

Figure 5.3 shows the frequency estimated by the ANF and the comparison between filter input u and output y_{AN}. The ANF, obtained by setting $\lambda = 0.98$ and $\gamma = 0.9$, is able to estimate the sine wave initial frequency ω_i (Fig. 5.3(a)) and to effectively cancel the sinusoidal oscillations (Fig. 5.3(b)). Moreover, the ANF captures the frequency variation of the sine wave occurring at $t = 10\,\text{s}$, and the estimated frequency converges at the actual sine wave frequency ω_f in about 3 s, as shown in Fig. 5.3(a). It appears in Fig. 5.3(b), that the ANF output y_{AN}, after a transient phase due to the sharp sine frequency variation, is led to zero by the ANF.

An accurate setting of parameters λ and γ is a crucial aspect in implementing the ANF. The forgetting factor λ determines the adaptation rate, where a smaller value of λ provides faster adaptation by placing less weight on the past data. Figure 5.4(a), where results relative to different values of λ and $\gamma = 0.9$ are reported, shows that as the forgetting factor λ decreases, the filter response becomes quicker, but the estimation performance degrades.

As said, when γ approaches unity, the notch filter bandwidth becomes narrower and a degradation on the estimation of the time-varying frequency appears, as shown in Fig. 5.4(b), where the frequency identified by the filter for different values of γ and $\lambda = 0.98$ is reported. In this respect, a larger bandwidth increases the estimation performance but, when the ANF is applied in the attitude control problem, an

(a) frequency identification

(b) y_{AN} output of ANF

Figure 5.3. ANF response to a variable frequency sine wave signal.

(a) λ variations

(b) γ variations
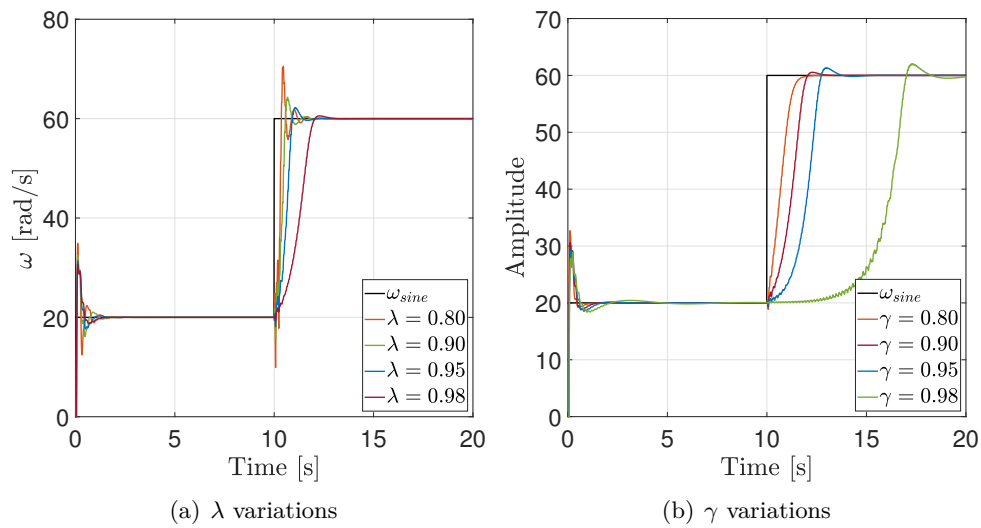
Figure 5.4. ANF response to a variable frequency sine wave signal for different value of forgetting factor λ and filter bandwidth γ.

excessively large bandwidth degrades the rigid-body dynamic response performance.

5.4.2 Multiple sine wave

The behavior of the ANF is evaluated when the signal u, made by adding two sinusoids with different frequencies (ω_1 and ω_2) and amplitudes (A_1 and A_2), is considered as input, that is

$$u(t) = A_1 \sin(\omega_1 t) + A_2 \sin(\omega_2 t) \tag{5.15}$$

Figure 5.5 refers to a test, dubbed Case I, where u is obtained setting $A_1 = A_2 = 1$ and $\omega_1 = 10\,\mathrm{rad/s}$ and $\omega_2 = 30\,\mathrm{rad/s}$. The RLS identification algorithm promptly estimates the higher frequency ω_2, as shown in Fig. 5.5(a). The filter cancels out the higher frequency component in the signal u, and y_{AN} is a unity amplitude sine wave with a frequency of $10\,\mathrm{rad/s}$ at steady-state, as expected.

(a) frequency identification

(b) ANF y_{AN} output
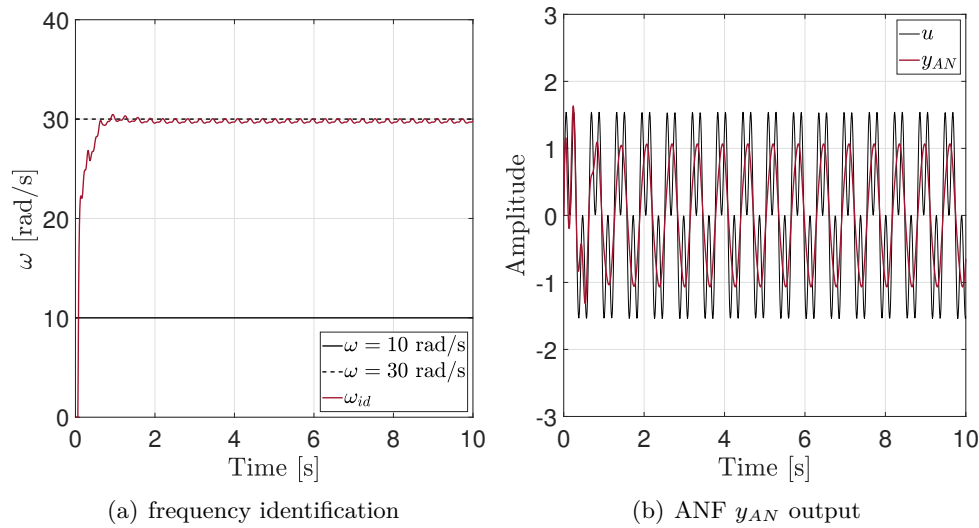
Figure 5.5. Case I: $A_1 = A_2 = 1$, $\omega_1 = 10$ and $\omega_2 = 30$.

When Case II is considered, reference is to be made to Fig. 5.6, where the results obtained for u specified by setting $A_1 = 2$, $A_2 = 1$, $\omega_1 = 10\,\mathrm{rad/s}$ and $\omega_2 = 30\,\mathrm{rad/s}$, are presented. In this situation, the estimated frequency is the lowest among the two above because the adaptation algorithm is based on the "vibration power" of the signal [88], that is, the RLS identification algorithm tracks the frequency of the signal with the major signal power and frequency, that may be roughly estimated as $(A^2/2)\omega$ for a sine wave. The fact that the ANF algorithm tracks low-frequency dynamics instead of those at high-frequency, may cause issues in implementing the filter in the BC. In particular, identification of the bending mode frequency during flight could be perturbed by the low frequency rigid-body dynamics, that can assume large amplitude. An inaccurate estimation of the bending mode frequency leads to instability as the notch filter is incorrectly centered and, consequently, not able to stabilize the bending mode.

In order to avoid that the ANF tracks the low-frequency component in the input signal, the high-pass filter in Eq. (5.12) is applied to u. Figure 5.7 shows the results obtained for Case II when a high-pass filter with cutoff frequency at $15\,\mathrm{rad/s}$ is considered. The ANF accurately tracks and notches the high frequency content in the signal u, as it is visible in Fig. 5.7(a), when the filter input u and output y_{AN}

(a) frequency identification

(b) y_{AN} output of ANF
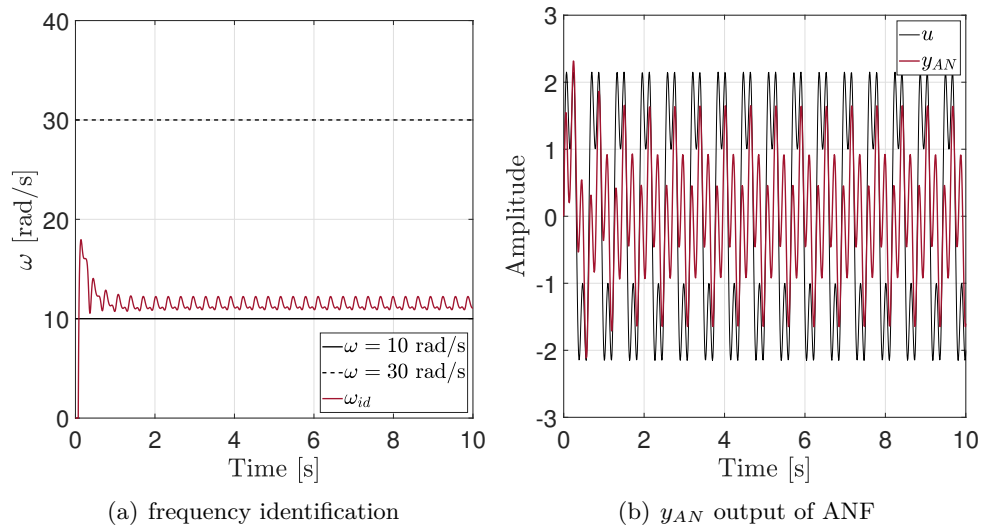
Figure 5.6. Case II: $A_1 = 2$, $A_2 = 1$, $\omega_1 = 10$ and $\omega_2 = 30$.

are also compared (Fig. 5.7(b)).

(a) frequency identification

(b) y_{AN} output of ANF
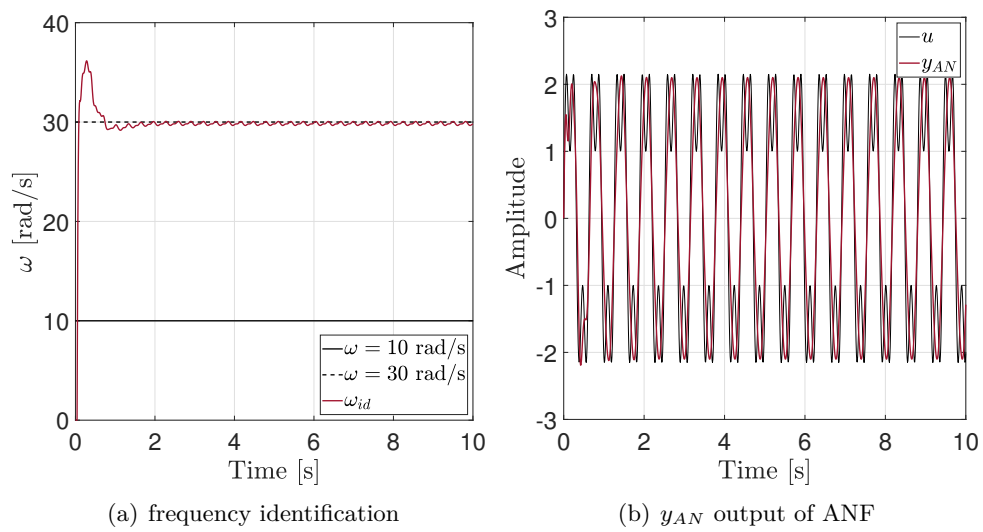
Figure 5.7. Case II with high-pass filter: $A_1 = 2$, $A_2 = 1$, $\omega_1 = 10$ and $\omega_2 = 30$.

Chapter 6

Results and discussion

In this chapter, the performances of BC+AAC and EAAC are evaluated using the linear, time-varying and planar model of the LV pitch and lateral dynamics discussed in Sec. 2.8, and simulating the atmospheric phase of flight from launch through an altitude of $60\,\mathrm{km}$ ($t = 140\,\mathrm{s}$) in situations where the LV undergoes large wind disturbances. In this respect, a stochastic Dryden wind disturbance, the mathematical model of which is presented in Sec. 2.7, is taken into consideration for the simulations; Fig. 6.1 shows the wind speed as function of time.
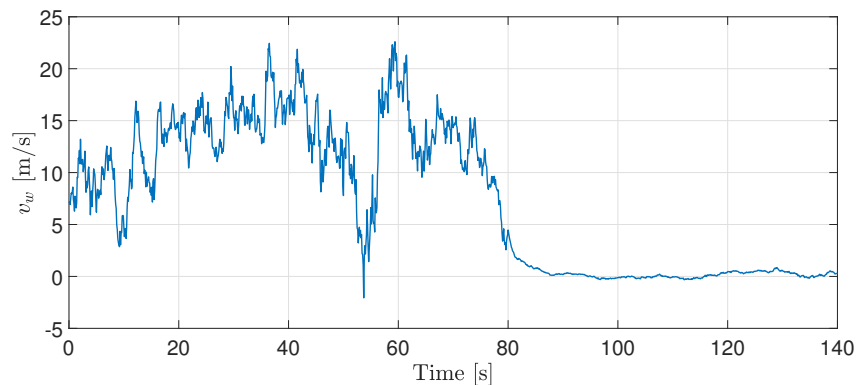
Figure 6.1. Dryden wind gust profile.

To this end, the AAC second law recalled in Sec. 4.2 is implemented in BC+AAC and EAAC (see Sec. 4 and 5.3, respectively) and the AAC parameters are tuned solving the robust design optimization RDO/min-max problem discussed in Sec. 4.3.2. Table 6.1 shows the values of AAC parameters adopted in the simulations.

In more details, in Sec. 6.1 simulation results for nominal conditions and different parameter scattering sets are presented. In Sec. 6.2 two worst case scenarios, that involve significant reductions of the bending mode frequency combined with large rigid-body parameter scattering, including modal gain at sensor are discussed in

Table 6.1. AAC optimally tuned parameters.

$k_{T_{min}}$	$k_{T_{max}}$	a_{AAC}	α_{AAC}	β_{AAC}	ω_c^{HP}	ω_c^{LP}
0.50	2.00	1,768.70	12,411.73	0.25	8.00	4.00

order to demonstrate the effectiveness of the adaptive algorithms beyond the BC capability. Finally, in Sec. 6.3 the main performance metrics are evaluated through Monte Carlo campaigns for scenarios with variations of several model parameters.

6.1 Performance assessment

In this section, the performance of BC augmented by AAC and EAAC is analyzed with the aim to demonstrate that the adaptive control architectures developed in the thesis can achieve

- minimal adaptation in nominal conditions

- improvement in performance and robustness with respect to BC as the dispersion of parameters increases

- high effectiveness in stabilizing the system for large scatterings that lead to the failure of LV controlled by BC.

According to [20] and to the discussion in Sec. 3.3.2, limit configurations are defined for the rigid stability margins as follows

- case LF (or Low Frequency) where the Aero GM is minimum

- case HF (or High Frequency) where the Rigid GM is minimum.

The two scattering sets for the rigid-body parameters, that lead to LF and HF cases are shown in Table 6.2. Moreover, another situation where stability is extremely low, dubbed LF$^+$, is specified as a superset of LF configuration, where the aerodynamic parameter A_6 is increased of 35% and control authority K_1 is reduced by 35%.

The effects of the three sets of parameter variations on system stability are shown in Fig. 6.2, where the Nichols plots of the open-loop linear model at $t = 72\,\mathrm{s}$, corresponding to the already cited maximum dynamic pressure condition are reported. The frequency response clearly shows that the LF and LF$^+$ scatterings are more critical for the stability because rigid-body gain margin (Aero GM) at low frequency is reduced. Since the LF, HF and LF$^+$ cases are only related to rigid-body parameter dispersions, the variation of the 1st bending mode natural frequency ω_{BM} is also

Table 6.2. Scattering sets LF, HF and LF$^+$.

Parameter	LF (%)	HF (%)	LF$^+$ (%)
A_6	+30	−30	+35
K_1	−30	+30	−35
V	+10	−10	+10
a_1	+10	−10	+10
a_3	−10	+10	−10
a_4	−10	+10	−10
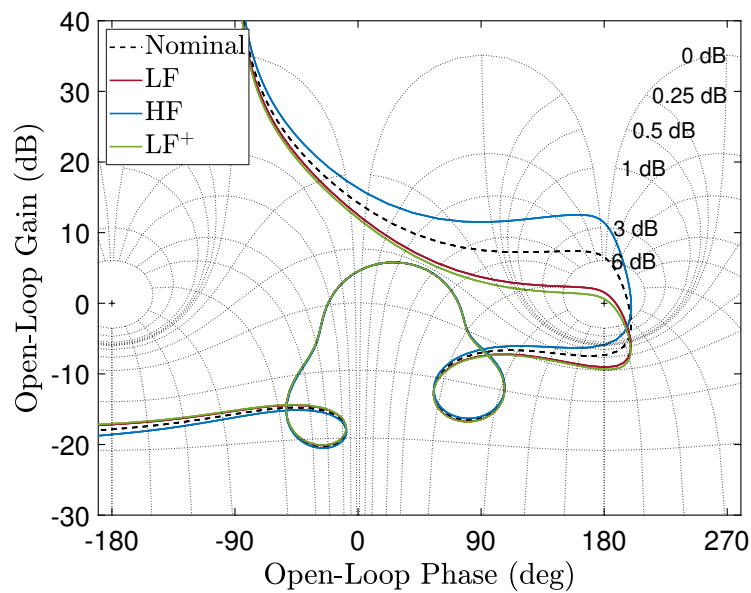
Figure 6.2. Nichols plots in nominal condition (dashed line), and for LF, HF and LF$^+$ scattering sets at $t = 72$ s.

considered in the tests, and its effects are illustrated in the Nichols plots of Fig. 6.3 for the LF condition (that is the most demanding for the rigid-body dynamics control), and ω_{BM} variations equal to -30% and -45% (Fig. 6.3(a)), as well as +30% and +45% (Fig. 6.3(b)).

As the bending mode frequency dispersion increases for both positive and negative variations, Fig. 6.3 shows that the "hump" in the range [180 deg, -180 deg], relative to the bending mode, rapidly grows because the notch and low-pass filters, centered on the nominal value of ω_{BM} are not able to effectively gain- and phase-stabilize the bending mode, and the dispersion eventually makes the system unstable.

The tests are listed in Table 6.3.

- Test 0 is intended to analyze the behavior of controllers in nominal conditions

- Test 1-2 are run to assess controller performances when only rigid-body pa-
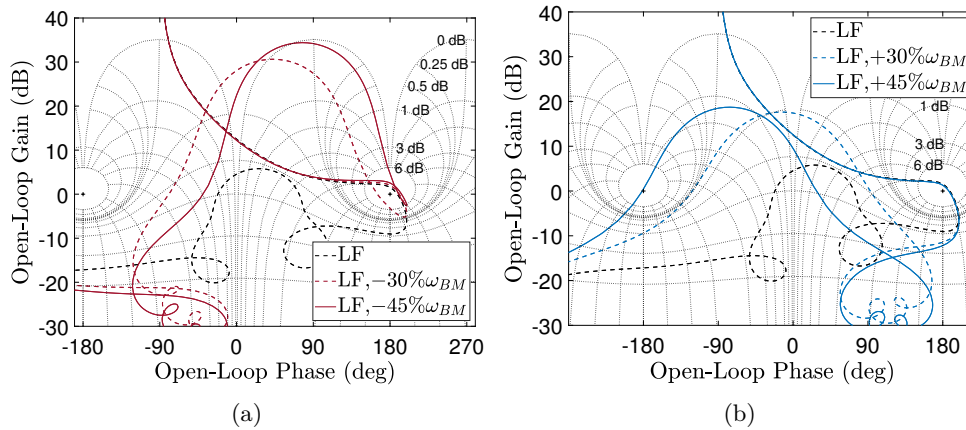
Figure 6.3. Nichols plot for LF condition with (a) negative variations of ω_{BM} and (b) positive variations of ω_{BM}.

rameter scattering is taken into account

- Tests 3-6 are conducted to analyze the effect of the adaptation algorithms at the limits of BC stability range, for large scattering combinations of rigid-body and flexible parameters

- Tests 7-9 are intended to evaluate the extended safety envelope capabilities provided by the adaptive schemes; to this end the level of uncertainty is increased beyond the operational range of BC.

Table 6.3. Test results: ⊘ specification is met, ⊗ specification in not met. ($Q\alpha$) aerodynamic load is in safety envelope. (LoC) system is stable. ($\Delta Q\alpha$) percentage difference of maximum $Q\alpha$ w.r.t. BC alone.

	scattering set		BC		BC+AAC			EAAC		
Test	RB	ω_{BM}	$Q\alpha$	LoC	$Q\alpha$	LoC	$\Delta Q\alpha$	$Q\alpha$	LoC	$\Delta Q\alpha$
0	Nominal	Nominal	⊘	⊘	⊘	⊘	-8%	⊘	⊘	-9%
1	LF	Nominal	⊗	⊘	⊗	⊘	-28%	⊗	⊘	-27%
2	HF	Nominal	⊘	⊘	⊘	⊘	-2%	⊘	⊘	-2%
3	LF	+30%	⊗	⊘	⊗	⊘	-30%	⊗	⊘	-30%
4	HF	+30%	⊘	⊘	⊘	⊘	-3%	⊘	⊘	-3%
5	LF	-30%	⊗	⊘	⊗	⊘	-26%	⊗	⊘	-26%
6	HF	-30%	⊘	⊘	⊘	⊘	0%	⊘	⊘	0%
7	LF$^+$	Nominal	⊗	⊗	⊗	⊘	-	⊗	⊘	-
8	LF	+45%	⊗	⊗	⊗	⊗	-	⊗	⊘	-
9	LF	-45%	⊗	⊘	⊗	⊗	-	⊗	⊘	-22%

Table 6.3 shows results related to FCS performance for the three considered

control architectures. In particular, entries $Q\alpha$ and LoC indicate if the controllers meet the performance specification, that is, the aerodynamic load stays within $Q\alpha$ safety envelope during the flight, and a LoC event is avoided (i.e. controlled system is stable), respectively. Moreover, the percentage difference between the maximum $Q\alpha$ of the system controlled by BC+AAC and EAAC w.r.t. BC is reported in the column $\Delta Q\alpha$.

Even thought in tests 1, 3 and 6, where LF uncertainty set is used, both BC+AAC and EAAC are not able to meet the specifications on the $Q\alpha$ limitation, a significant improvement (about 28%) w.r.t. the maximum $Q\alpha$ related to BC is apparent. Moreover, the EAAC is able to obtain system stability for all the considered tests, whereas BC+AAC is unstable for large variations of the bending mode frequency (tests 8, 9).

Relevant results are discussed in some detail in what follows.

6.1.1 Test 0 - Nominal condition

In this case, all parameters are set at their nominal values. As expected, the BC has reasonably good performance and the contributions of the AAC and EAAC are minimal. In fact, as shown in Fig. 6.4 the three controllers are all able to keep the aerodynamic load within the safety limit.
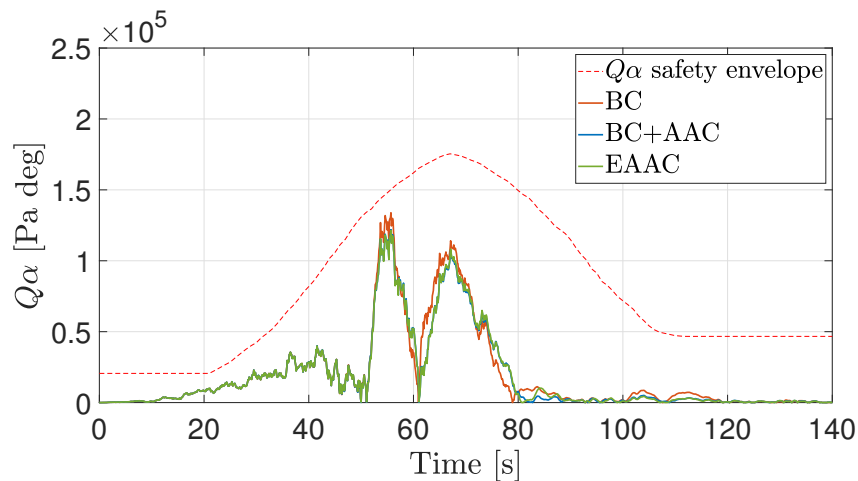
Figure 6.4. Test 0: $Q\alpha$ comparison.

In spite of the fact that AAC and EAAC increase adaptive gain between $t = 50$ and $80\,\mathrm{s}$ so as to manage wind disturbances, as it is observed from the time histories of the total adaptive gain k_T versus time in Fig. 6.5(a), the adaptive controllers provide similar performance than BC. Moreover, the EAAC estimated bending mode frequency ω_{id}, reported in Fig. 6.5(b), correctly follows the time variations of

nominal bending mode frequency $\omega_{nominal}$. In this test no bending mode frequency scattering is taken into account ($\omega_{scattered} = \omega_{nominal}$), as it appears in Fig. 6.5(b).

(a) Adaptive total gain
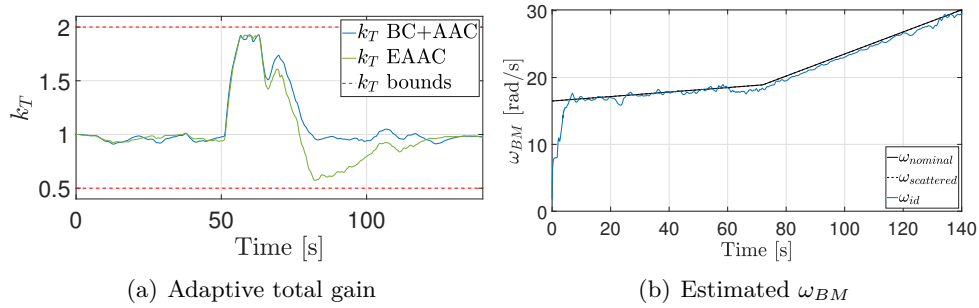
(b) Estimated ω_{BM}

Figure 6.5. Test 0: adaptive parameters. (a) Comparison between BC+AAC and EAAC adaptive total gain. (b) Bending mode frequency ω_{id} estimated by EAAC.
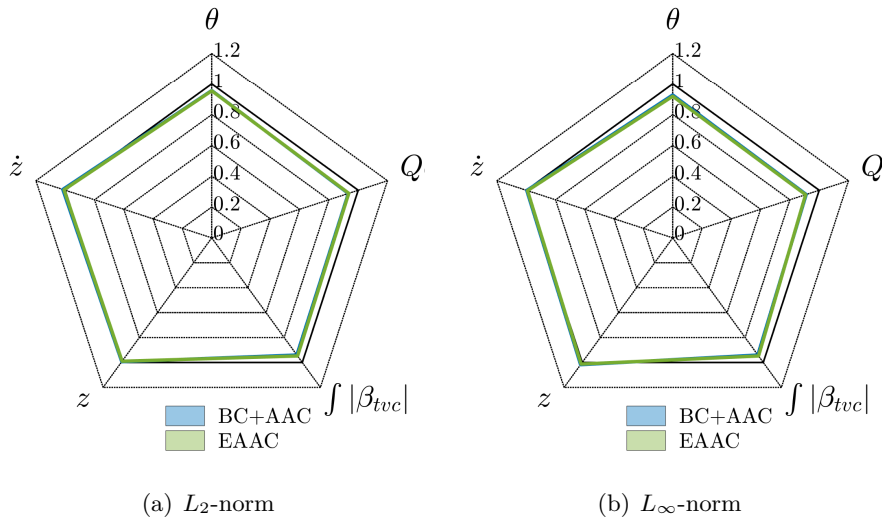
(a) L_2-norm

(b) L_∞-norm

Figure 6.6. Test 0: normalized performances metrics.

The mild action of AAC and EAAC is confirmed in Fig. 6.6, where the L_2-norm and L_∞-norm of attitude error ($\Delta\theta$), z-axis drift (z) and drift rate ($\dot{z}$), and aerodynamic load ($Q\alpha$), are reported together with the overall control effort (that is $\int |\beta_{tvc}|$) of BC+AAC and EAAC, normalized w.r.t. the corresponding values for the BC. The BC+AAC and EAAC configurations achieve only slight reductions of the maximum amplitude of $Q\alpha$ w.r.t. BC as low as 8% and 9%, respectively.

6.1.2 Test 1 - LF scattering set

In this case, only the rigid-body uncertainty set LF is accounted for, whereas the bending mode scattering is zero. For the considered wind disturbance, the BC is

Figure 6.7. Test 1: $Q\alpha$ comparison.

not able to keep $Q\alpha$ within safety envelope (Fig. 6.7).
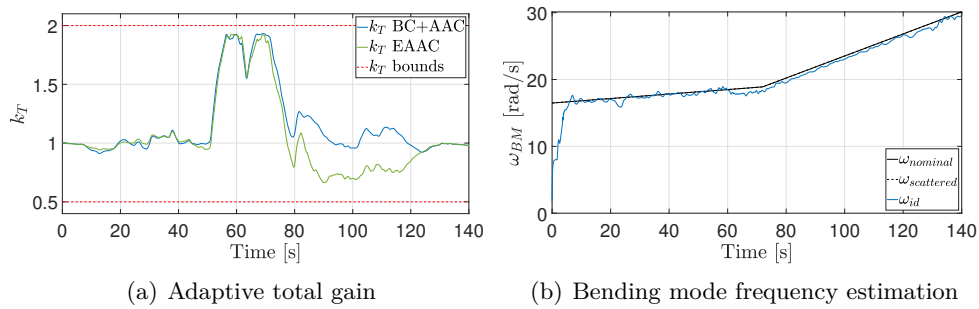
(a) Adaptive total gain

(b) Bending mode frequency estimation

Figure 6.8. Test 1: adaptive parameters. (a) Comparison between BC+AAC and EAAC adaptive total gain. (b) Bending mode frequency estimated by EAAC.
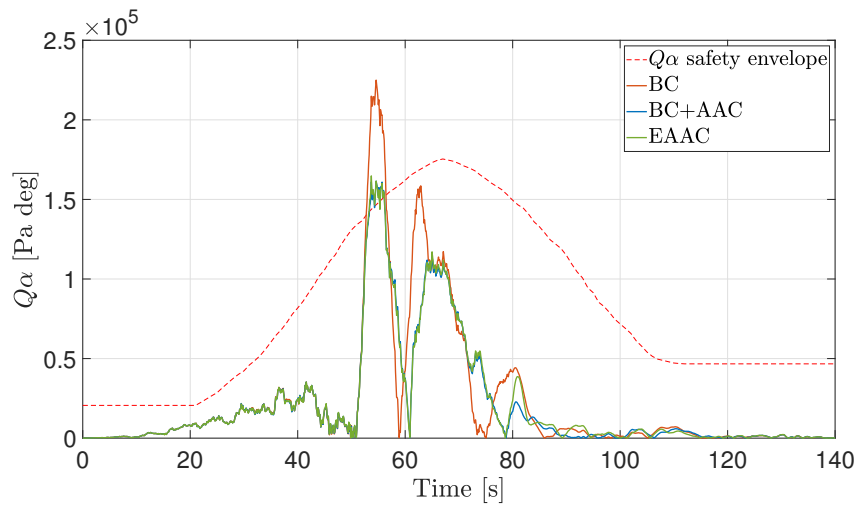
Conversely, as shown in Fig. 6.8(a), where the time histories of the total adaptive gain k_T of BC+AAC and EAAC are reported, the peak at $t = 55\,\text{s}$ is significantly reduced as the adaptive gain k_T is increased between $t = 50$ and $80\,\text{s}$, when the wind disturbance is more intense, so as to satisfy the requirement and prevent LoC. Figure 6.8(b) shows that EAAC correctly tracks the nominal bending mode frequency (in this case $\omega_{scattering} = \omega_{nominal}$) during the flight.

Figure. 6.10, where L_2-norm and L_∞-norm normalized w.r.t. BC performance, of attitude error ($\Delta\theta$), z-axis drift (z) and drift rate ($\dot{z}$), aerodynamic load ($Q\alpha$) and control effort of BC+AAC and EAAC are reported, shows that the BC+AAC and EAAC provide similar and improved overall performances as far as pitch angle (Fig. 6.9), aerodynamic load (Fig. 6.7) and control effort are concerned.
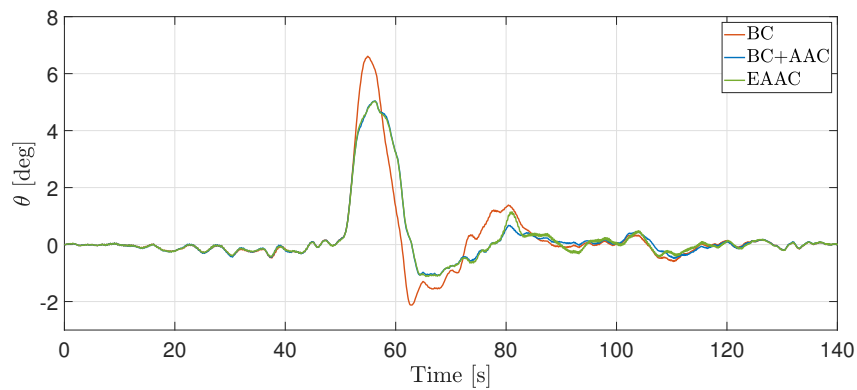
Figure 6.9. Test 1: comparison between BC, BC+AAC and EAAC pitch responses.

(a) L_2-norm

(b) L_∞-norm
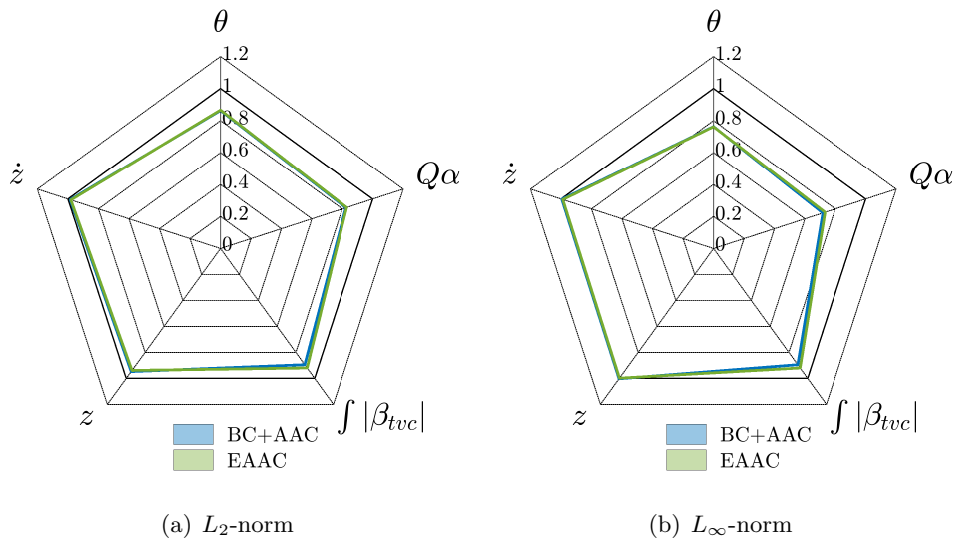
Figure 6.10. Test 1: normalized performance metrics.

6.1.3 Test 7 - Extended BC capability, large rigid-body uncertainty LF$^+$

A large modelling error is simulated by setting the level of uncertainties to LF$^+$, where, as said, the aerodynamic parameter A_6 is increased of 35%, together with a 35% reduction of control authority K_1.

This level of scattering rapidly drives the LV controlled by BC towards divergence, as shown by the pitch angle response in Fig. 6.11. On the other hand, the BC+AAC and EAAC preserve the stability of the system by increasing the adaptive gain k_T (Fig. 6.12(a)) even though the limit on $Q\alpha$ (Fig. 6.13) is violated. The observed LV behavior is in agreement with the results discussed in [38], where simulations are carried out using the nonlinear model of the VEGA LV (Vegacontrol) for
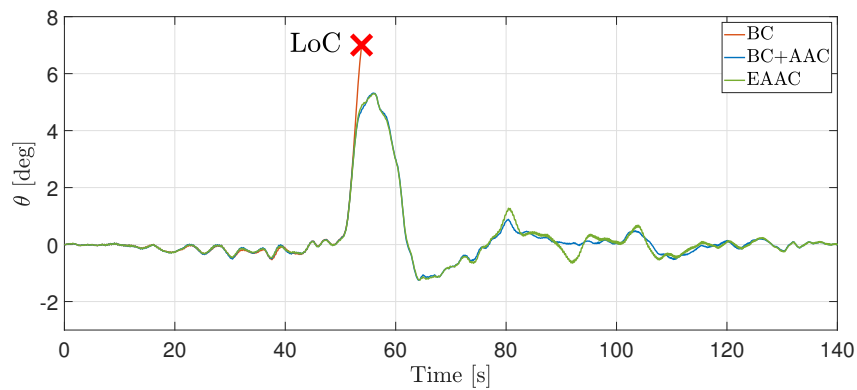
Figure 6.11. Test 7: comparison between BC, BC+AAC and EAAC pitch responses.

large parameter dispersions beyond operation range (35% on a not specified set of parameters) and VV05 wind profile. The results reported in that study show that the system with BC becomes unstable, whereas the AAC can control the instability preventing the LoC. Turning to the present analysis, we see that EAAC correctly identifies the actual ω_{BM}, as shown in Fig. 6.12(b), and the behavior of the BC+AAC and EAAC is quite similar, in terms of adaptive gain k_T modulation (Fig. 6.11) and pitch angle (Fig. 6.11) control. It is worth to remark that even though the systems

(a) Adaptive total gain

(b) Bending mode frequency estimation
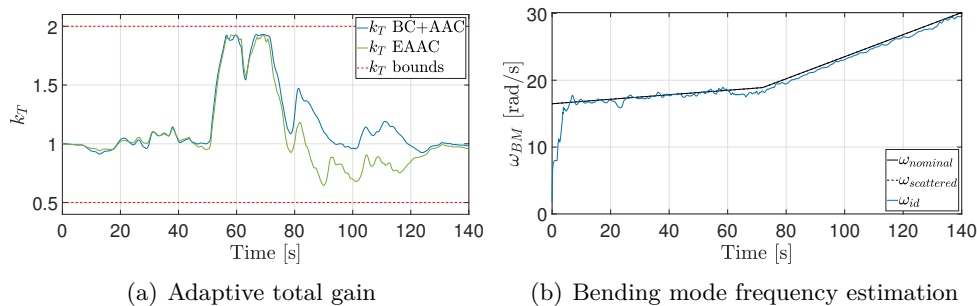
Figure 6.12. Test 7: adaptive parameters. (a) Comparison between BC+AAC and EAAC adatpive total gain. (b) Bending mode frequency estimated by EAAC.

with adaptive controllers do not meet all the requirements, the adaptive algorithms are able to manage large variations of rigid-body parameters together with intense wind disturbances. In this respect, the relevant effect of AAC on control system robustness is apparent (Fig. 6.13).

6.1.4 Test 8 - Large increase of bending mode frequency

In this case, the performances of controllers are investigated when the variation of the bending mode frequency is set to +45%, while the other parameters are perturbed as for the LF scattering set. In this situation, potential instability comes
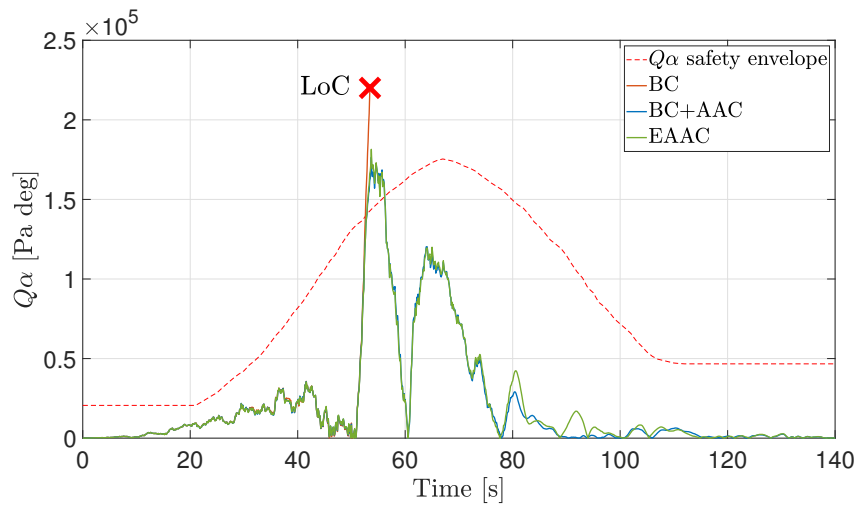
Figure 6.13. Test 7: $Q\alpha$ comparison.

from crossing the left critical point [0 dB, -180 deg], as shown in Fig. 6.3(b). Note that the system with BC only is on the edge of stability.
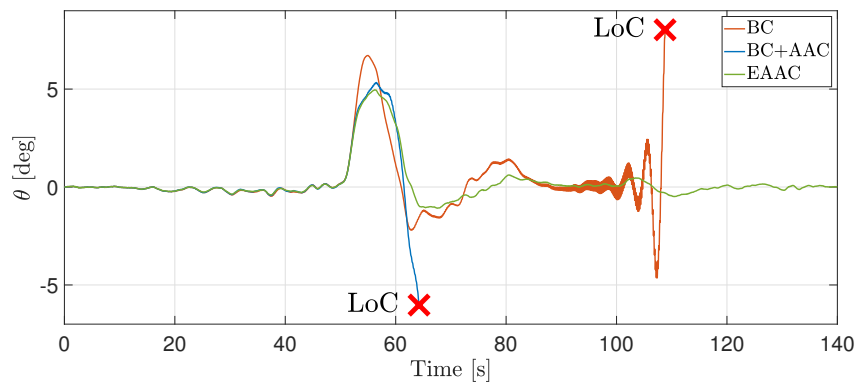
Figure 6.14. Test 8: comparison between BC, BC+AAC and EAAC pitch responses.

Both BC+AAC and BC do not meet requirements, and the divergent behaviors for BC and BC+AAC are apparent in Fig. 6.14, where pitch angle response vs. time is reported. Figure 6.15 shows the Nichols plot at $t = 55\,\text{s}$ and $t = 61\,\text{s}$ for the system controlled by BC in nominal condition and with the considered scattering set, and for the system controlled by BC+AAC in the scattered condition. Regardless of the considered wind profile, an initial increase in the AAC adaptive gain is apparent from the k_T time history shown in Fig. 6.16(a). This result from the action to recover the loss of performance at low frequency, near the Aero GM, due to the variation of the rigid-body parameters A_6 and K_1. The total adaptation gain presents a peak value $k_T = 1.66$ at $t = 55\,\text{s}$, that, if kept constant, would lead to instability, as it is apparent when the Nichols plot in Figure 6.15(a) is observed.

(a) $t = 55\,\text{s}$ (b) $t = 61\,\text{s}$
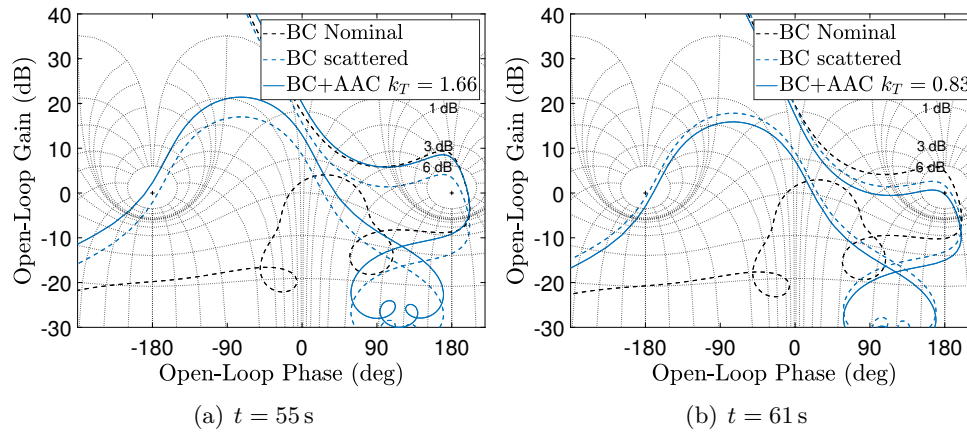
Figure 6.15. Nichols plot of the open loop responses. BC nominal case, BC scattered case and BC scattered case augmented by AAC at $t = 55\,\text{s}$ (a) and $t = 61\,\text{s}$ (b).

(a) Adaptive total gain   (b) Bending mode frequency estimation
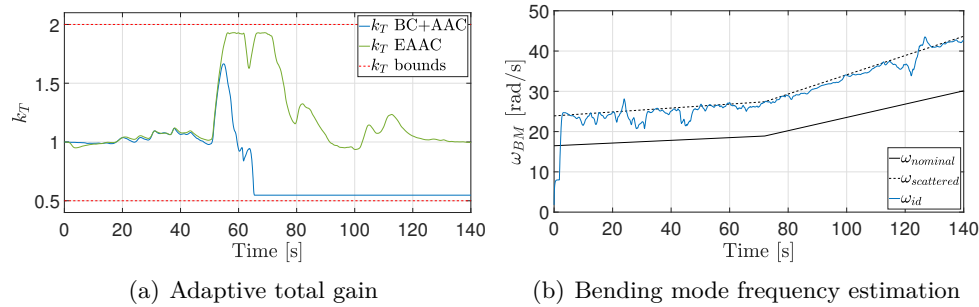
Figure 6.16. Test 8: adaptive parameters. (a) Comparison between BC+AAC and EAAC adaptive total gain. (b) Bending mode frequency estimated by EAAC.

Note that this situation occurs only for a limited amount of time, as shown in Fig. 6.16(a); at t = 61 s the AAC decreases the adaptive gain as a result of the action of the spectral damper, bringing the total adaptive gain to values below unity ($k_T = 0.83$) when trying to stabilize the system at higher frequencies, that is, with respect to the critical point [0 dB, -180 deg]. Unfortunately, as shown in the Nichols plot at $t = 61\,\text{s}$ in Fig. 6.15(b), this leads the system to instability at low frequency, as confirmed by the negative Aero GM at the critical point [0 dB, 180 deg]. The low frequency instability degrades the disturbance rejection capability of the BC+AAC, that is not able to deal with the wind disturbance, so that a LoC event occurs. This circumstance clearly shows the limits of the AAC gain stabilization method.

On the other hand, EAAC correctly identifies the scattered ω_{BM}, as shown in Fig. 6.16(b) and, adapting notch and low-pass filters, avoids the insurgence of an instability at the left critical point [0 dB, 180 deg]. In this respect, the gain adaptation provided by EAAC is now able to limit $Q\alpha$, as apparent in Fig. 6.17,

where the EAAC response in terms of $Q\alpha$ is observed to be slightly above its safety envelope.
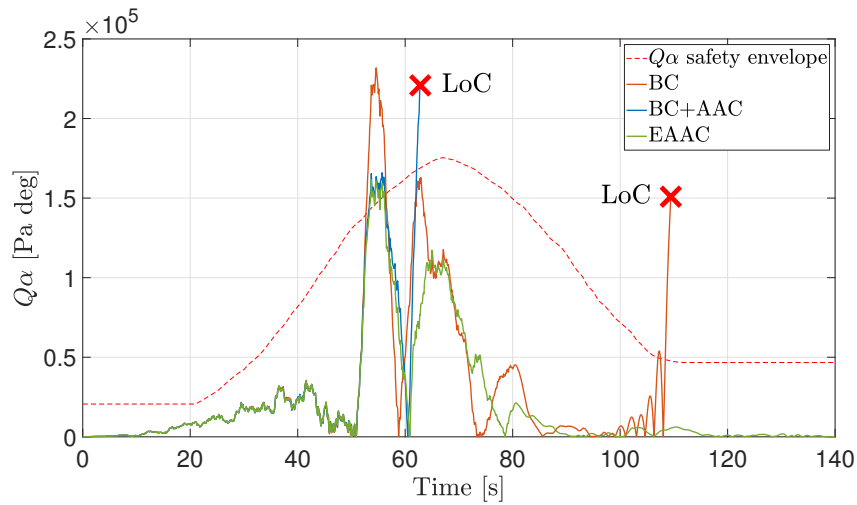
Figure 6.17. Test 8: $Q\alpha$ comparison.

6.1.5 Test 9 - Large decrease of bending mode frequency

In this test, in addition to the LF rigid-body parameter variation, the bending mode frequency is decreased by 45%. While for a ±30% frequency variations no relevant differences from the nominal case are apparent, a 45% frequency reduction is outside the robustness envelope of the BC, and drives the system unstable (Fig. 6.18). In particular, the BC notch and low-pass filters are no longer able to attenuate and phase-stabilize the bending mode, with a consequent reduction of the stability margins.
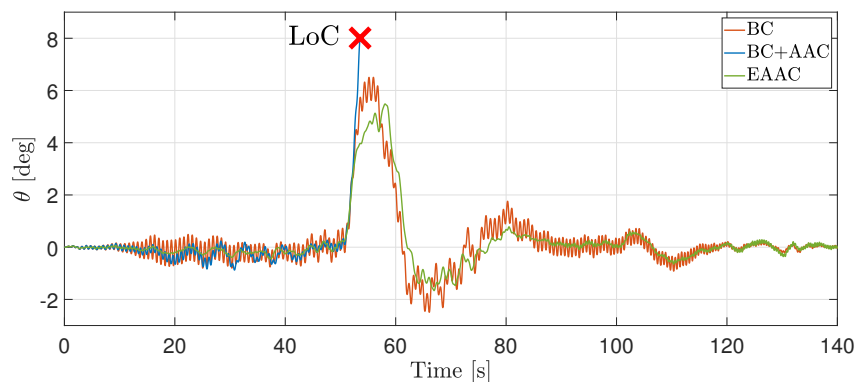
Figure 6.18. Test 9: comparison between BC, BC+AAC and EAAC pitch responses.

Figure 6.18 shows the divergent behavior of BC+AAC at $t = 55\,\mathrm{s}$, whereas the system without control adaptation retains stability, even though high-frequency

oscillations of pitch angle are apparent. The LoC event of the BC+AAC is due to the fact that AAC reduces the adaptive gain k_T (see Fig. 6.19(a)) in an attempt to eliminate high-frequency oscillations; however, by doing so, the controlled system is not longer able to manage the intense wind gust that occurs at $t = 55\,\mathrm{s}$. In the considered off-nominal condition, it is impossible for the AAC to recover stability, regardless of the adopted tuning procedure. In fact, the AAC may only modify the gain magnitude of the BC, that is, it may only shift up or down the open-loop response curves. Therefore, as it is apparent in Fig. 6.20(a) that shows the Nichols plot of the system featuring BC at t = 55, 65 and 75 s, there are not k_T values, that the AAC can generate, able to achieve stabilization.

(a) Adaptive total gain
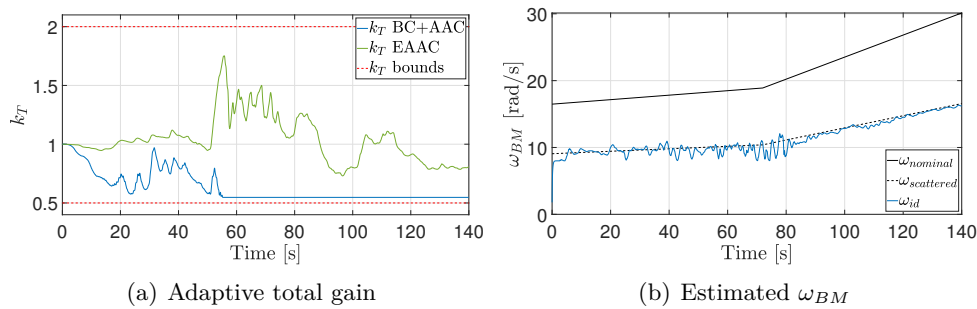
(b) Estimated ω_{BM}

Figure 6.19. Test 9: adaptive parameters. (a) Comparison between BC+AAC and EAAC adaptive total gain. (b) Bending mode frequency estimated by EAAC.

(a) BC

(b) EAAC
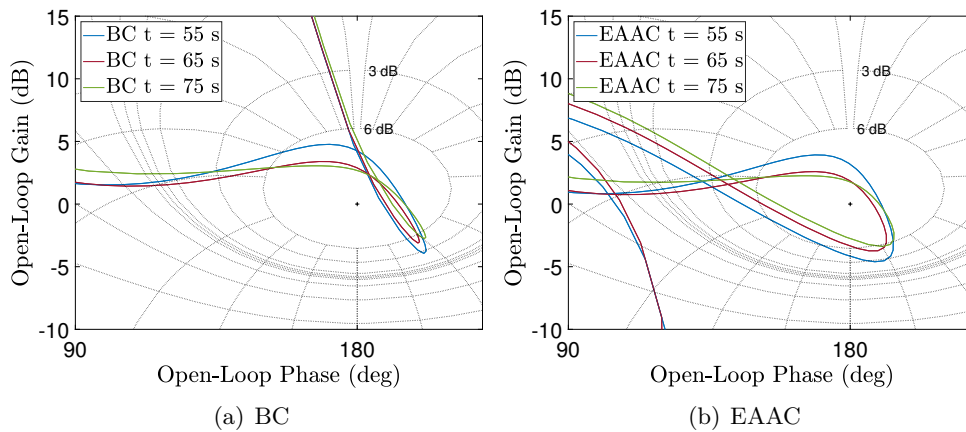
Figure 6.20. Nichols plot at t = 55, 65 and 75 s for LF scattering set and -45% variation of ω_{BM} for the BC and EAAC.

Conversely, the EAAC is effective in maintaining stability, as shown by the pitch response in Fig. 6.18, and achieves better performance w.r.t. BC in terms of aerodynamics load reduction, as apparent in Fig. 6.21. The scattered bending mode frequency (Fig. 6.19(b)) is accurately estimated, and, consequently, the notch and

low-pass filters are correctly tuned, that are able to gain- and phase-stabilize the bending mode. In particular, Fig. 6.20(b), where the Nichols plots of the system controlled by EAAC considering only the adaptation of the bending mode filters, is presented at t = 55, 65 and 75 s, shows that the system is gain- and phase- stabilized due to filter adaptation, the effect of k_T being negligible.
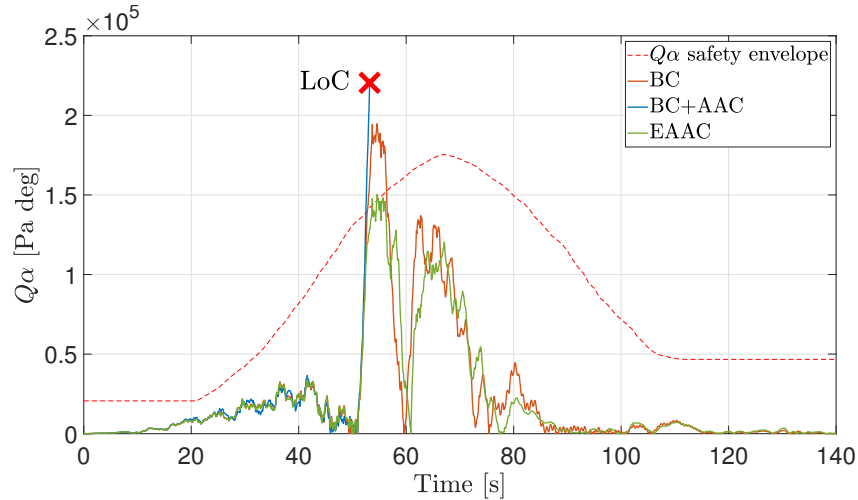
Figure 6.21. Test 9: $Q\alpha$ comparison.

It is also worth to mention that, although the Nichols plot in Fig. 6.3(a) shows that the LV model with BC is unstable, no divergence occurs in the simulations (Fig. 6.18). As already discussed in Sec. 3.3.2, the observed behavior is due to the nonlinear components introduced by saturations on nozzle angle and angular rate.

6.2 Worst-case scenarios

At this point, selected results are presented and discussed with the objective of investigating and comparing the effectiveness of the adaptive control architectures in conditions where large off-nominal parameter variations and/or wind disturbances decrease the open-loop stability of the vehicle and require the AAC to generate a significant control activity. In particular, the effects of ANF implementation on the operating limits of the BC and AAC is investigated. In this respect, beside the results obtained by BC, BC+AAC and EAAC, performance of BC-AN, that is, BC featuring ANF (Eq. (5.11)), is also taken into consideration.

In more detail, two worst-case scenarios are simulated

- **Case 1** bending mode frequency is reduced by 35% and modal gain sensor is increased of 6 dB

- **Case 2** aerodynamic coefficient A_6 is increased by 35%, control moment coefficient K_1 is decreased by -35%, and ω_{BM} is reduced by -45%

6.2.1 Case 1

In the first case the bending mode frequency is reduced so as to increase the coupling between rigid-body and elastic modes. Although the variation of ω_{BM} is outside the robustness envelope of the BC, the AAC succeeds at stabilizing the vehicle [51]. The BC instability is apparent in the Nichols plots of the open-loop frequency response shown in Fig. 6.22 at flight time $t = 72\,\mathrm{s}$, when the dynamic pressure Q is at the maximum value.
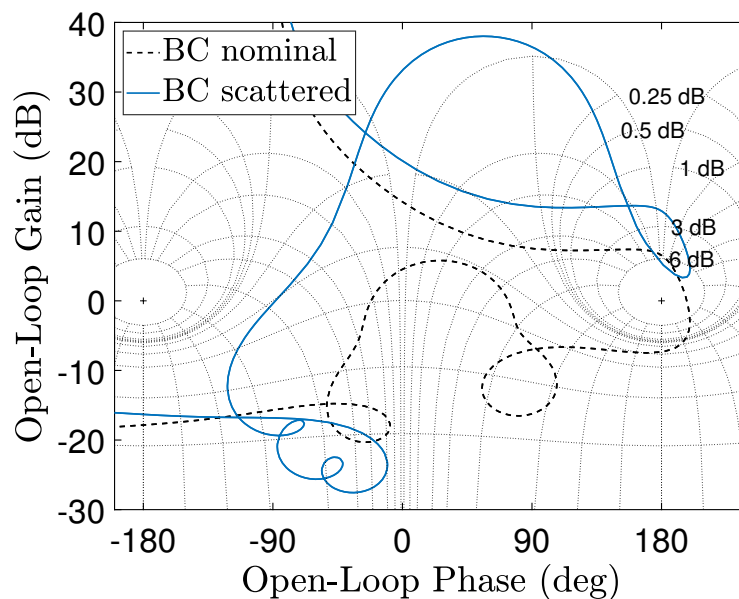
Figure 6.22. Case 1: Nichols plots of open-loop response at $t = 72$ s.

Figure 6.23(a), where the time evolution of $Q\alpha$ is shown for the aforementioned control architectures, confirms that the system controlled by BC is driven unstable, exceeding its aerodynamic load limit. Note that the curve corresponding to BC-AN also shows a loss-of-control (LoC) situation, whereas the two configurations featuring the AAC (BC+AAC and EAAC) retain stability throughout the entire flight by pushing the adaptive gain down to its lower bound (see Fig. 6.23(d)). Gimbal angles generated by these adapted controllers, reported in Fig. 6.23(b), show that the EAAC configuration significantly reduces control activity, as the L_1-norm of β is 38.67 deg s from a value of 52.20 deg s for the BC+AAC configuration. Figure 6.23(c) shows that the perturbed bending mode frequency is properly identified in the EAAC controller. The oscillations of ω_{id}, visible in the figure in the time interval $50 \div 70\,\mathrm{s}$, are due

(a) $Q\alpha$

(b) Gimbal angle

(c) Bending mode frequency estimation

(d) Adaptive gain
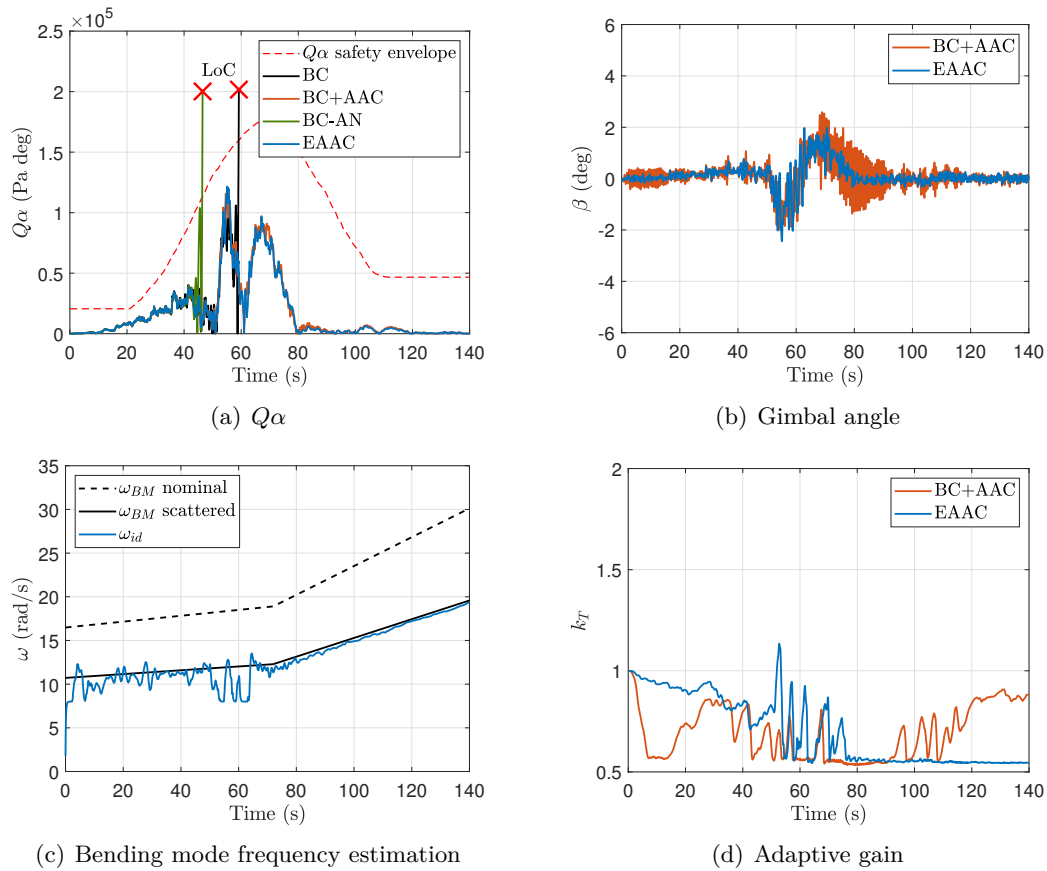
Figure 6.23. Case 1: Simulation results.

to the more intense wind disturbance in that phase of flight, which significantly increases the high frequency excitation of rigid modes so that the input signal to the identification algorithm is more disturbed. Finally, Fig. 6.23(d) shows that the EAAC presents a lower reduction of the adaptive gain k_T in comparison with the BC-AAC scheme, so that there is a larger control authority suitable for managing more challenging off-nominal conditions.

6.2.2   Case 2

In the second test the effect of the ANF implementation on the operating limits of the AAC is investigated. To this end, the aerodynamic coefficient A_6 is increased by 35%, the control moment coefficient K_1 is decreased by -35%, and ω_{BM} is reduced by -45%, while all the other parameters maintain their nominal values.

Figure 6.24, where the open-loop responses of the BC in nominal and scattered conditions are presented, shows that the combined variations of A_6 and K_1 decrease the Aero GM, making it close to zero. Moreover, as the bending mode frequency
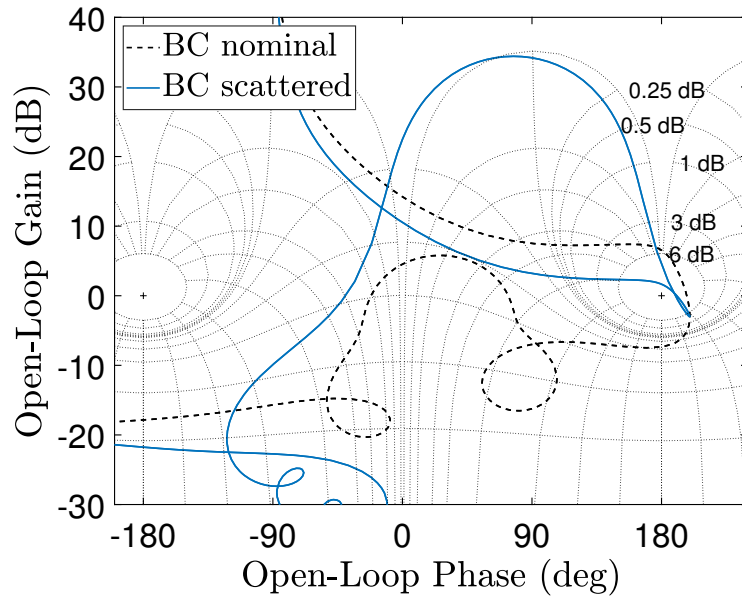
Figure 6.24. Case 2: Nichols plots of open-loop response at $t = 72$ s.

(a) $Q\alpha$

(b) Bending mode frequency estimation
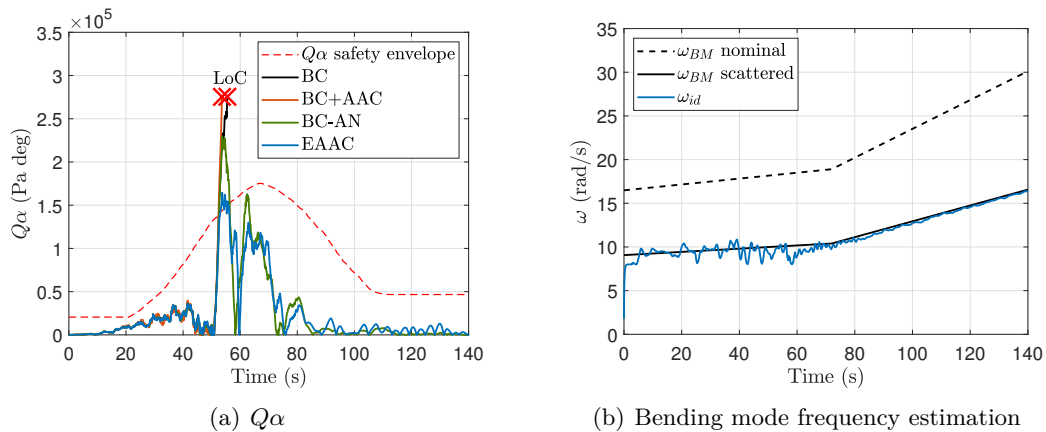
Figure 6.25. Case 2: Simulation results.

decreases, the notch filter of the BC, centered at the nominal bending mode frequency, is no longer effective in attenuating the flexible dynamics. The reductions of Rigid GM and first Flex PM determine a shift of the "hump" on the Nichols plot towards the top-right corner of the figure and, as a consequence, the BC becomes unstable. In this situation, the AAC cannot recover stability because there is no k_T variation that may shift the open-loop response curve corresponding to the scattered model so that it moves clockwise around the critical point $[0\,\mathrm{dB}, 180\,\mathrm{deg}]$. Therefore, in this case, the configuration BC+AAC is unstable at $t = 72$ s, and Fig. 6.25(a) shows that a LoC event (corresponding to divergence of system response) occurs at $t \approx 55$ s.

The same figure also shows that the LoC is avoided by the BC-AN because

the scattered bending mode frequency is correctly estimated (see Fig 6.25(b)), and adaptation of notch and low-pass filters provides phase-stabilization and bending mode attenuation. However, BC-AN is not successful at keeping $Q\alpha$ within the safety envelope. Finally, it is apparent that EAAC is able to both stabilize the system and significantly reduce the maximum values of $Q\alpha$, that even in this extreme scattering condition, are slightly above the limit.

6.3 Monte Carlo campaigns

6.3.1 MC 1

FCS performance assessment is also carried out through extensive Monte Carlo (MC) campaigns where 1000 simulations are run. The first campaign (MC 1) considers the parameter scattering reported in Table 6.4.

Table 6.4. Scattering ranges for MC 1.

Parameter	Scattering range (%)
A_6	$[-35, +35]$
K_1	$[-35, +35]$
a_1	$[-10, +10]$
a_3	$[-10, +10]$
a_4	$[-10, +10]$
ω_{BM}	$[-35, +35]$

Figure 6.26, where the envelopes of $Q\alpha$ together with the corresponding safety limit are reported for the four controller implementations, shows that both BC+AAC and EAAC present more limited maximum values of the aerodynamic load in comparison with BC and BC-AN. This is confirmed in Fig. 6.27, that shows the L_2-norms of attitude error ($\Delta\theta$), the z-axis drift (z) and drift rate ($\dot{z}$), and the aerodynamic load ($Q\alpha$), together with the overall control effort ($\int |\beta_{tvc}|$) for the control configurations BC-AN, BC+AAC and EAAC. The norms are averaged over the number of runs and normalized with respect to the same metrics computed for the LV controlled by the BC. It is apparent that BC+AAC and EAAC improve the performance in terms of reduction of $Q\alpha$, attitude error and control effort.

This is confirmed considering that, as shown in Table 6.6, BC+AAC and EAAC allow for a reduction of about 60%, in comparison with BC and BC-AN, of situations where the $Q\alpha$ safety envelope is violated. In this test, EAAC and BC+AAC performances are very similar, which is somewhat expected as the scattering on ω_{BM} in MC 1 is less critical for the AAC with respect to the situation where the

(a) BC

(b) BC-AN

(c) BC+AAC

(d) EAAC
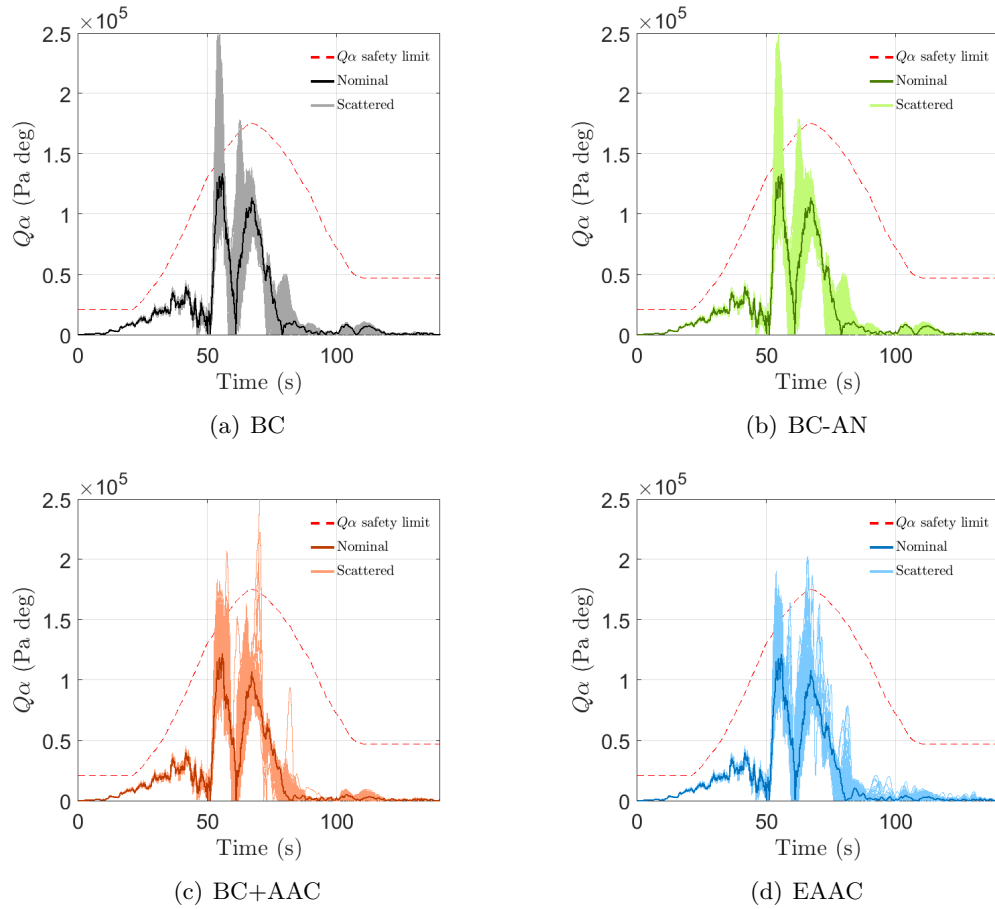
Figure 6.26. MC 1: $Q\alpha$ envelope and safety limit vs. time; bold continuous lines indicate no scattering.

value of ω_{BM} is reduced and brought close to the highest rigid-body frequency. It is also worth to mention that control performance metrics averaged over a large number of cases where model parameters are randomly scattered, are improved over those corresponding to specific, worst-case conditions.

6.3.2 MC 2

A second Monte Carlo simulation campaign (MC 2) is carried out by scattering the model parameters according to Table 6.5, where the bending mode frequency, constant along the flight, is reduced by 35% of its nominal value over the 1.000 simulation runs. Figure 6.28, where the responses in terms of aerodynamic load $Q\alpha$ are reported, shows that BC and BC-AN provide similar results, as already noted for the MC 1 campaign.

Conversely, the BC+AAC presents a substantial performance degradation as
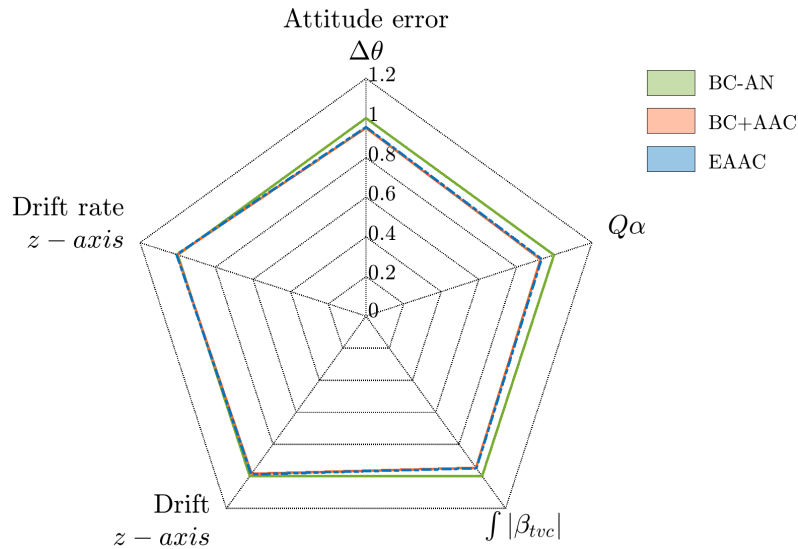
Figure 6.27. MC 1: Normalized performance metrics.

Table 6.5. Scattering ranges for MC 2.

Parameter	Scattering range (%)
A_6	$[-35, +35]$
K_1	$[-35, +35]$
a_1	$[-10, +10]$
a_3	$[-10, +10]$
a_4	$[-10, +10]$
ω_{BM}	-35

Table 6.6. Number of cases exceeding $Q\alpha$ safety limit.

Controller	MC 1	MC 2
BC	329	265
BC-AN	324	258
BC+AAC	119	335
EAAC	144	91

confirmed by the L_2-norms in Figure 6.29, where it is apparent that attitude errors and $Q\alpha$ are greater than the same metrics computed for the BC. On the other hand, EAAC retains the reduction of attitude error, aerodynamic load and control effort that are typically provided by a BC+AAC configuration operating as expected, and to reduce the number of LoC events. This is clearly visible in Table 6.6, as the EAAC is able to prevents 174 of the 265 situations where the constraint on $Q\alpha$ is violated using the BC and, more important, 244 of the 335 mission failures occurring with the BC+AAC control implementation.
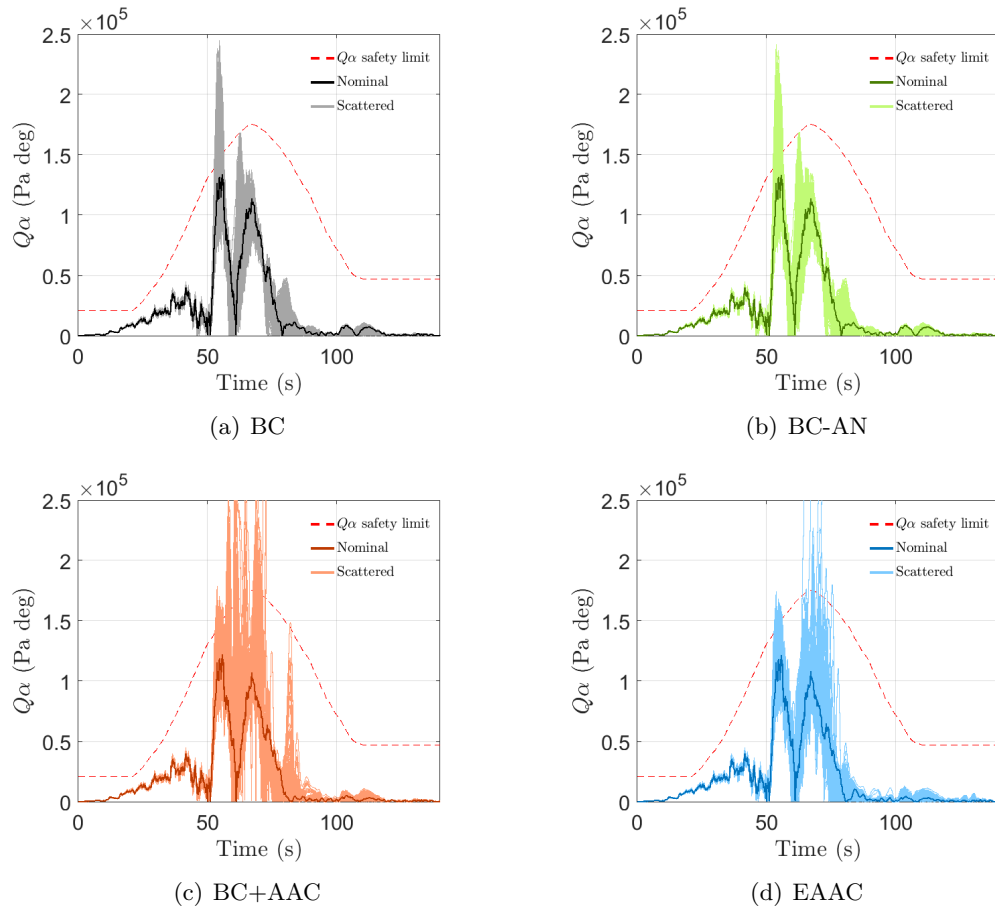
Figure 6.28. MC 2: $Q\alpha$ envelope and safety limit vs. time; bold continuous lines indicate no scattering.
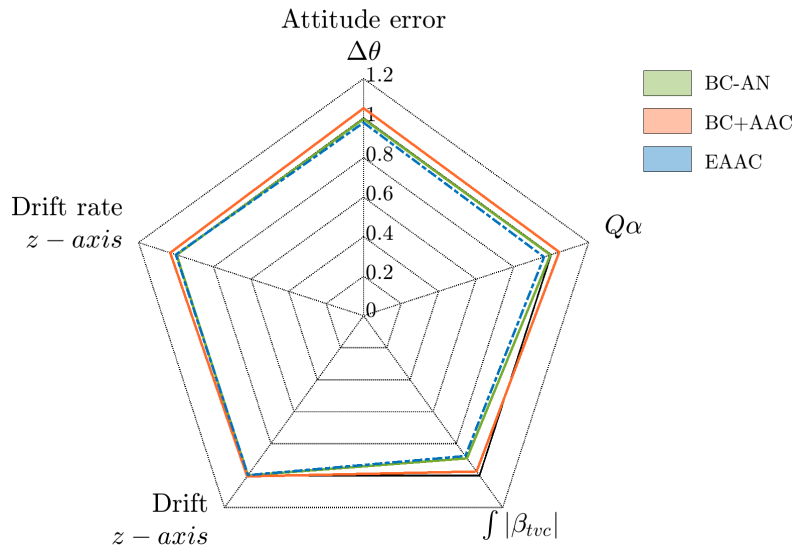
Figure 6.29. MC 2: Normalized performance metrics.

Chapter 7

Conclusions

7.1 Main achievements

The thesis is focused on development and analysis of adaptive control architectures to the Flight Control System (FCS) of a Launch Vehicle (LV) in the atmospheric phase of flight with the following major objectives

1. to improve performance and safety in terms of trajectory error and aerodynamic load minimization

2. to improve the FCS stability robustness against model uncertainties

3. to reduce the burden related to gain tuning and FCS validation activities before each flight.

LV modeling

As a first step, LV modeling is dealt with in order to achieve an accurate description of LV flight from lift-off to first stage separation. A nonlinear model of the LV is developed, the equations of motion of which are derived taking into account all physical aspects relevant for the LV attitude control problem, such as rigid-body dynamics, aerodynamic and propulsion forces and moments, elastic DoFs, and the inertial coupling terms due to nozzle rotation. Suitable wind disturbance models are also devised.

In order to investigate FCS stability and performance in the consolidated framework for linear controller synthesis and analysis (i.e. root locus, Bode diagrams, Nichols charts), a linearized model is derived under the assumptions of small deviations of vehicle motion from the reference trajectory, and assuming that LV

parameters, such as mass or thrust magnitude, are "frozen" over a short period of time. The LV model is completed by the TVC actuator dynamics.

Attitude control design

A classic attitude controller (BC), which consists of a PD controller on pitch axis with anti-drift control, plus a filter to stabilize high-frequency dynamics and bending modes, is developed. The BC is designed to meet traditional stability requirements for LVs, that is, $6\,\mathrm{dB}$ gain and $30\,\mathrm{deg}$ phase margins, and to guarantee robustness against parameter uncertainties. Performance and stability assessments of BC are carried out using frequency-based analyses and time-domain simulations, where a number of LV parameters are scattered and severe wind disturbances are considered. The results show that BC performance degrades as the level of uncertainty increases, as expected. In particular, the maximum amplitude of the aerodynamic load $Q\alpha$ reaches its safety envelope for a 10% increase of A_6 combined with a 10% reduction of K_1, that are the parameters related to the aerodynamic moment and control authority, respectively.

Adaptive control

In the second part of the study, the Augmenting Adaptive Controller (AAC) architecture is taken into consideration. According to this approach the BC output is corrected by a multiplicative gain whose value is adapted during the flight in order to minimize deviations with respect to a suitably specified reference model, and to limit the excitation of high frequency dynamics. As an advantage, AAC implementation does not introduce any modifications in the BC architecture and filter structure.

The main features of the AAC are critically analyzed, and opportunities and limitations of its architecture are investigated. Moreover, a number of simulations confirms that performance and robustness are improved by the adaptive algorithm for the considered variations of model parameters, and in situations where the LV experiences intense wind variations. Furthermore, the AAC is able to prevent loss of control when the level of uncertainties on rigid-body parameters is increased beyond the stability range of BC (up to uncertainty of 35% on A_6 and K_1).

However, it is also observed that relevant variations of bending mode frequency, which cause a loss of effectiveness of BC notch filters, are more troublesome (mostly when the frequency decreases). In those situations, the AAC may degrade BC performance, and even lead the system to instability, as gain stabilization hardly manages large scattering of bending mode frequency.

Optimal tuning of AAC parameters

AAC gain selection is still an open-topic mainly due to the complexity of the spectral damper action, and tuning is based on trial-and-error procedures. In this respect, refined guidelines are discussed in the thesis for the setup of the spectral damper filters, and two novel tuning methodologies for the AAC parameters are presented. The aim is to reduce the issues and burden of the procedures currently adopted for the design of the adaptive laws. In particular, the novel methodologies involve the solution of a robust optimization problem (RDO), the goal of which is to minimize the maximum angular displacement and a suitable measure of the unwanted high frequency oscillations of pitch angle.

The first approach (RDO/MC) uses a genetic algorithm (GA) to find the optimal AAC parameters that minimize an objective function evaluated as the result of a Monte Carlo campaign. This technique is robust with respect to initial estimates of tuning parameters, avoidance of local minima and not smooth merit index.

The second tuning method (RDO/min-max) is formulated as a min-max optimization, where AAC parameters are to be determined that maximize the performance in two worst-case conditions. These conditions are defined by setting the values of uncertain parameters so that the low- and high-frequency gain margins of the open-loop LV controlled by BC are zero. The RDO/min-max is based on the Nelder-Mead simplex method for the solution of the optimization problem, and provides the same quality of results of RDO/MC being much faster and less computationally demanding, as the performance metrics are determined in a few, suitably selected, corner cases. Optimal tuning improves AAC performance in terms of reduced attitude errors and angle-of-attack variations, preventing up to 94% of loss of vehicle (LoV) the considered test cases.

Adaptive bending mode filters and Extended AAC

As said, large variations of bending mode frequency from nominal may significantly degrade the performance of the adaptive algorithm. This can be critical when the bending mode frequency gets closer to the frequencies of rigid-body modes, and the gain variation provided by AAC is not effective when a system where phase-stabilization would be required is dealt with.

In this respect, a novel adaptive control architecture is proposed as a possible means for improving the robustness of AAC to uncertainties in the model of flexible dynamics. Notch and low-pass filters, that are standard components of the BC, are adapted following an on-line estimation of the first bending mode frequency based on the application of the recursive least-squares (RLS) method. The adaptive notch

filters (ANF) are successfully integrated in the control architecture featuring the BC augmented by AAC. The so-called Extended Adaptive Augmenting Control (EAAC) appears effective in improving control system performance in situations where the BC is marginally stable and AAC functionality is challenged by large variations of bending mode frequency.

In particular, it is apparent that in the aforementioned situation, the EAAC provides the required control stability, also reducing the control effort associated to the configuration featuring BC and AAC without filter adaptation. When the gain stabilization realized by AAC would be ineffective to control the vehicle, due to the combined effects of increased aerodynamic action and limited control authority when the bending mode frequency is reduced with respect to its nominal values, the EAAC is again able to stabilize the model and to significantly reduce the structural load.

As a final comment, the adoption of adaptive control methodologies can be an effective and reliable tool for enhancing FCS robustness with respect to parametric uncertainties and, possibly, a mean for limiting the costs of mission integration activities, so as to reduce the recurrent activities in FCS design and validation.

7.2   Future work

Future work and possible improvements for this thesis will require a thorough evaluation of the proposed adaptive control algorithms using a high-fidelity six-degree-of-freedom (6-DoF) nonlinear simulation model that includes all relevant elastic and, if present, sloshing dynamics, tail-wags-dog effects, nonlinear unsteady aerodynamics, sensor dynamics and related error models and external disturbances. The adaptive controller shall be also implemented in the pitch and yaw axes, taking into account roll coupling effects.

In this thesis, the adaptive control techniques have been designed and assessed using a reference LV model of the same class as VEGA LV, the data of which are relative to a single mission. In this regard, future works might investigate the implementation of the proposed adaptive controllers for different LVs and missions. For instance, when reference is made to LVs with liquid-propellant propulsion systems, featuring non-negligible sloshing effects that can create dynamic couplings with rigid and/or flexible body dynamics, the effects sloshing on the effectiveness of the adaptive control architectures developed in this thesis could be investigated.

Furthermore, the 6-DoF nonlinear dynamics model developed in this study is a suitable asset for LV simulation, that can be used in future researches on system

identification and trajectory reconstruction.

Bibliography

[1] J. Hanson, "A plan for advanced guidance and control technology for 2nd generation reusable launch vehicles," in *AIAA guidance, navigation, and control conference and exhibit*, p. 4557, August 2002.

[2] K. Betts, R. Rutherford, J. McDuffie, M. Johnson, M. Jackson, and C. Hall, "Time domain simulation of the nasa crew launch vehicle," in *AIAA Modeling and Simulation Technologies Conference and Exhibit*, p. 6621, 2007.

[3] W. Du, *Dynamic modeling and ascent flight control of Ares-I Crew Launch Vehicle*. PhD thesis, Iowa State University, 2010.

[4] A. Marcos, P. Rosa, C. Roux, M. Bartolini, and S. Bennani, "An overview of the rfcs project v&v framework: optimization-based and linear tools for worst-case search," *CEAS Space Journal*, vol. 7, no. 2, pp. 303–318, 2015.

[5] J. H. Blakelock, *Automatic control of aircraft and missiles*. John Wiley & Sons, 1991.

[6] E. Mooij and X. Wang, "Incremental sliding mode control for aeroelastic launch vehicles with propellant slosh," in *AIAA Scitech 2021 Forum*, p. 1221, 2021.

[7] E. Mooij and D. Gransden, "The impact of aeroelastic effects on the controllability of conventional launch vehicles," in *The 67th International Astronautical Congress, Guadalajara, Mexico*, 2016.

[8] J. Orr, M. Johnson, J. Wetherbee, and J. McDuffie, "State space implementation of linear perturbation dynamics equations for flexible launch vehicles," in *AIAA Guidance, Navigation, and Control Conference*, p. 5962, 2009.

[9] A. L. Greensite, "Analysis and design of space vehicle flight control systems. volume i-short period dynamics," Tech. Rep. NASA-CR-820, GD/C-DDE65-055, 1967.

[10] D. Garner, "Control theory handbook," Tech. Rep. NASA TM-X-53036, NASA Marshall Space Flight Center, 1964.

[11] A. L. Greensite, "Analysis and design of space vehicle flight control systems. volume vii-attitude control during launch," Tech. Rep. NASA-CR-826, GD/C-DDE66-028, 1967.

[12] J. A. Frosch and D. P. Vallely, "Saturn as-501/s-ic flight control system design.," *Journal of Spacecraft and Rockets*, vol. 4, no. 8, pp. 1003–1009, 1967.

[13] W. Haeussermann, "Description and performance of the saturn launch vehicle's navigation, guidance, and control system," *IFAC Proceedings Volumes*, vol. 3, no. 1, pp. 275–312, 1970.

[14] L. EDINGER, "The space shuttle ascent flight control system," in *Guidance and Control Conference*, p. 1942, 1976.

[15] H. Suzuki, "Load relief control of h-iia launch vehicle.," *Proceedings of the 16th IFAC Symposium on Automatic Control in Aerospace, pp.985-990*, June 2004.

[16] J.-W. Jang, A. Alaniz, R. Hall, N. Bedrossian, C. Hall, S. Ryan, and M. Jackson, "Ares i flight control system design," in *AIAA Guidance, Navigation, and Control Conference*, p. 8442, 2010.

[17] H. Charles, L. Chong, J. Mark, W. Mark, and W. Mark, "Ares i flight control system overview," *AIAA Guidance, Navigation and Control Conference*, August, 2008.

[18] W. Leite Filho, "Control system of brazilian launcher," *ESA International conference on space guidance, navigations and control systems*, January, 2000.

[19] S. Byung-Chan, P. Yong-Kyu, R. Woong-Rae, and C. Gwang-Rae, "Attitude controller design and test of korea space launch vehicle-i upper stage," *IJASS International Journal of Aeronautical and Space Science*, 2010.

[20] C. Roux and I. Cruciani, "Scheduling schemes and control law robustness in atmospheric flight of vega launcher," in *7th ESA GNC Conference*, pp. 1–5, 2008.

[21] J. S. Shamma and M. Athans, "Guaranteed properties of gain scheduled control for linear parameter-varying plants," *Automatica*, vol. 27, no. 3, pp. 559–564, 1991.

[22] J. S. Shamma, *Analysis and design of gain scheduled control systems.* PhD thesis, Massachusetts Institute of Technology, 1988.

[23] A. Marcos, C. Roux, M. Rotunno, H.-D. Joos, S. Bennani, L. F. Peñín, and A. Caramagno, "The v&v problematic for launchers: current practice and potential advantages on the application of modern analysis techniques," in *ESA Guidance, Navigation and Control Conference, Karlovy Vary. Czech Republic*, 2011.

[24] C. Roux, V. Mantini, A. Marcos, L. Peñín, and S. Bennani, "Robust flight control system design verification & validation for launchers," in *AIAA Guidance, Navigation, and Control Conference*, p. 4996, 2012.

[25] A. Brito, W. Leite Filho, and F. Ramos, "Approach comparison for controller design of a launcher," *Proceedings of 6th ESA International Conference on Spacecraft Guidance, Navigation and Control Systems*, October, 2005.

[26] H. Klotz, "Ariane 5 dynamics and control," in *Automatic Control in Aerospace 1992*, pp. 227–233, Elsevier, 1993.

[27] H. Kwakernaak and R. Sivan, *Linear optimal control systems*, vol. 1. Wiley-interscience New York, 1972.

[28] J. Doyle, "Guaranteed margins for lqg regulators," *IEEE transactions on automatic control, pp. 756-757*, 1978.

[29] J. C. Doyle, K. Glover, P. P. Khargonekar, and B. A. Francis, "State-space solutions to standard h_2 and h_∞ control problems," *IEEE Transactions on Automatic Control*, vol. 34, no. 8, pp. 831–847, 1989.

[30] A. P. White, G. Zhu, and J. Choi, *Linear Parameter-Varying Control for Engineering Applications.* Springer-Verlag GmbH, 2013.

[31] D. F. Enns, "Rocket stabilization as a structured singular value synthesis design example," *IEEE Control Systems Magazine*, vol. 11, no. 4, pp. 67–73, 1991.

[32] J. Doyle, K. Glover, P. Khargonekar, and B. Francis, "State-space solutions to standard h_2 and h_∞ control problems," in *1988 American Control Conference*, pp. 1691–1696, IEEE, 1988.

[33] M. Ganet and M. Ducamp, "LPV CONTROL FOR FLEXIBLE LAUNCHER," in *AIAA Guidance, Navigation, and Control Conference*, American Institute of Aeronautics and Astronautics, aug 2010.

[34] E. Gadea Díaz, "Design of a robust controller for the vega tvc using the μ-synthesis technique," Master's thesis, Universitat Politècnica de Catalunya, 2010.

[35] P. Gahinet and P. Apkarian, "Structured h∞ synthesis in MATLAB," *IFAC Proceedings Volumes*, vol. 44, pp. 1435–1440, jan 2011.

[36] D. Navarro-Tapia, A. Marcos, P. Simplício, S. Bennani, and C. Roux, "Legacy recovery and robust augmentation structured design for the vega launcher," *International Journal of Robust and Nonlinear Control*, 2019.

[37] M. Ganet-Schoeller and J. Desmariaux, "Structured h∞ synthesis for flexible launcher control," *IFAC-PapersOnLine*, vol. 49, no. 17, pp. 450–455, 2016.

[38] D. Navarro-Tapia, A. Marcos, S. Bennani, and C. Roux, "Robust-control-based design and comparison of an adaptive controller for the VEGA launcher," in *AIAA Scitech 2019 Forum*, American Institute of Aeronautics and Astronautics, Jan 2019.

[39] K. J. Åström and B. Wittenmark, *Adaptive control.* Courier Corporation, 2013.

[40] N. T. Nguyen, "Model-reference adaptive control," in *Model-Reference Adaptive Control*, pp. 83–123, Springer, 2018.

[41] S. G. Anavatti, F. Santoso, and M. A. Garratt, "Progress in adaptive control systems: past, present, and future," in *2015 International Conference on Advanced Mechatronics, Intelligent Manufacture, and Industrial Automation (ICAMIMIA)*, pp. 1–8, IEEE, 2015.

[42] A. P. Nair, N. Selvaganesan, and V. Lalithambika, "Lyapunov based pd/pid in model reference adaptive control for satellite launch vehicle systems," *Aerospace Science and Technology*, vol. 51, pp. 70–77, 2016.

[43] C. Plaisted and A. Leonessa, "Expendable launch vehicle adaptive autopilot design," in *AIAA Guidance, Navigation and Control Conference and Exhibit*, p. 7126, 2008.

[44] M. Wang, J. Yang, G. Qin, and Y. Yan, "Adaptive fault-tolerant control with control allocation for flight systems with severe actuator failures and input saturation," in *2013 American Control Conference*, pp. 5134–5139, IEEE, 2013.

[45] U. Ansari, S. Alam, *et al.*, "Trajectory optimization and adaptive fuzzy based launch vehicle attitude control," in *2012 20th Mediterranean Conference on Control & Automation (MED)*, pp. 457–462, IEEE, 2012.

[46] J. Muse, K. Kim, L. Qin, A. Calise, and J. Craig, "Adaptive attitude and vibration control of the nasa ares crew launch vehicle," in *AIAA Guidance, Navigation and Control Conference and Exhibit*, p. 7129, 2008.

[47] A. Khoshnood, J. Roshanian, A. Jafari, and A. Khaki-Sedigh, "An adjustable model reference adaptive control for a flexible launch vehicle," *Journal of dynamic systems, measurement, and control*, vol. 132, no. 4, 2010.

[48] C.-S. Oh, H. Bang, and C.-S. Park, "Attitude control of a flexible launch vehicle using an adaptive notch filter: ground experiment," *Control engineering practice*, vol. 16, no. 1, pp. 30–42, 2008.

[49] M. ENGLEHART and J. Krause, "An adaptive control concept for flexible launch vehicles," in *Astrodynamics Conference*, p. 4622, 1992.

[50] E. Kharisov, I. Gregory, C. Cao, and N. Hovakimyan, "L1 adaptive control for flexible space launch vehicle and proposed plan for flight validation," in *AIAA Guidance, Navigation and Control Conference and Exhibit*, p. 7128, 2008.

[51] J. Orr and T. Van Zwieten, "Robust, practical adaptive control for launch vehicles," in *AIAA Guidance, Navigation, and Control Conference*, p. 4549, 2012.

[52] J. Orr, J. Wall, T. VanZwieten, and C. Hall, "Space launch system ascent flight control design," *Advances in the Astronautical Sciences*, vol. 151, pp. 141–154, 01 2014.

[53] S. Creech, T. May, and K. Robinson, "Nasa's space launch system: An enabling capability for international exploration," in *IAA Space Exploration Conference*, M14-3167, (Washington, D. C., United States), 2014.

[54] J. H. Wall, J. S. Orr, and T. S. VanZwieten, "Space launch system implementation of adaptive augmenting control," in *37th Annual American Astronautical Society (AAS) Guidance, Navigation, and Control Conference,* NASA AAS 14-051, (Breckenridge, CO, United States), 2014.

[55] K. Clements and J. Wall, "Time domain stability margin assessment of the nasa space launch system gn&c design for exploration mission one," in *AS Guidance and Control Conference*, (Breckenridge, CO), 11-15 Aug. 2017.

[56] T. S. VanZwieten, M. R. Hannan, and J. H. Wall, "Evaluating the stability of nasa's space launch system with adaptive augmenting control," *CEAS Space Journal*, vol. 10, no. 4, pp. 583–595, 2018.

[57] T. VanZwieten, E. Gilligan, J. Wall, J. Orr, C. Miller, and C. Hanson, "Adaptive augmenting control flight characterization experiment on an f/a-18," in *Advances in the Astronautical Sciences Guidance, Navigation and Control* (Univelt, ed.), vol. 151, pp. 241–257, Jan. 2014.

[58] J.-W. Jang, R. Hall, N. Bedrossian, and C. Hall, "Ares-i bending filter design using a constrained optimization approach," in *AIAA Guidance, Navigation and Control Conference and Exhibit*, p. 6289, 2008.

[59] S.-I. Leea, J. Ahn, and W.-R. Roh, "Integrated design optimization of structural bending filter and gain schedules for rocket attitude control system," *arXiv preprint arXiv:1802.01875*, 2018.

[60] C. Cunningham and W. Higgins Jr, "Study of applications of a tracking filter to stabilize large flexible launch vehicles," tech. rep., Phase I, Final Technical Report Procurement Request, 1966.

[61] R. Gaylor, R. L. Schaperkoetter, and D. C. Cunningham, "An adaptive tracking filter for bending-mode stabilization.," *Journal of Spacecraft and Rockets*, vol. 4, no. 5, pp. 573–577, 1967.

[62] A. L. Greensite, "Analysis and design of space vehicle flight control systems. volume xiii-adaptive control," 1967.

[63] W. Ra, "Practical adaptive notch filter for missile bending mode rejection," *Electronics Letters*, vol. 41, no. 5, pp. 228–229, 2005.

[64] A. A. jafari, A. M. Khoshnood, and J. Roshanian, "Model reference adaptive method for estimating the bending vibration frequency of a flexible system," in *International MultiConference of Engineers and Computer Scientists 2008, IMECS 2008*, vol. 2, 2008.

[65] H. Whitaker, "An adaptive system for control of the dynamics performances of aircraft and spacecraft," *Inst. Aeronatical Sciences*, pp. 59–100, 1959.

[66] P. Osburn, *New developments in the design of model reference adaptive control systems*. Institute of the Aerospace Sciences, 1961.

[67] H.-D. Choi and H. Bang, "An adaptive control approach to the attitude control of a flexible rocket," *Control engineering practice*, vol. 8, no. 9, pp. 1003–1010, 2000.

[68] S. S. Haykin, *Adaptive filter theory*. Pearson Education India, 2005.

[69] H.-G. Beyer and B. Sendhoff, "Robust optimization – a comprehensive survey," *Computer Methods in Applied Mechanics and Engineering*, vol. 196, pp. 3190–3218, jul 2007.

[70] W. Zhai, P. Kelly, and W.-B. Gong, "Genetic algorithms with noisy fitness," *Mathematical and Computer Modelling*, vol. 23, pp. 131–142, jun 1996.

[71] J. C. Lagarias, J. A. Reeds, M. H. Wright, and P. E. Wright, "Convergence properties of the nelder–mead simplex method in low dimensions," *SIAM Journal on Optimization*, vol. 9, no. 1, pp. 112–147, 1998.

[72] B. Etkin, *Dynamics of atmospheric flight.* Courier Corporation, 2012.

[73] J. Orr, "A flight dynamics model for a multi-actuated flexible rocket vehicle," in *AIAA Atmospheric Flight Mechanics Conference*, p. 6563, 2011.

[74] B. Etkin and L. D. Reid, *Dynamics of flight*, vol. 2. Wiley New York, 1959.

[75] M. Rheinfurth and H. Wilson, *Methods of applied dynamics*, vol. 1262. National Aeronautics and Space Administration, Office of Management . . . , 1991.

[76] P. Simplício, S. Bennani, A. Marcos, C. Roux, and X. Lefort, "Structured singular-value analysis of the vega launcher in atmospheric flight," *Journal of Guidance, Control, and Dynamics*, pp. 1342–1355, 2016.

[77] D. Navarro Tapia, A. Marcos, S. Bennani, and C. Roux, "Joint robust structured design of vega launcher's rigid-body controller and bending filter," 10 2018.

[78] D. R. Lukens, A. F. Schmitt, and G. T. Broucek, "Approximate transfer functions for flexible-booster-and autopilot analysis," tech. rep., GENERAL DYNAMICS CORP POMONA CA POMONADIV, 1961.

[79] D. Johnson, "Terrestrial environment (climatic) criteria guidelines for use in aerospace vehicle development. 2008 revision," NASA/TM 2008-215633, 2008.

[80] B. Wie and K.-W. Byun, "New generalized structural filtering concept for active vibration control synthesis," *Journal of Guidance, Control, and Dynamics*, vol. 12, no. 2, pp. 147–154, 1989.

[81] R. F. Hoelker, "Theory of artificial stabilization of missiles and space vehicles with exposition of four control principles," *NASA Technical Note, NASA TN D-555*, June, 1961.

[82] D.-W. Gu, P. Petkov, and M. M. Konstantinov, *Robust control design with MATLAB®.* Springer Science & Business Media, 2005.

[83] S. Pankaj, J. S. Kumar, and R. Nema, "Comparative analysis of mit rule and lyapunov rule in model reference adaptive control scheme," *Innovative Systems Design and Engineering*, vol. 2, no. 4, pp. 154–162, 2011.

[84] D. Navarro-Tapia, A. Marcos, S. Bennani, and C. Roux, "Robust-control-based design and comparison of an adaptive controller for the vega launcher," AIAA SciTech Forum, American Institute of Aeronautics and Astronautics, Jan. 2019.

[85] D. Trotta, A. Zavoli, G. De Matteis, and A. Neri, "Opportunities and limitations of adaptive augmented control for launch vehicle attitude control in atmospheric flight," in *Astrodynamics Specialist Conference,* AAS 19-765, (Portland, Maine), 11-15 Aug. 2019.

[86] T. H. Cormen, C. E. Leiserson, R. L. Rivest, and C. Stein, *Introduction to algorithms.* MIT press, 2009.

[87] M. Mitchell, *An Introduction to Genetic Algorithms (Complex Adaptive Systems).* MIT Press, 1998.

[88] H. Choi and J. Kim, "Adaptive notch filter design for bending vibration of a sounding rocket," *Proceedings of the Institution of Mechanical Engineers, Part G: Journal of Aerospace Engineering*, vol. 215, no. 1, pp. 13–23, 2001.

[89] C.-S. Oh and H. Bang, "Attitude control of flexible launch vehicle using adaptive notch filter," *IFAC Proceedings Volumes*, vol. 38, no. 1, pp. 187–192, 2005.